Strål
säkerhets
myndigheten
Swedish Radiation Safety Authority

Author: Mikael Möller
Andreas Gustafsson
Peter Segle

Research

2015:43

Robust structural verification of pressurized nuclear components subjected to ratcheting

Report number: 2015:43 **ISSN:** 2000-0456
Available at www.stralsakerhetsmyndigheten.se

SSM perspective

Background

Pressurized components in nuclear applications that are subjected to cyclic loading may exhibit progressive deformation, so called structural ratcheting. If the component is made out of a material that are deformation hardening, it may also exhibit material ratcheting.

The combined effects of structural- and material ratcheting are not taken into account in the methods and material models currently used for structural verification of pressurized nuclear components.

Objective

The project aims to develop guidelines on how to evaluate pressurized nuclear components subjected to ratcheting in a rational and conservative way that are code compliant with ASME III.

The experimental studies are performed with two different laboratory test set ups, one called “two-rod test” and the other a tube test. Numerical studies with five different constitutive models are investigated in the project. The constants in the constitutive models are based on material characterization via tensile testing and fully-reversed strain controlled cycling. The three materials investigated are the ferritic steels P235 and P265 as well as the austenitic steel 316L.

Results

- Simulation of cyclic plastic deformation should be done with an as simple constitutive model as possible, still capturing the essential response. Important reasons are that simple models are easier to understand and work with and that fewer tests are needed for characterisation of the material.

- The simplest model that can be used for simulation of cyclic plastic deformation is the ideal plastic model. In most cases this model overestimates strain development and grossly overestimates ratcheting. Thus, the ideal plastic model may be used for establishment of an upper bound. The use of this model may be the first step in an analysis of the plastic response of a structure. Minimum yield stress according to material data sheets should then be used. Results from such an analysis might be sufficient for structural verification of the component.

- For pressure equipment subjected to cyclic plastic deformation, structural ratcheting often dominates over material ratcheting. The reason for this is that the direction for which reversed plastic cycling takes place normally does not coincide with the direction of incremental plastic deformation (ratcheting). This fact facilitates the use of linear models in the analysis of pressure equipment subjected to cyclic plastic deformation.

- Among the constitutive models investigated, the Besseling multi-linear model is recommended for simulation of pressure equipment subjected to cyclic plastic deformation.

- An important feature for materials exhibiting a yield plateau – which most carbon steels do – is that the applicable stress-strain curve for cyclic analysis with kinematic models is that of a material with a stress-strain curve obtained by back extrapolation of the strain hardening portion of the monotonic curve such that a stress-strain curve similar to austenitic steels is obtained. The stress-strain curve applicable for cyclic loading is half the reversed curve following the yield plateau in tension.

Need for further research

Code information on material strength is yield and tensile strength. The construction of stress-strain curves from this information is not obvious. The Eurocode 3 (EN-1993-1-4) and RCC-MRx design code both give analytical expressions for stress-strain curves as a function of yield and tensile strength and this may constitute an applicable procedure for austenitic steels. For carbon steels however, there is no obvious route to determine applicable stress-strain curves for cyclic analysis. The experimental procedure for determining such curves are however simple as outlined in this project. It is recommended that such experimental stress-strain curves are derived for common pressure vessel steels as an extension to this project.

Project information

Contact person SSM: Daniel Kjellin
Reference: SSM2012-4908

Strål
säkerhets
myndigheten
Swedish Radiation Safety Authority

Author: Mikael Möller [1)], Andreas Gustafsson [1)], Peter Segle [2)]

[1)] Uddcomb AB, Helsingborg, [2)] Inspecta Nuclear AB, Stockholm

2015:43

Robust structural verification of pressurized nuclear components subjected to ratcheting

Date: October 2015
Report number: 2015:43 **ISSN:** 2000-0456
Available at www.stralsakerhetsmyndigheten.se

This report concerns a study which has been conducted for the Swedish Radiation Safety Authority, SSM. The conclusions and viewpoints presented in the report are those of the author/authors and do not necessarily coincide with those of the SSM.

Summary

Two-rod tests and tube tests form the basis for this investigation. Specimens are made of the ferritic steels P235 and P265 as well as the austenitic steel 316L. Determination of the constants in the five constitutive models used in the project is based on material characterisation of the three materials. This characterisation involves tensile testing and fully-reversed strain controlled cycling. The possibility to simulate the response of conducted experiments with the different material models is investigated thoroughly. Recommendations for how ratcheting in structures subjected to cyclic plastic deformation can be predicted by numerical simulation are developed. Among the constitutive models investigated, the Besseling multi-linear model is recommended for simulation of pressure equipment subjected to ratcheting.

Sammanfattning

Cyklisk plastisk deformation studeras utgående från tvåstångsprovning och axiellt deformationsstyrd cykling av trycksatta rör. De ferritiska stålen P235 och P265 tillsammans med det austenitiska stålet 316L ingår i studien. Bestämning av konstanter i fem konstitutiva modeller baseras på karakterisering av materialen genom dragprov och fullt reverserad töjningsstyrning provning. Möjligheten att prediktera genomförda experiment med de fem modellera undersöks noggrant. Rekommendationer ges för hur ratcheting i strukturer utsatta för cyklisk plastisk deformation kan predikteras. Besselings multi-linjära modell rekommenderas för simulering av tryckbärande utrustning utsatt för ratcheting.

Content

Nomenclature

C_k	constant in nonlinear kinematic hardening model [Pa]
E	Young’s modulus [Pa]
H_p	plastic modulus [Pa]
s_{ij}	stress deviator tensor [Pa]
S_m	ASME design stress intensity value [Pa]
S_y	yield stress [Pa]
α_{ij}	back-stress tensor [Pa]
ε^p	uniaxial plastic strain [-]
ε_p	effective plastic strain [-]
ε_{ij}	strain tensor [-]
ε_{ij}^e	elastic strain tensor [-]
ε_{ij}^p	plastic strain tensor [-]
γ_k	constant in nonlinear kinematic hardening model [-]
$d\lambda$	scalar multiplier [-]
σ	uniaxial stress [Pa]
σ_{bound}	bounding stress in nonlinear models [Pa]
σ_e	effective stress [Pa]
σ_{ij}	stress tensor [Pa]
σ_{prim}	primary stress [Pa]
$\Delta\sigma_{sec}$	secondary stress range [Pa]

1. Introduction

Three failure modes are addressed in the assessment of pressure retaining components in nuclear power plants. These are i) collapse, ii) progressive deformation (ratcheting), and iii) low cycle fatigue. All these failure modes involve plastic deformations. For obvious reasons however, all three failure modes have historically been addressed by means of linear elastic analysis and subsequent stress evaluation. The objectives of these evaluation procedures are to approximately predict elastoplasticity from elastic analysis. Depending on the failure mode and type of component considered, the procedures may be both complicated and un-precise. Elastoplastic analysis results in superior accuracy and – in general – higher predicted resistance and life span.

The elastoplastic assessment of collapse is conducted by means of limit analysis and such analysis requires little from the applied constitutive model since it involves monotonic loading only. The following hence relates to cyclic loading in general and to progressive deformation in particular.

Ratcheting addressed in the assessment of nuclear components may be illustrated by e.g. the Bree problem. For a thorough discussion of the mechanics of this phenomenon, [1] may be consulted. There are other ratcheting mechanisms, e.g. ratcheting from secondary bending of a pressurized pipe, for which the ratcheting has a different origin. In any case, these ratchetings may be denoted structural ratcheting since they are the result of stresses and strains within the structure.

Progressive deformation may occur in structures regardless of the hardening properties of the material. Strain hardening is beneficial in this respect and is, hence, desirable to account for. However, strain hardening metals exhibit certain characteristics in cyclic loading – they have an inherent tendency to ratchet on their own. This is a material property and it has nothing to do with the equilibrium driven ratcheting described above. This material property is characterised by the presence of ratcheting in asymmetric stress cycling, i.e. uni-axial cycling at a mean stress.

Obviously, the question arises whether this material ratcheting and the structural ratcheting above interact. If such an interaction exists, all elastoplastic assessments of progressive deformation need to be conducted with constitutive models that are capable of simulating material ratcheting. Most of the cyclic elastoplastic assessments up to now have been conducted with multi-linear kinematic hardening constitutive models of Besseling [2] or Mroz, [3] type. Such models cannot reproduce material ratcheting, as they generate a closed loop at asymmetric stress cycling regardless of mean stress.

There are models, however, that predict material ratcheting from such a loading. The most well-known is likely the Chaboche model [4], which is a superposition of several Armstrong-Frederick kinematic models [5] with or without elements of isotropic hardening. There are more refined models as well, but all seem to share the same basic structure.

Predictions from elastoplastic simulation of ratcheting in general differ depending on what constitutive model is applied. In some problems, the deviations may be large. Obviously then, some constitutive models perform poorly in the prediction of ratcheting. This is unsatisfactory since the objective of using elastoplastic ratcheting analysis is to obtain a high accuracy in general and higher than for elastic analysis in particular.

2. Purpose with project

The objective of this project is to – via an extensive experimental program – investigate the performance of different constitutive models in ratchet simulation, to be able to determine which constitutive models are suitable for ratcheting simulations in nuclear applications.

3. Theoretical background

3.1. Plastic deformation

Deformation can be divided in elastic and inelastic deformation where the former part is directly related to applied stress. Inelastic deformation is the deformation that remains if stress is removed. Plastic, creep and swelling deformation are examples of inelastic deformation. In this project, focus is on plastic deformation why inelastic deformation, from now on, is termed plastic deformation (or plastic strain).

Plastic deformation in metal structures occurs when the yield stress of the material is exceeded. In this project both ferritic and austenitic steels are investigated. The characteristics of the yield stress differ between these two material groups. Ferritic steels show a more distinct yield stress and yield interval while the start of yielding in austenitic steels is more diffuse.

At a microstructural level, plastic deformation in metals is associated with movement of dislocations. In a material with low yield strength, the dislocation can move relatively easy when a mechanical load is applied (simplistic view). By addition of different elements and/or heat treatment of the material, the movement of the dislocations can be restrained. This change can increase the yield strength and influence the plastic hardening characteristics.

In this project, investigated materials are regarded from a continuum mechanics perspective. This means that the micromechanical characteristics are mathematically modelled with a phenomenological approach.

3.2. Material ratcheting and structural ratcheting

Ratcheting is defined as progressive incremental plastic deformation resulting from cyclic loading. A consequence of ratcheting can be wall thinning, excessive deformation or, if proceeding too long, failure of the component. Failure caused by ratcheting is one of the failure mechanisms addressed in the ASME III code [6].

Ratcheting can be divided in material ratcheting and structural ratcheting. A steel specimen subjected to uniaxial stress cycling with a nonzero mean stress can show material ratcheting if plastic deformation occurs in both tension and compression. Material ratcheting is a phenomenon that is related to the characteristics of the material and its response at a microstructural level. For the same stress amplitude and mean stress, various steel materials show various amount of ratcheting. Figure 3-1 shows a typical stress- strain graph from a material ratcheting test. Ratchet strain is the plastic strain increment that develops during each load cycle. This measure may change as a result of cyclic hardening/softening.

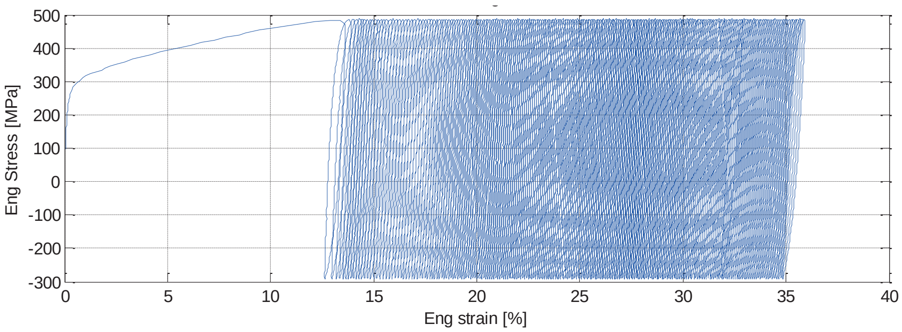

Figure 3-1 Schematic stress-strain graph from a material ratcheting test.

One of the most well-known cases where structural ratcheting can be produced is the Bree test where a pressurized cylinder is subjected to a cyclic thermal gradient through the wall thickness [7]. In this test, stresses caused by the internal pressure are constant and load controlled in contrast to the thermal stresses that are cyclic and deformation controlled. Starting from the stress state caused by the internal pressure and assuming that the load level is such that structural ratcheting is facilitated, application of the thermal gradient through the wall thickness will cause the stresses to increase in the region where temperature is lowered and decrease in the region where temperature is increased. During the first half cycle of a Bree test, one part of the wall thickness undergoes plastic deformation while the remaining part acts as a dolly and stays elastic. During the consecutive half cycle, plastic deformation occurs at the opposite side of the wall thickness. Now as the thermal cycling continues, ratcheting will occur in the cylinder resulting in thinning of the wall thickness and an increase of the diameter. The driving force causing the change in geometry in the Bree test is the internal pressure.

The most simplified structure in which structural ratcheting can be produced is the two-rod test. This structure consists of two parallel rods that are subjected to a constant primary load in combination with a cyclic secondary load. The stress state in both rods is uniaxial.

In this project, the cyclic secondary load in the two-rod test is applied as a cyclic elongation difference between the rods, see Figure 3-2. Assuming for simplicity that the material shows no plastic hardening and that the secondary stress range exceeds two times the yield stress, structural ratcheting will be produced in the rods. Here, the secondary stress range is defined as

$$\Delta\sigma_{sec} = E \cdot \Delta\delta / l_0 \qquad \text{(Eq. 3-1)}$$

where E is Young's modulus, $\Delta\delta$ is the elongation difference between the two rods and l_0 is the measuring length of the rods. At the start of the two-rod test, the constant primary load is applied resulting in tension in both rods. Subsequent application of an elongation difference between the rods will, if large enough, result in plastic deformation in the most pulled rod while the least pulled rod stays elastic. In this sequence of the test, the least pulled rod acts as a dolly. In the following half cycle, the response of the two rods will switch. As the secondary cycling continues, the averaged strain between the rods will increase caused by structural ratcheting.

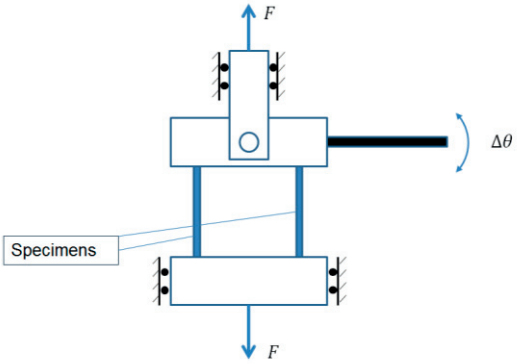

Figure 3-2 **Schematic figure of a two-rod test. Joints where the specimens are attached to the blocks are not shown.**

In summary, structural ratcheting is characterised by cyclic plastic deformation produced in a structure which is subjected to a constant driving force (pressure in the Bree test) in combination with a secondary cycling load (thermal gradient through wall thickness in the Bree test). In many cases, the response in regions of the structure alternate between elastic and plastic. The elastic part acts as a dolly during the process.

Material ratcheting and structural ratcheting are further discussed in [8].

3.3. Elastic and plastic shakedown

Shakedown of a structure occurs if ratcheting ceases after a few cycles of load application. Subsequent response is either elastic or elastic-plastic and progressive incremental plastic deformation is absent. Plastic shakedown is the case in which plastic deformation occurs during subsequent load cycling. Elastic shakedown is the case in which subsequent cyclic response is elastic.

3.4. Plastic analysis according to the ASME code

ASME Boiler & Pressure Vessel Code, section III Division 1 [6], is used for structural verification of pressure equipment in nuclear applications.

The normal route in this code is to perform the verification of the component based on elastic analysis. Criteria and their limits are adjusted in such way that local plastic deformation in the structure is considered without performing a plastic analysis.

In cases when criteria based on elastic analysis are violated, different types of plastic analysis can be applied (ASME NB-3228). Such analyses are limit analysis (ASME NB-3228.1), plastic analysis (ASME NB-3228.3) and shakedown analysis (ASME NB-3228.4).

In ASME NB-3228.4, ratcheting is addressed. Based on a plastic analysis, where the actual material stress-strain relationship is considered, the evolution of plastic strain in the structure is determined. If shakedown does not occur, an accumulated strain in a point of the structure can be accepted if it does not exceed 5%. Experimental and numerical results in this project will be compared to this strain limit.

4. Constitutive models used in the project

4.1. Constitutive modelling basics

Constitutive models in metal plasticity require a yield criterion for the virgin material and a hardening rule that governs the evolution of the yield criterion as the material undergoes plastic deformation. The initial yield criterion commonly used for metals is the von Mises yield criterion, [9], which reads

$$f\left(\sigma_{ij}\right)=\frac{3}{2}s_{ij}s_{ij}-S_y^2=0 \qquad \text{(Eq. 4-1)}$$

in which the deviatoric stress state s_{ij} is determined from

$$s_{ij}=\sigma_{ij}-\frac{1}{3}\sigma_{kk}\delta_{ij} \qquad \text{(Eq. 4-2)}$$

in which $\sigma_{kk}/3$ is the volumetric stress (or mean stress, or hydrostatic stress) and $\left[\delta_{ij}\right]=1$ if $i=j$ otherwise zero. The square root of the first term in the yield criterion is denoted effective stress i.e.

$$\sigma_e=\sqrt{\frac{3}{2}s_{ij}s_{ij}} \qquad \text{(Eq. 4-3)}$$

A corresponding measure ε_p for effective plastic strain is useful, and the plastic work equation

$$dW_p=\sigma_{ij}d\varepsilon_{ij}^p=\sigma_e d\varepsilon_p \qquad \text{(Eq. 4-4)}$$

yields the expression for the effective plastic strain increment as follows

$$d\varepsilon_p=\sqrt{\frac{2}{3}d\varepsilon_{ij}^p d\varepsilon_{ij}^p} \qquad \text{(Eq. 4-5)}$$

In the principal stress space, the mathematical formulation of the yield criterion represents a yield surface, in principal subspaces it represents a yield locus, and in the full six-dimensional stress space it represents a hypersurface. In general however, it is referred to as simply the yield surface regardless of the dimension of the considered stress space.

It has been experimentally observed that hydrostatic pressure cannot cause yielding of metals and that is why only the deviatoric stress state is involved in metal plasticity.

The physical origin of plastic deformation is atomic slips in shear planes and this is fundamentally different from elastic deformation. The total strain is the sum of elastic strain and plastic strain according to

$$\varepsilon_{ij} = \varepsilon_{ij}^{e} + \varepsilon_{ij}^{p} \qquad \text{(Eq. 4-6)}$$

The elastic strains obey simply the generalized Hooke law and are not commented upon any further herein.

If the elastic strains are subtracted from the uniaxial stress-strain curve the stress-plastic strain curve remains. The slope of that curve is

$$H_p(\varepsilon^p) = \frac{d\sigma}{d\varepsilon^p} \qquad \text{(Eq. 4-7)}$$

in which σ is the uniaxial stress and ε^p is the uniaxial plastic strain. In plasticity theory, this relationship is assumed universal regardless of the stress state i.e.

$$H_p(\varepsilon_p) = \frac{d\sigma_e}{d\varepsilon_p} \qquad \text{(Eq. 4-8)}$$

The plastic strains are path dependent i.e. their magnitude and direction depend on the loading history, not the current loading itself. Hence, they must be determined by incremental analysis. From energy considerations it can be demonstrated theoretically, and it has been experimentally verified, that the plastic strain increment vector is directed perpendicular to the yield surface i.e.

$$d\varepsilon_{ij}^{p} = d\lambda \frac{\partial f}{\partial \sigma_{ij}} \qquad \text{(Eq. 4-9)}$$

in which $d\lambda$ is a scalar multiplier which is a function of the material stress-strain curve and the direction of the stress increment in stress space. It is recognized that $d\lambda$ determines the magnitude of the plastic strain increment whereas $\partial f / \partial \sigma_{ij}$ determines its direction. The derivation of $d\lambda$ is slightly tedious and the interested reader is advised to consult the literature, [10], [11].

For monotonic loading of strain hardening materials, it is widely agreed upon that isotropic hardening renders a satisfactory accuracy in the solution of elastoplastic problems. This is the case for proportional loading as well as for non-proportional loading. Isotropic hardening means the yield surface expands isotropically in stress space as the effective stress increases due to the monotonically increased loading.

For loading involving reversing plasticity, isotropic hardening fails to capture the Bauschinger effect, [12], i.e. the decrease of strength in the direction opposite to the loading, in which the strength is increased. To remedy this shortcoming, the concept of kinematic hardening was introduced by Prager, [13], in which the yield surface size and shape remained constant during inelastic loading whereas it translates in stress space during the loading history.

Denoting the current center – commonly called back-stress – of the yield surface α_{ij}, the translated subsequent von Mises yield surface reads

$$f\left(\sigma_{ij}-\alpha_{ij}\right)=\frac{3}{2}\left(s_{ij}-\alpha_{ij}\right)\left(s_{ij}-\alpha_{ij}\right)-S_y^2=0 \qquad \text{(Eq. 4-10)}$$

Obviously the key element in the description of such subsequent yield surface is the evolution of the translation α_{ij}. For that purpose a translation rule is required. In the literature, there is a large number of constitutive models with corresponding translation rules proposed. Most models presented the last decades however stem from the model proposed by Chaboche, [4]. Chaboche in turn stems from the Armstrong-Frederick model, [5], which in turn is a modification of the original Prager model.

The Chaboche model is itself a rather advanced model, involving commonly at least seven model parameters to be determined on the basis of material testing. It was determined at the project start that no models more advanced than Chaboche should be investigated. For industrial purposes, an as simple as possible model involving a minimum of required testing and model parameters is preferred. For that reason, the models of Prager, Armstrong-Frederick and Chaboche are investigated herein. In addition to these, the Besseling model is investigated. The reason for this is partly that it is a kinematic hardening option in the Ansys finite element software [14], and partly since the anatomy of the model is different from the remaining three.

4.2. Prager linear kinematic hardening model

The Prager kinematic hardening constitute a bi-linear stress-strain curve with plastic modulus H_p. The Prager model assumes a yield surface translation as follows

$$d\alpha_{ij}=\frac{2}{3}Cd\varepsilon_{ij}^{p} \qquad \text{(Eq. 4-11)}$$

In which C is the (constant) slope of the stress-plastic strain curve i.e. C equals the plastic modulus $H_p=d\sigma_e/d\varepsilon_p$. Obviously, since there is no volumetric component of plastic strains, the translation α_{ij} of the yield surface is purely deviatoric.

The factor $2/3$ is understood as follows by considering the uniaxial case. If an increment of stress $d\sigma$ is applied, the volumetric and deviatoric portions of this stress increment are

$$\begin{bmatrix} d\sigma \\ 0 \\ 0 \end{bmatrix} = \begin{bmatrix} d\sigma/3 \\ d\sigma/3 \\ d\sigma/3 \end{bmatrix} + \begin{bmatrix} 2d\sigma/3 \\ -d\sigma/3 \\ -d\sigma/3 \end{bmatrix} \tag{Eq. 4-12}$$

Hence if the stress state moves $\begin{bmatrix} d\sigma & 0 & 0 \end{bmatrix}^T$, the yield surface must translate $\begin{bmatrix} 2d\sigma/3 & -d\sigma/3 & -d\sigma/3 \end{bmatrix}^T$ in the deviatoric plane in order for the stress state to still be on the yield surface and hence

$$d\alpha = \frac{2}{3}d\sigma = \frac{2}{3}H_p d\varepsilon^p \tag{Eq. 4-13}$$

4.3. Armstrong-Frederick kinematic hardening model

The Armstrong-Frederick model is similar to the Prager model but the translation rule is modified with a recall term according to

$$d\alpha_{ij} = \frac{2}{3}Cd\varepsilon_{ij}^p - \gamma\alpha_{ij}d\varepsilon_p \tag{Eq. 4-14}$$

The recall term makes the evolution of the back-stress α_{ij} non-linear and hence the plastic modulus H_p is no longer constant as in the Prager model. The parameter C denotes the plastic modulus at the onset of plasticity.

The Armstrong-Frederick is hence a three-parameter model with parameters C, γ and S_y. The model is better able to adjust to real stress-strain curves than the Prager model. For the case of $\gamma = 0$ it degenerates to the Prager model and for the case of $\gamma \to \infty$ it degenerates to the perfectly plastic model. Moreover, the uniaxial stress-strain curve following from the translation rule saturates when

$$d\alpha = \frac{2}{3}Cd\varepsilon^p - \gamma\alpha d\varepsilon_p = 0 \tag{Eq. 4-15}$$

which, since in the uniaxial case $d\varepsilon_p = d\varepsilon^p$ and $\alpha = 2\Delta\sigma/3$ in which $\Delta\sigma$ is the amount of strain hardening, yields saturation of stress at

$$\sigma_{bound} = S_y + C / \gamma \qquad \text{(Eq. 4-16)}$$

i.e. the strain hardening amounts to $\Delta\sigma = C / \gamma$.

Another advantage of the Armstrong-Frederick over the Prager model is that it is able to simulate ratcheting in asymmetrical uniaxial stress cycling and related phenomena such as stress relaxation in strain cycling – these phenomena being experimentally observed material behavior. The Armstrong-Frederick model is however known to overestimate the rate of ratcheting in such uniaxial cycling.

4.4. Chaboche kinematic hardening model

Although the Armstrong-Frederick model is better able to adjust to real stress-strain curves than the Prager model, it is not able to adjust to a general strain hardening material stress-strain curve. In order to remedy that, Chaboche introduced the concept of several superimposed Armstrong-Frederick translations according to

$$d\alpha_{ij} = \sum_{k=1}^{n} \left\{ \frac{2}{3} C_k d\varepsilon_{ij}^{p} - \gamma_k \alpha_{ij} d\varepsilon_p \right\} \qquad \text{(Eq. 4-17)}$$

In general, the stress-strain curve exhibits three indistinct phases. The first is related to the initiating of plasticity in which the slope is steep, the second is a transition phase that corresponds to a knee in the stress-strain curve, and the third is characterised by a constant or near constant slope. Letting each of these phases be characterised by an Armstrong-Frederick translation allows for the simulation of arbitrary stress-strain curves of strain hardening metals.

Moreover, the Chaboche model has the potential to better capture ratcheting in asymmetrical uniaxial stress cycling – and related phenomena – than the Armstrong-Frederick model.

4.5. Besseling multi-linear kinematic hardening model

The Besseling multi-linear kinematic hardening model is fundamentally different from the kinematic models described above. Rather than introducing the Bauschinger effect by a translation of the yield surface, the Besseling model generates a Bauschinger effect by dividing the material into sub-volumes of elastic-perfectly plastic materials, hereafter called EPP materials, with different yield strengths thereby creating a piecewise linear stress-strain curve. This in fact reflects the internal mechanics of poly-crystalline materials.

The differences in comparison to the kinematic models above are elaborated to some extent as follows. Consider Figure 4-1 below in which the response of three EPP materials with yield strengths 100, 200 and 300 MPa, respectively, are subjected to a strain history going from zero to 0.2 % tension whereafter the loading is reversed to 0.2 % compression.

Now, consider a Besseling material composed of 1/3 of each of these EPP materials. At any strain, the Besseling material stress is then the mean of the three EPP stresses in Figure 4-1 and the Besseling material behaves as shown in Figure 4-2. The Baushinger effect is obviously accounted for and the behavior is kinematic although neither of the yield surfaces involved may translate since the involved materials do not strain harden.

In order to understand the kinematic behavior of a set of EPP materials, consider the stresses following the strain history from zero to 0.2 % tension followed by reversing to 0.1 % tension. At 0.1 % tension in the reversed phase the stress in the Besseling material is zero as seen in Figure 4-2. However, the stresses in the individual EPP materials are 100 MPa compression, zero, and 100 MPa tension, respectivey.

Hence, at reversal, residual stresses are built into the sub-volumes. This resembles the mechanism of the Bauschinger effect in poly-crystalline materials, the mechanism being the formation of residual stresses within the material.

Effectively, therefore, in a Besseling model there are stress state translations in each sub-volume instead of yield surface translations and this distinguishes it from the remainder of kinematic constitutive models for cyclic plasticity.

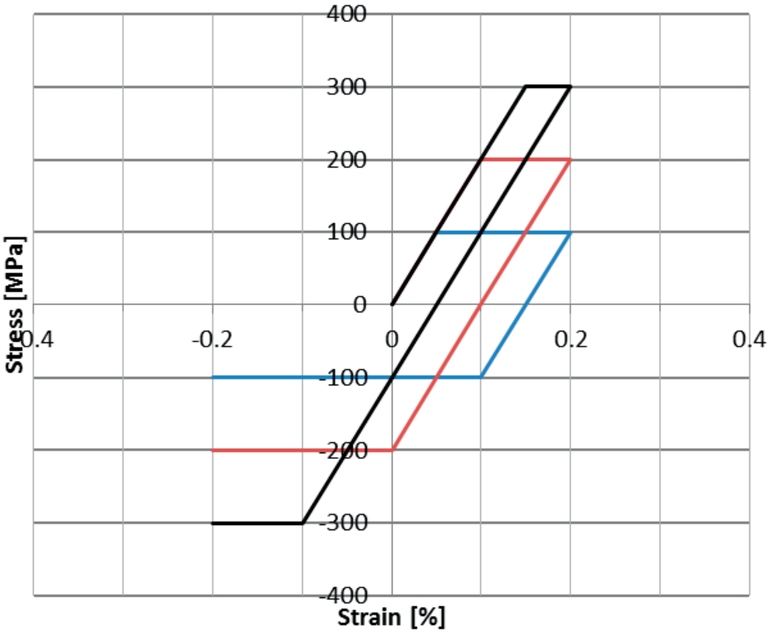

Figure 4-1 Three EPP materials with yield strengths 100, 200, and 300 MPa subjected to strain history zero to 0.2 % tension and reversed to 0.2 % compression.

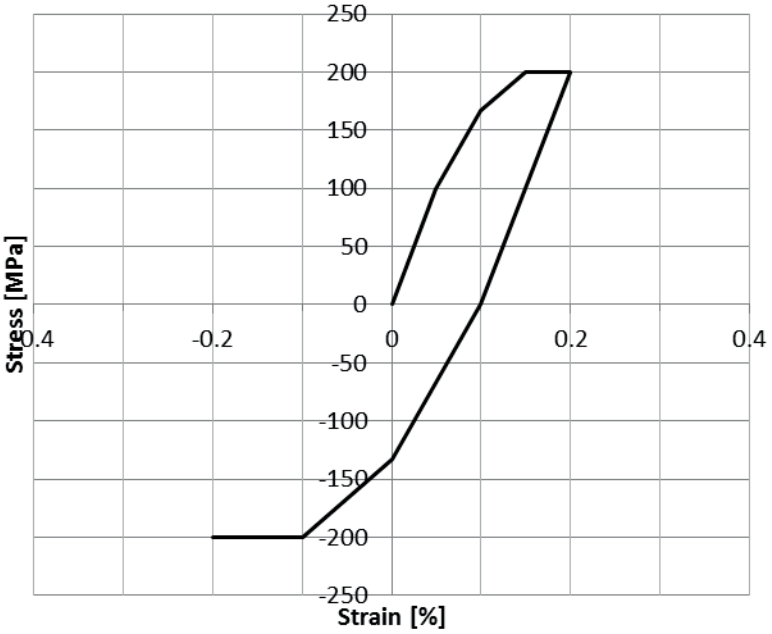

Figure 4-2 Resulting response for a Besseling material composed of 1/3 of each material in Figure 4-1.

The fact that there are no yield surface translations must be considered an advantage since there is little experimental evidence available on the translation of subsequent yield surfaces for general stress states – thus all proposed translation rules are merely assumptions.

It should be pointed out that in uniaxial loading, the model behaves identically to the multi-surface model of Mroz, [3], but for general stress states the models differ since the Mroz model includes a translation rule for the involved yield surfaces.

Consider the stress-strain curve in Figure 4-3 below. In a Besseling material, a sub-volume α_1 of the material has yield strength $S_{y1} = \sigma_1$ whereas the sub-volumes $\alpha_2, \alpha_3 ... \alpha_k$ have yield strengths $S_{y2}, S_{y3},,, S_{yk}$. These parameters are determined so as to fit the material stress-strain curve. All sub-volumes are subjected to the same total strain and hence

$$S_{yi} = E\varepsilon_i \qquad \text{(Eq. 4-18)}$$

Moreover it holds

$$\alpha_k = \frac{E_{Tk}}{E} \qquad \text{(Eq. 4-19)}$$

$$\alpha_{k-1} + \alpha_k = \frac{E_{Tk-1}}{E} \qquad \text{(Eq. 4-20)}$$

$$\alpha_{k-2} + \alpha_{k-1} + \alpha_k = \frac{E_{Tk-2}}{E} \qquad \text{(Eq. 4-21)}$$

and so forth and hence it may be written

$$\alpha_i = \frac{E_{Ti}}{E} - \sum_{i+1}^{k} \alpha_j \qquad \text{(Eq. 4-22)}$$

in which $i = 1,,, k$ and by which α_k is the first to be determined. Ansys limits the number of the stress-strain points to $k \leq 20$ which effectively means that any stress-strain curve may be modeled very accurately without appearance of piecewise linearity.

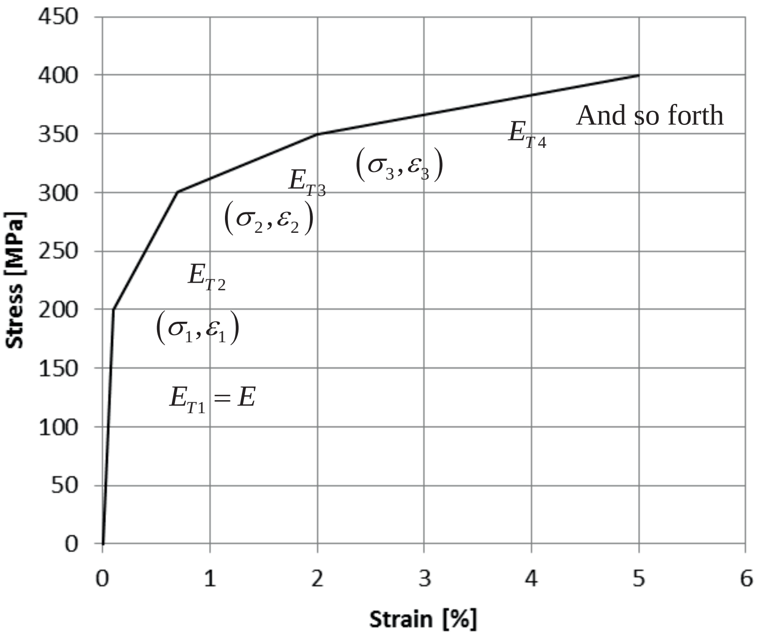

Figure 4-3. Example of multi-linear stress-strain curve.

5. Two-rod test

5.1. General

Structural ratcheting can be investigated experimentally in a number of ways. The two-rod test makes it possible to produce structural ratcheting with a simple structure where the specimens are subjected to a uniaxial stress state.

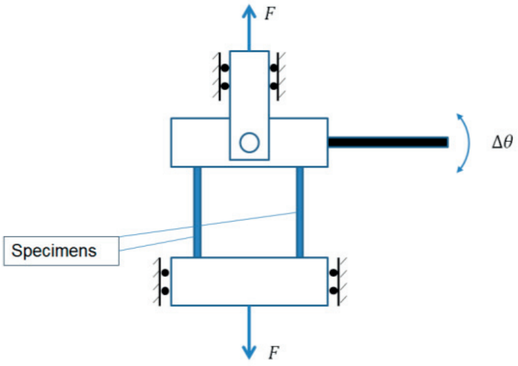

Figure 5-1 **Schematic figure of the first developed two-rod test rig. Joints where the specimens are attached to the blocks are not shown.**

In this project, the two-rod test was developed in two steps. In the first experimental setup, one test machine is used. Figure 5-1 shows a schematic figure where the two specimens are attached to one upper and one lower block. The constant force F is applied by the test machine that pulls the two blocks apart from each other. The cyclic deformation controlled difference in elongation between the two specimens is introduced by cycling the angle θ of the upper block. Figure 5-2 shows one special designed specimen and Figure 5-3 shows a close-up photo of the experimental setup in the test machine. A comparison of Figure 5-1 and Figure 5-3 reveals that the schematic figure is turned upside-down.

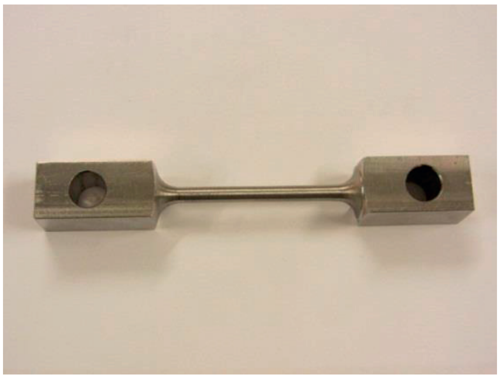

Figure 5-2 **Special designed specimen for the first developed two-rod test setup.**

Initial tests with the first developed two-rod test setup worked satisfactorily and showed that structural ratcheting could be produced as expected. However, there were a number of drawbacks. In order to determine the stress in the individual specimen, a strain gage had to be attached to each specimen. Furthermore, a system for controlling the angel θ had to be developed.

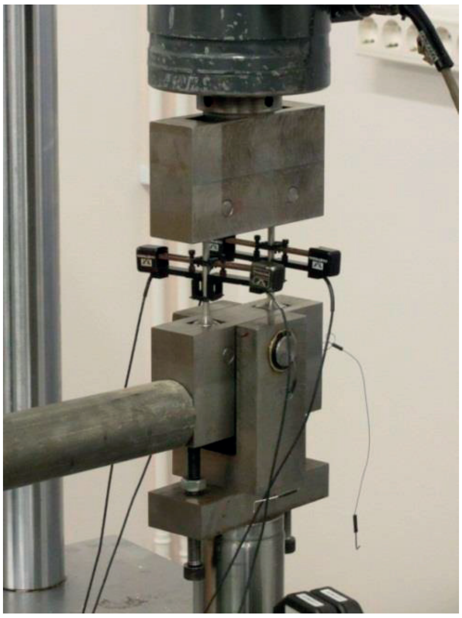

Figure 5-3 **Close-up photo of the first (and rejected) two-rod experimental setup.**

In the second two-rod experimental setup, two testing machines are used in parallel with one specimen in each, see Figure 5-4. The difference between signals from the two extensometer pairs and the sum of the forces in the two load cells are used to control of the testing machines. The advantage with this approach is that standard specimens can be used, the force in the individual specimen is given directly and that the arrangement for controlling the movement of the lever arm is not needed. This developed two-rod test setup is used in this project. More details about the test and test procedure are given below.

Figure 5-4 **Two-rod experimental setup with two test machines.**

5.2. Material characterisation

Four different tests are conducted for characterisation of the two investigated materials P265 and 316L. These tests are tensile test, tensile test with unloading, fully-reversed strain controlled cycling test and material ratcheting test.

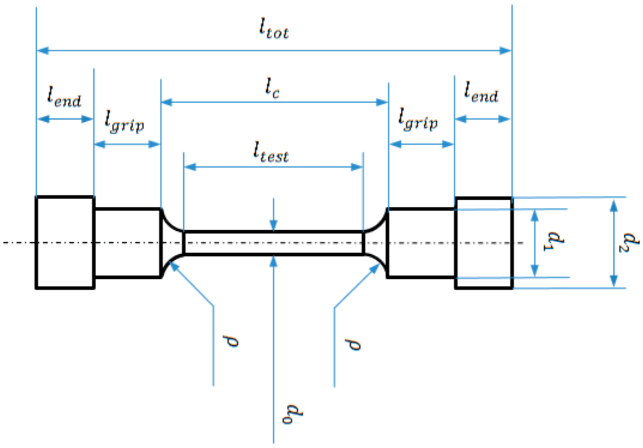

Figure 5-5 **Specimen geometry.**

The geometry of the specimens used is shown in Figure 5-5 and Table 5-1. The fully-reversed strain controlled cycling test and the material ratcheting test requires stiffer specimens than the tensile test and the tensile test with unloading. The cross section of the specimens is round with varying length and diameter. The specimen geometry is chosen according to the ASTM E606 standard [15]. All specimens are made uniform within 0.01 mm diameter tolerance throughout the length l_{test}.

Table 5-1 Specimen geometry values. Geometry 1 is used for the tensile test and the tensile test with unloading. Geometry 2 is used for the fully-reversed strain controlled cycling test and the material ratcheting test.

	d_0	l_{test}	l_c	l_{grip}	l_{end}	l_{tot}	d_1	d_2	ρ
Geometry 1	6	30	35	12	11	80	10	13	5
Geometry 2	7	18	26	12	11	75	10	13	6.08

The specimens are clamped to the machine head (1) using a ring (2) and a wedge (3) as illustrated in Figure 5-6. This fixture is used for support in both compression and tension. When the bolts are tightened against the machine head, the fixture ring (2) slides relative to the fixture wedges (3) which clamp the specimen.

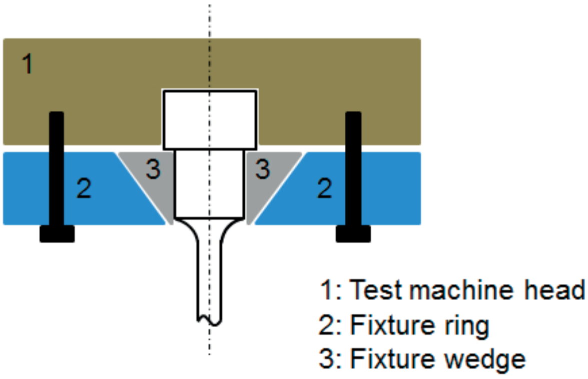

Figure 5-6 Test specimen fixture.

The material characterisation is performed on MTS312.21 load frames with a 100 kN load cell and INSTRON 8500 controls recorded by a computer. The specimen strain measurements are done by use of two 12.5 mm extensometers fastened on opposite sides of the specimen as shown in Figure 5-7. The mean value of the two extensometers is recording. All tests are conducted at room temperature.

Figure 5-7 **A close-up photo of the specimen, specimen fixture and extensometers.**

5.2.1. Material characterisation of P265

Specimens for characterisation of the ferritic steel P265 are all machined from the same steel plate. All tests are performed with specimens taken out in the rolling direction of the plate except for the tensile test where also a specimen taken out in the transversal direction of the rolling direction is tested. Chemical composition of the tested P265 is given in Table 5-2.

Table 5-2 **Chemical composition of the tested ferritic steel P265.**

	C	Si	Mn	P	S	N	Al	Cu	Cr	Ni
[%]	0.16	0.17	0.89	0.012	0.003	0.004	0.039	0.02	0.04	0.03

	Mo	V	Ti	Nb
[%]	0.01	0.003	0.002	0.002

P265 - Tensile testing

Tensile tests are conducted in both the rolling direction and perpendicular to the rolling direction. A strain rate of 0.05%/s is used. Specimen geometry is given in Table 5-1. As seen in Figure 5-8, the degree of anisotropy is very small up to a strain level of 22%. Averaged yield stress in the rolling direction equals 298 MPa. For this material $S_y = R_{p,0.2} = 298$ MPa.

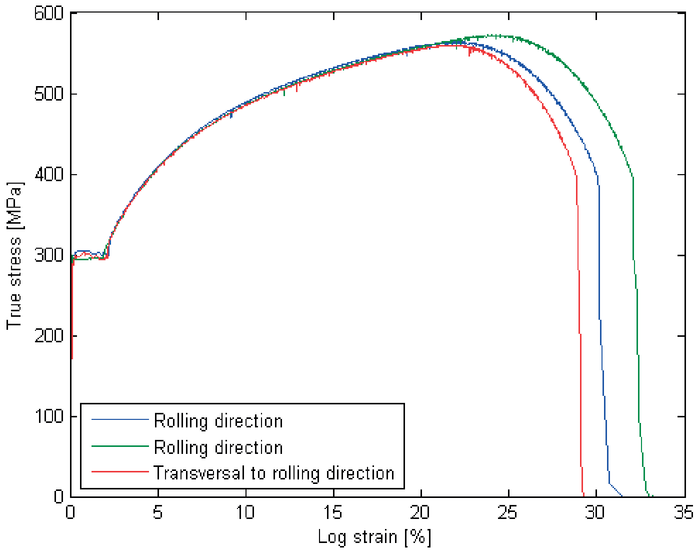

Figure 5-8 Tensile test results for the ferritic steel P265.

P265 - Tensile testing with unloading

For the two-rod tests conducted in this project, plastic deformation in the specimens occurs only in tension at the start of the test. Depending on material characteristics, primary stress σ_{prim} and secondary stress range $\Delta\sigma_{sec}$ plastic deformation may also occur in compression as the test continues.

In order to understand the response of the material if cyclic plastic deformation occurs only in tension, a tensile test with unloading is conducted. After each strain increment of 0.2%, the specimen is unloaded by one yield stress. Strain rate used in the test is 0.005%/s. This corresponds to the strain rate used in the two-rod tests. Specimen geometry is given in Table 5-1. Figure 5-9 shows that the plastic hardening is somewhat reduced for the tensile test with unloading compared to that for the tensile test. This difference might be explained by the fact that the tensile test is conducted at a strain rate of 0.05%/s resulting in a slightly higher plastic hardening. Further investigations on this issue are not done within this project.

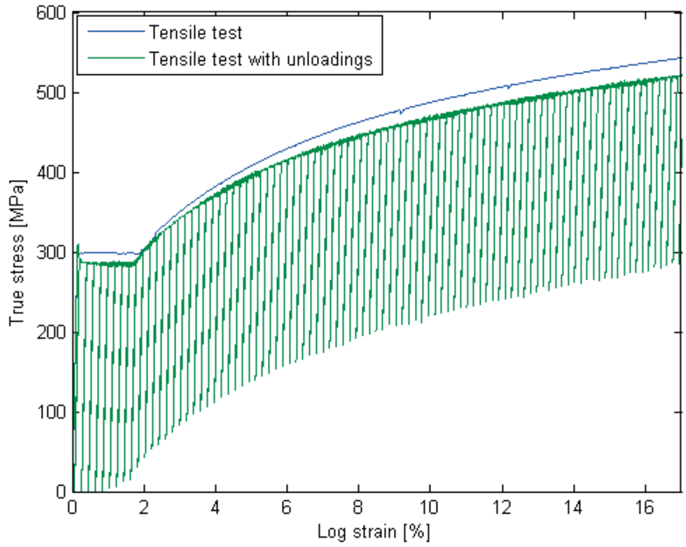

Figure 5-9 P265 tensile test with unloading.

P265 - Fully-reversed strain controlled cycling

Fully-reversed strain controlled cycling tests are conducted with specimens taken out in the rolling direction of the plate. Tests are performed with strain amplitudes of 0.5, 1, 1.5 and 2%. A saw-tooth displacement at a strain rate of 0.005%/s controls the tests. Specimen geometry is given in Table 5-1. Results are given in Figure 5-10 to 5-13. Cyclic hardening can be noticed for tests with a strain amplitude of 1% or more.

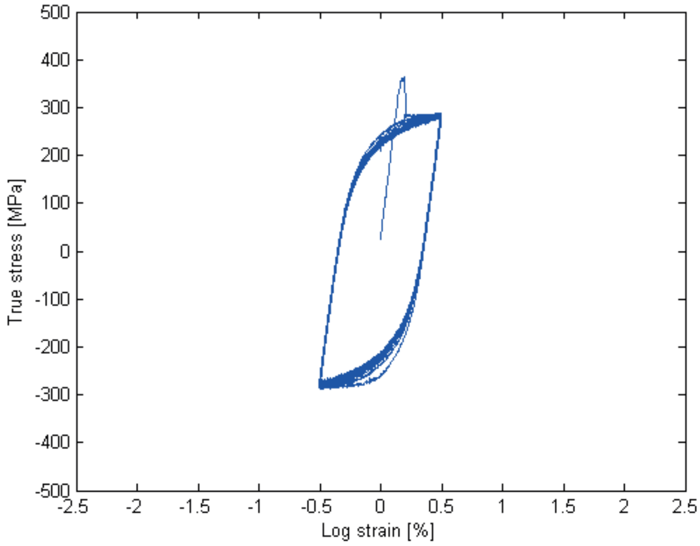

Figure 5-10 Fully-reversed strain cycling test with 0.5% strain amplitude.

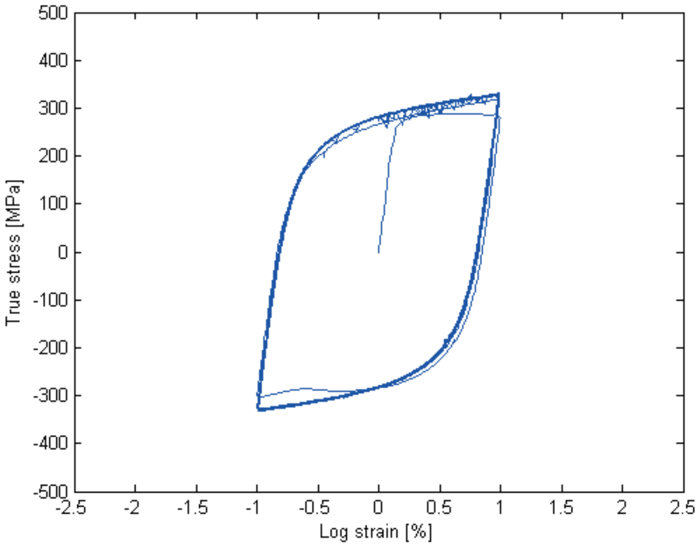

Figure 5-11 Fully-reversed strain cycling test with 1.0% strain amplitude.

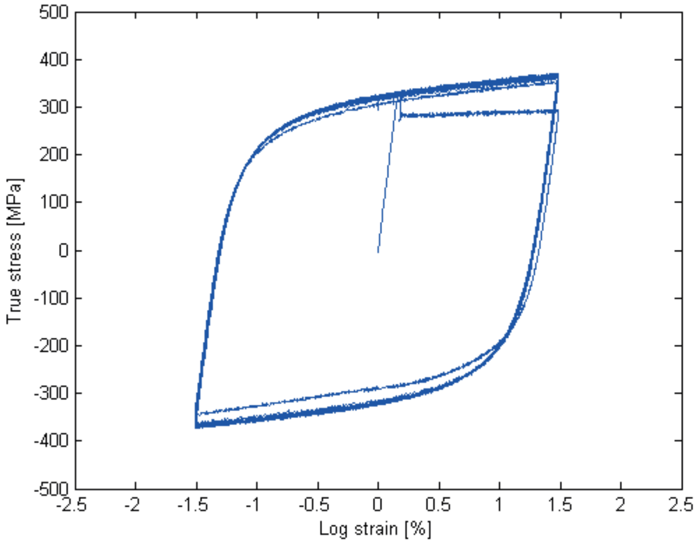

Figure 5-12 Fully-reversed strain cycling test with 1.5% strain amplitude.

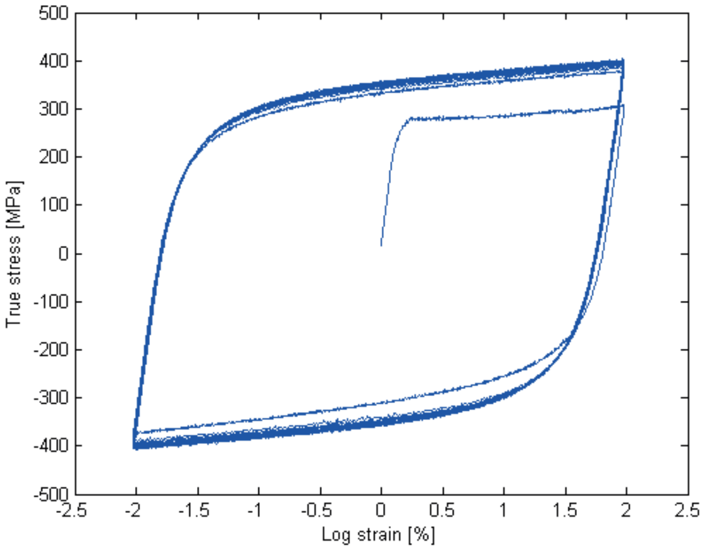

Figure 5-13 **Fully-reversed strain cycling test with 2.0% strain amplitude.**

Saturated stress-plastic strain loops are used for determination of constants in the nonlinear kinematic hardening models. Figure 5-14 shows half of these loops for the different cyclic tests performed.

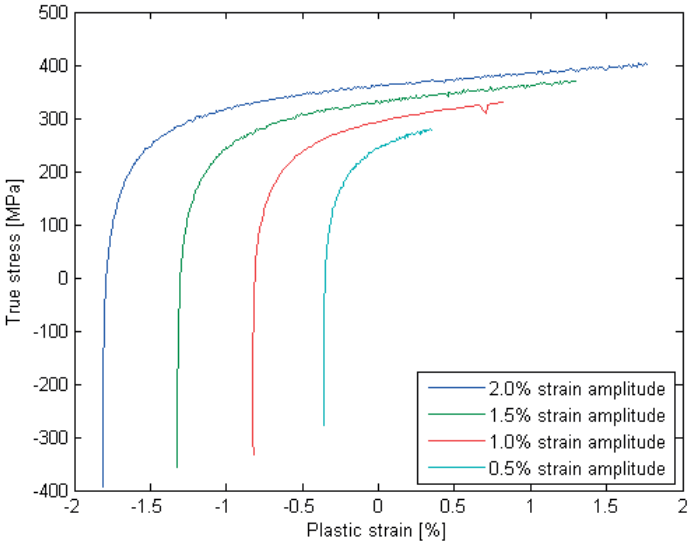

Figure 5-14 **Half of the saturated stress-plastic strain loops from the different fully-reversed strain cycling tests conducted on P265.**

5.2.2. Material characterisation of 316L

Specimens for characterisation of the austenitic steel 316L are all machined from the same steel plate. The rolling direction of the plate is not known why one of the directions is called the main direction. All but one specimen is taken out in the main direction. One tensile test is performed with a specimen taken out transversal to the main direction. Chemical composition of 316L is given in Table 5-3.

Table 5-3 Chemical composition of the austenitic steel 316L.

	C	Mn	Si	P	S	Cr	Mo	Ni	N	Fe
Wt. % min	-	-	-	-	-	16.0	2.0	10.0	-	rem.
Wt. % max	0.03	2.0	0.75	0.045	0.03	18.0	3.0	14.0	0.1	rem.

Tested 316L steel material has been investigated in an earlier project [16]. Material characterisation test results from the present project have been compared to corresponding results from the earlier project and found to agree well.

316L - Tensile testing

Tensile tests are conducted in the main direction and perpendicular to the main direction. A strain rate of 0.05%/s is used. Specimen geometry is given in Table 5-1. As seen in Figure 5-15, the degree of anisotropy is small up to a strain level of 50% and the material is shown to be very ductile. Averaged parameters from the tensile tests are presented in Table 5-4.

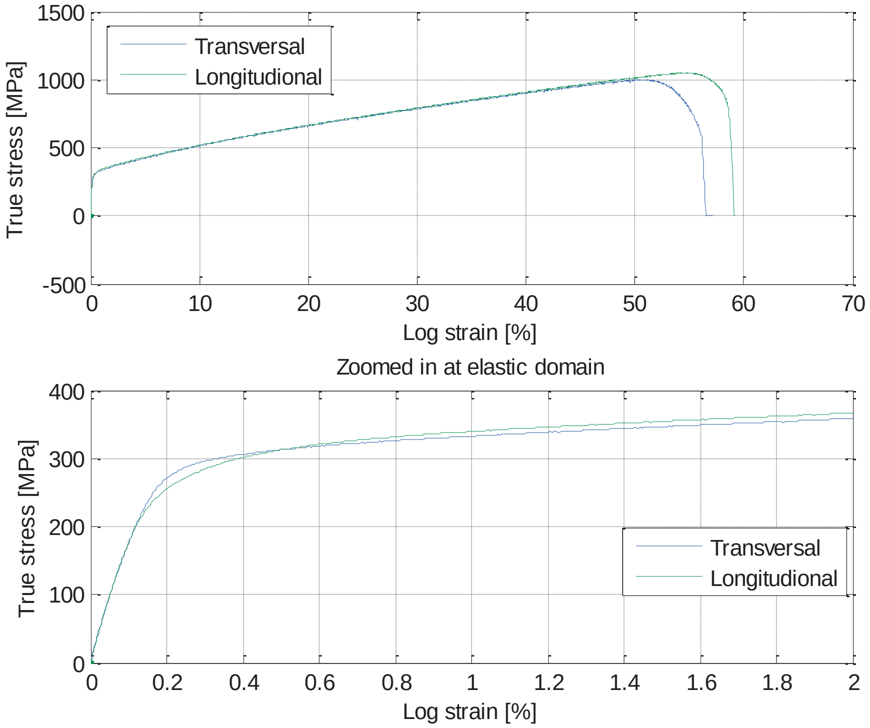

Figure 5-15 Tensile test results for the austenitic steel 316L.

Table 5-4 Averaged material parameters tensile tests.

E	$R_{p,0.2}$ (S_y)	R_M	A_5	Z
197 GPa	293 MPa	614 MPa	80%	89%

316L - Fully-reversed strain controlled cycling

Fully-reversed strain controlled cycling tests of the material are conducted to evaluate the cyclic behaviour with strain amplitudes 0.25, 0.5 and 1%. A saw-tooth displacement at a strain rate of 0.01%/s controls the tests. Specimens are taken out in the main direction of the plate with geometry according to Table 5-1. Results are given in Figure 5-16 where an extensive cyclic hardening can be seen, especially for 1% strain amplitude. The results show good correspondence with corresponding test results in [16].

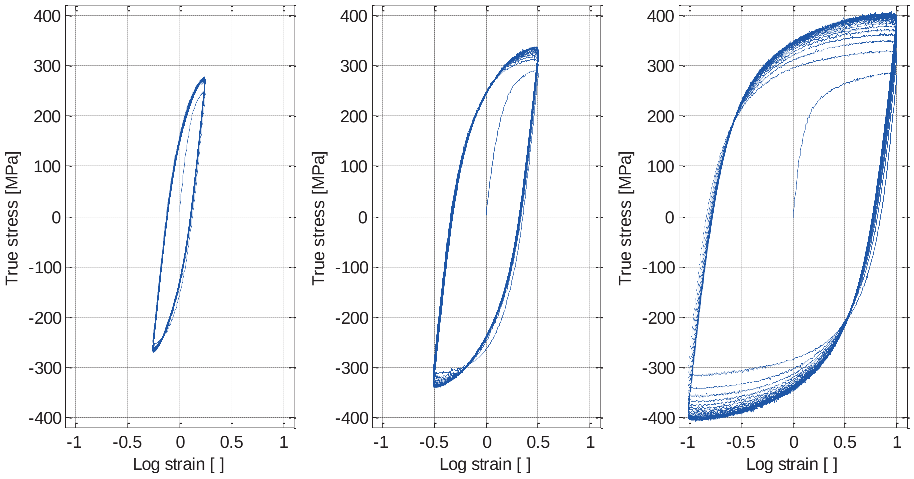

Figure 5-16 **Fully-reversed strain controlled cycling at strain amplitudes 0.25%, 0.5% and 1%.**

Saturated stress-strain loops are extracted from results presented in Figure 5-16 and later used for the nonlinear kinematic hardening models. Figure 5-17 shows saturated hysteresis loops for 316L.

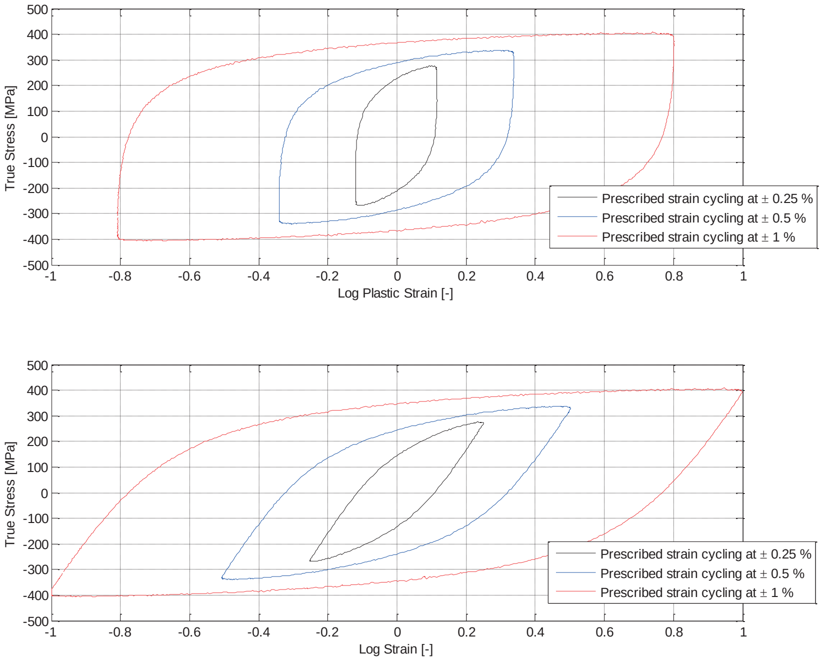

Figure 5-17 **Saturated hysteresis loops for the three cyclic strain amplitudes. Upper: Stress versus plastic strain. Lower: Stress versus strain.**

316L - Influence of strain rate on fully-reversed strain controlled cycling

All fully-reversed strain controlled cycling tests on 316L were conducted at a strain rate of 0.01 %/s before it was found out that the control system of the two-rod test did not allow a strain rate higher than 0.005 %/s. In order to understand the impact of the strain rate, the strain rate dependency is evaluated over the interval 0.01-0.0025 %/s. Specimen geometry 2 in Table 5-1 is used for three fully-reversed strain controlled cycling tests with a strain amplitude of 0.5%. The saturated cycles for three different strain rates are presented in Figure 5-18. As can be seen, a strain rate within 0.0025 %/s and 0.01 %/s has negligible influence in the stress-strain response. As no trend can be seen, the differences between the saturated loops can instead be used as a measure of the repeatability in the fully-reversed strain cycling tests.

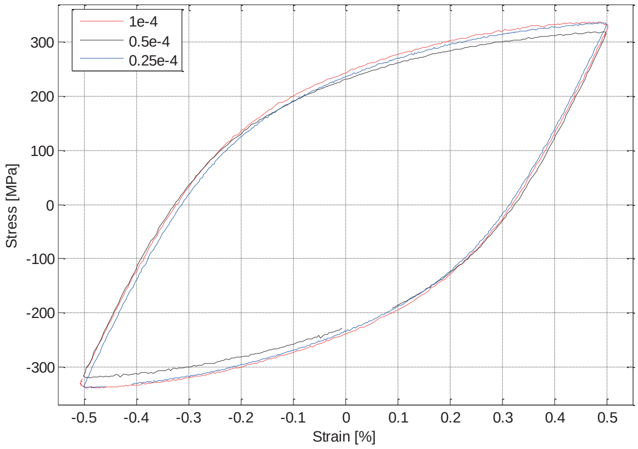

Figure 5-18 Strain rate dependency test.

5.3. Determination of S_m value

Load combinations used for the two-rod tests performed are given as multiples of the ASME design stress intensity value S_m. Based on results from tensile testing of the two materials P265 and 316L, the S_m value is determined as

$$S_m = \frac{2}{3} \cdot R_{p,0.2} \qquad \text{(Eq. 5-1)}$$

Table 5-5 S_m value for P265 and 316L.

	S_m
P265	199 MPa
316L	195 MPa

5.4. Two-rod test setup

5.4.1. Investigated load combinations

The two-rod test load combinations investigated for P265 and 316L are shown in Table 5-6 and 5-7, respectively. Primary stress σ_{prim} is a load controlled constant stress that is applied at both specimens. Secondary stress range $\Delta\sigma_{sec}$ corresponds to the displacement controlled difference in displacement $\Delta\delta$ between the specimens given as

$$\Delta\delta = \frac{\Delta\sigma_{sec}}{E} \cdot l_{ext} \qquad \text{(Eq. 5-2)}$$

where E is Young's modulus and l_{ext} is the measuring length of the specimens, i.e. the distance between extensometer knife edges.

Table 5-6 Two-rod test load combinations investigated for P265. S_m equals 199 MPa.

Primary stress (σ_{prim})	Secondary stress range ($\Delta\sigma_{sec}$)
0.5 S_m	3 S_m, 6 S_m, 9 S_m
S_m	3 S_m, 6 S_m, 9 S_m
1.25 S_m	2 S_m, 3 S_m, 6 S_m

Table 5-7 Two-rod test load combinations investigated for 316L. S_m equals 195 MPa.

Primary stress (σ_{prim})	Secondary stress range ($\Delta\sigma_{sec}$)
0.5 S_m	3 S_m, 4.5 S_m, 6 S_m, 9 S_m
S_m	2 S_m, 3 S_m, 4.5 S_m, 6 S_m, 9 S_m
1.25 S_m	S_m, 2 S_m, 3 S_m, 6 S_m

5.4.2. Test specimens

Geometry of two-rod specimens is show in Figure 5-19 and Table 5-8. The length of the P265 specimen is 5 mm longer than that of the 316L specimen. This difference has no influence on the results.

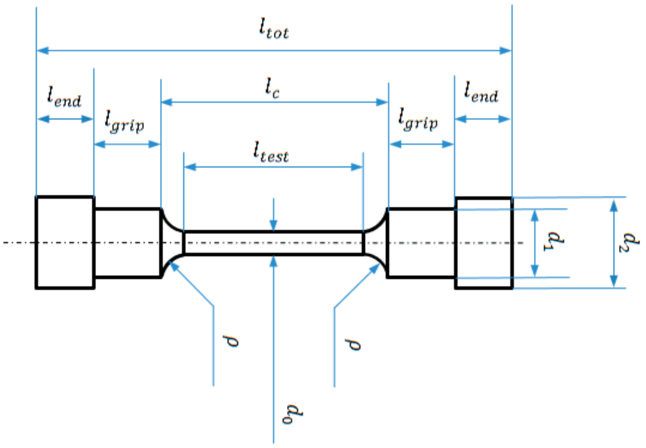

Figure 5-19 Specimen geometry.

Table 5-8 Geometry values for two-rod test specimens.

	d_0	l_{test}	l_c	l_{grip}	l_{end}	l_{tot}	d_1	d_2	ρ
P265	6	30	35	12	11	80	10	13	5
316L	6	25	30	12	11	75	10	13	5

5.4.3. Control system

When a test is running, the computer controls the cyclic displacement of the specimens measured by the extensometers. A primary routine checks the length difference between the two specimens at the end of each half-cycle. Converted to strain, this difference is denoted $\Delta\varepsilon_{sec}$. The primary routine has the following outline (for half-cycle N running from $t = t_N$ to $t = t_{N+1}$):

- Strain rate for specimen 1: $\dot{\varepsilon}_1 = \frac{\Delta\varepsilon_{sec}}{t_{N+1} - t_N}(-1)^N$
- Strain rate for specimen 2: $\dot{\varepsilon}_2 = \frac{\Delta\varepsilon_{sec}}{t_{N+1} - t_N}(-1)^{N+1}$
- $\varepsilon_1(t) = \int_{t_N}^{t} \dot{\varepsilon}_1 dt + \varepsilon_1(t_N)$
- $\varepsilon_2(t) = \int_{t_N}^{t} \dot{\varepsilon}_2 dt + \varepsilon_2(t_N)$.

Another routine is responsible for holding the sum of the two loads on the specimens constant. This routine consists of a loop which is running without stopping, slightly altering the output signal $\varepsilon_1(t)$ and $\varepsilon_2(t)$. The outline of the loop is described in Figure 5-20.

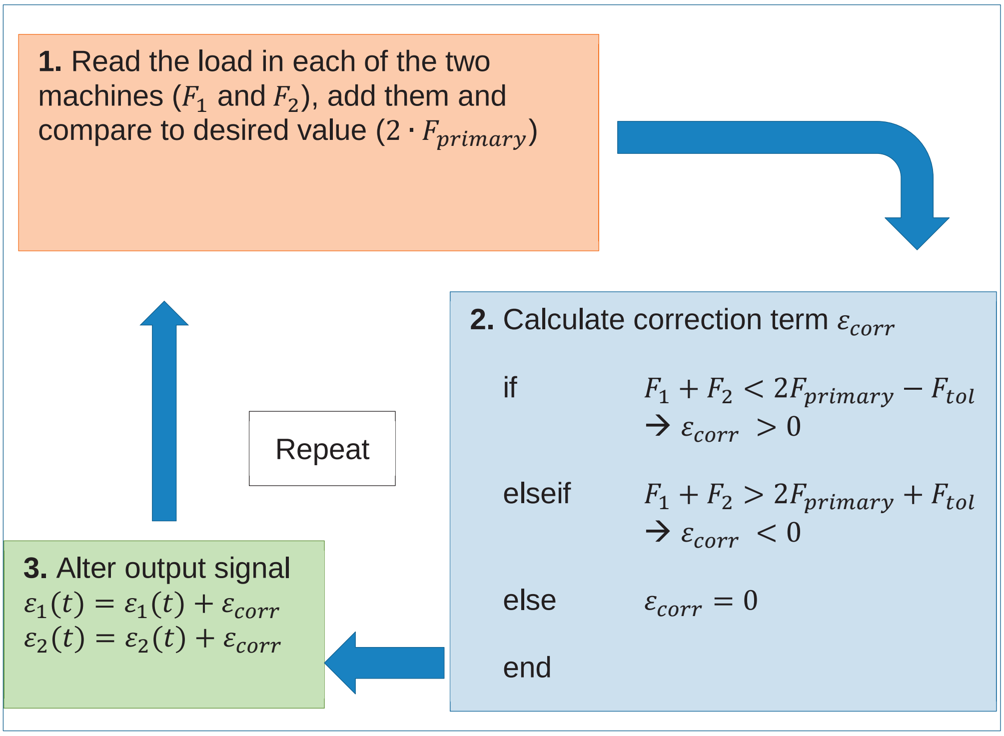

Figure 5-20 Scheme over regulation algorithm controlling the sum load in two-rod tests.

Calculation of the corrective term ε_{corr} is done proportionally to the error (P-control). Due to a delay in the response time, the corrective term is bounded to a maximal correction. As apparent in the scheme above, if the difference of the forces and the desired force is within a tolerance, F_{tol}, no alteration is made. This tolerance is set to 90 N. Since these two regulations are conducted independently, the specimens are allowed to elongate successively with increasing cycles.

At the end point of each half-cycle, data is recorded. This includes

- Piston position for machine 1 and 2,
- Extensometer position for specimen 1 and 2,
- Piston force readings for machine 1 and 2.

Between the ends of each half-cycle, no data is recorded. However, when the test is running, the force in machine 1 and 2 is visualized in an oscilloscope in real-time. Furthermore, an electric circuit is made to show the mean force of machine 1 and 2 in real-time.

5.5. Experimental results from two-rod tests

5.5.1. P265

Results from two-rod testing of P265 are shown in Figure 5-21 to 5-23. Average strain of the two specimens is given as a function of the number of cycles. For comparison reasons corresponding results for 316L are included in the figures. Generally, P265 shows more ratcheting than 316L does. This is pronounced for higher secondary stress ranges and for a primary stress $\sigma_{prim} \geq S_m$. Worth to mention is that P265 has a tendency to break when reaching about 27% strain.

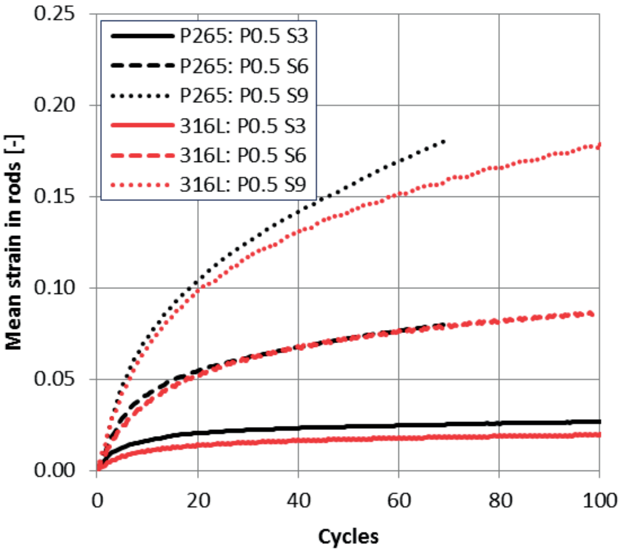

Figure 5-21 Two-rod test results for primary load $0.5\ S_m$ and secondary stress range according to legend. Average strain of the two specimens is given as function of number of cycles. S3 equals a secondary stress range of $3\ S_m$.

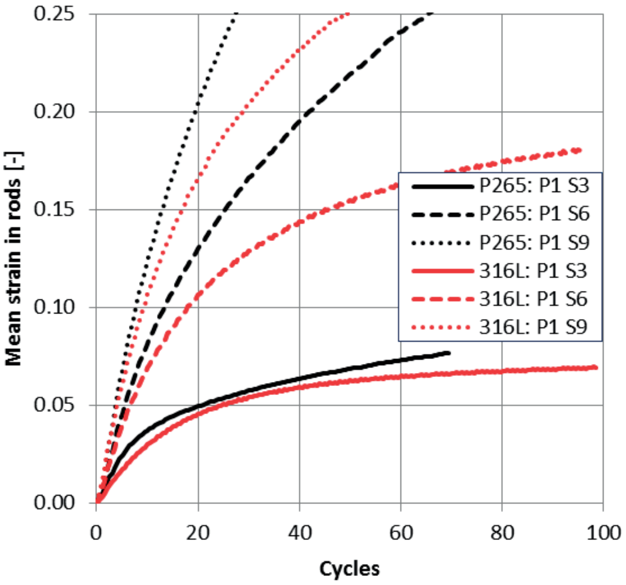

Figure 5-22 Two-rod test results for primary load S_m and secondary stress range according to legend. Average strain of the two specimens is given as function of number of cycles. S3 equals a secondary stress range of $3\ S_m$.

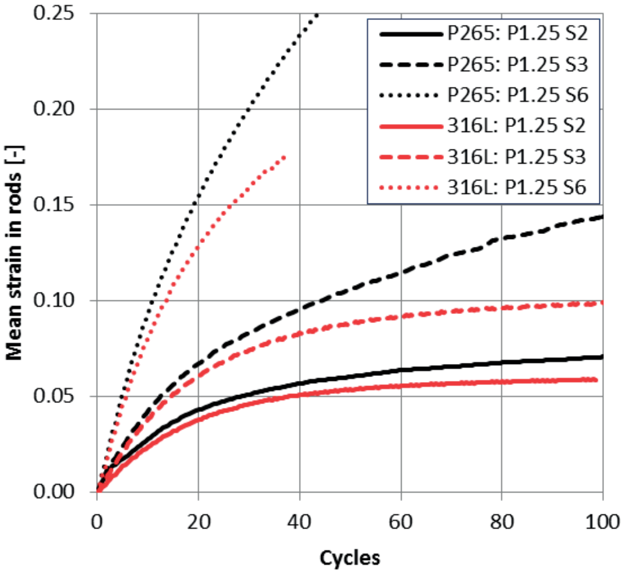

Figure 5-23 Two-rod test results for primary load $1.25\ S_m$ and secondary stress range according to legend. Average strain of the two specimens is given as function of number of cycles. S3 equals a secondary stress range of $3\ S_m$.

5.5.2. 316L

The result from the two-rod tests of 316L is presented in Figure 5-24. Average strain of the two specimens is given as function of number of cycles. For each primary stress level, the different tests with varying secondary stress range are compared. Each secondary stress range level corresponds to a specific colour in Figure 5-24.

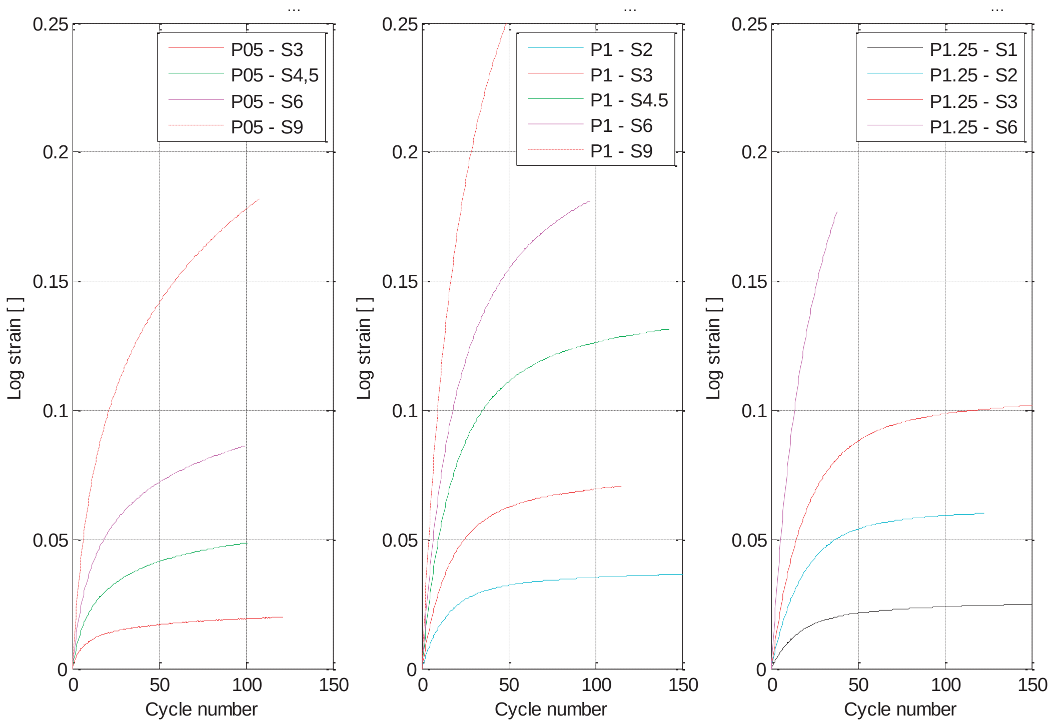

Figure 5-24 Two-rod test results for 316L. Average strain of the two specimens is given as function of number of cycles. P05 equals a primary stress of $0.5\ S_m$. S3 equals a secondary stress range of $3\ S_m$.

5.5.3. Evaluation of two-rod test results

All two-rod tests show a ratcheting rate that is highest at start of the test and declines as the test continues. At the beginning, the material is virgin and no plastic hardening has occurred. This explains the higher ratcheting rate at start. The following plastic hardening, as the specimens are plastically deformed, will decrease the ratcheting rate. Plastic hardening of P265 and 316L differs. The effect of this can for example be seen in Figure 5-22 and 5-23 where the ratcheting rate is higher for P265. It is obvious that the primary stress and the secondary stress range are important factors for the two-rod test response. An increase of σ_{prim} or $\Delta\sigma_{sec}$ increases the ratcheting rate. If $\Delta\sigma_{sec} \leq 2\ S_y$, elastic shakedown will eventually occur. If $\Delta\sigma_{sec} > 2\ S_y$, plastic shakedown might eventually occur. However, for the load combinations investigated it is expected that ratcheting would continue until failure of the specimens.

The ASME NB-3228.4 criterion of 5% for accumulated strain is exceeded for many of the two-rod tests. The number of consecutive cycles without failure, after the 5% strain criterion has been reached, indicate that the criterion gives an adequate margin.

5.6. Numerical simulation of two-rod tests

The possibility to simulate the response of a two-rod test depends on the material characteristics, the load level and load combination as well as the constitutive model used. In this project four constitutive models are investigated, i.e. a bi-linear kinematic hardening model (Prager), a multi-linear kinematic hardening model (Besseling), Armstrong-Frederick nonlinear kinematic hardening model and Chaboche nonlinear kinematic hardening model. The ideal plastic material model is also investigated as a special case of the bi-linear model. A general discussion about the different models possibility to simulate a two-rod test is given below. The finite element program ANSYS version 15.0 [14] is used for simulation of the two-rod tests.

Bi-linear material model (Prager)

Three constants define the bi-linear kinematic hardening model (assuming Poisson's ratio equals 0.3), i.e. Young's modulus E, the yield stress S_y and the plastic modulus H_p. In the following, simulation of a two-rod test with a bi-linear model is investigated in more detail.

At start of a two-rod test simulation, the back-stress for both of the rods is zero. When the primary load and ¼ of the first secondary load cycle is applied, the back-stress of the most pulled rod (here designated rod 1) increases if it is assumed that the stress in rod 1 exceeds S_y. The back stress of the least pulled rod (here designated rod 2) remains zero as the response of rod 2 is elastic. Now, as the secondary load goes from ¼ to ¾ of its first cycle, the response of rod 1 is elastic while plastic deformation occurs in rod 2. Thus, the back-stress increases in rod 2 while it is constant in rod 1. As the secondary load cycle goes from ¾ to 1¼, plastic deformation in rod 1 starts at a stress of $\sigma_y + \alpha_{rod1\ at\ 1/4}$ (back-stress in rod 1 at ¼ secondary load cycle). When plastic deformation starts in rod 1, the stress in rod 2 has been reduced compared to that one cycle before. The response of rod 2 is elastic. As secondary load cycling continues, plastic deformation is accumulated in both rods (i.e. structural ratcheting). Also the back-stress increases in both rods. Ratchet strain will decrease with the number of cycles as the elastic part of the response will increase with the number of cycles.

Two alternatives are now possible:

1. Secondary stress range $\Delta\sigma_{sec}$ is less or equal to 2 S_y
   Secondary load cycling will eventually result in merely an elastic response in both rods. At this point structural ratcheting stops. From now on, elastic shakedown occurs in both rods as the secondary

cycling continues.

2. Secondary stress range $\Delta\sigma_{sec}$ is larger than 2 S_y
   Secondary load cycling will eventually come to a point when the least pulled rod deforms plastically in compression when approaching the turning point. When this happens, the most pulled rod cannot use the least pulled rod as dolly and structural ratcheting stops. From now on, plastic shakedown occurs in both rods as the secondary cycling continues.

Ideal plastic material model

The ideal plastic material model is a special case of the bi-linear model where the plastic modulus H_p has been reduced to a very small value. As plastic hardening is very low, secondary cycling will result in large plastic strains in the most pulled rod. A consequence of this is that structural ratcheting at constant ratchet strain will occur.

Multi-linear material model (Besseling)

As the multi-linear material model is a linear kinematic hardening model it will principally behave as the bi-linear model described above, i.e. it cannot capture material ratcheting.

Armstrong-Frederick material model

The Armstrong-Frederick material model is a nonlinear kinematic hardening model equivalent with the Chaboche model with one back-stress. Four material constants define the model (assuming Poisson's ratio equals 0.3), i.e. Young's modulus E, yield stress S_y and two plastic hardening constants c_{AF} and γ_{AF}. With this material model, material ratcheting can be simulated in contrary to what is possible with the linear kinematic hardening models. Another important feature of the Armstrong-Frederick model is the bounding stress. The bounding stress is determined as

$$\sigma_{bound} = S_y + c_{AF}/\gamma_{AF} \qquad \text{(Eq. 5-3)}$$

If stress in a simulation approaches σ_{bound}, the amount of plastic strain becomes large. The bounding stress can be compared with the yield stress in an ideal plastic model.

A number of simulation conditions are now possible:

1. $\sigma_{prim} + 0.5\ \Delta\sigma_{sec} < \sigma_{bound}$ and $\Delta\sigma_{sec} \leq 2\ S_y$

These conditions will eventually result in elastic shakedown. The back-stress in the two rods will increase until the response is elastic in the whole structure.

2. $\sigma_{prim} + 0.5\ \Delta\sigma_{sec} < \sigma_{bound}$ and $\Delta\sigma_{sec} > 2\ S_y$

   These conditions will eventually result in a combination of structural and material ratcheting. Plastic deformation will occur in compression.

3. $\sigma_{prim} + 0.5\ \Delta\sigma_{sec} \geq \sigma_{bound}$ and $\Delta\sigma_{sec} \leq 2\ S_y$

   These conditions will eventually result in structural ratcheting. Plastic deformation will not occur in compression.

4. $\sigma_{prim} + 0.5\ \Delta\sigma_{sec} \geq \sigma_{bound}$ and $\Delta\sigma_{sec} > 2\ S_y$

   These conditions will eventually result in structural ratcheting. As plastic deformation is large in the most pulled rod, higher compression stresses cannot be built up. Plastic deformation will not occur in compression.

Chaboche material model

The Chaboche material model is a non-linear kinematic hardening model, here with three back-stress tensors. Eight material constants define the model (assuming Poisson's ratio equals 0.3), i.e. Young's modulus E, yield stress S_y and six constants $c_1, c_2, c_3, \gamma_1, \gamma_2$ and γ_3 describing the plastic hardening. With this material model, material ratcheting can be simulated. As for the Armstrong-Frederick model, one important feature is the bounding stress. The bounding stress is determined as

$$\sigma_{bound} = S_y + c_1/\gamma_1 + c_2/\gamma_2 + c_3/\gamma_3 \qquad \text{(Eq. 5-4)}$$

If stress in a simulation approaches σ_{bound}, the amount of plastic strain becomes large. The bounding stress can be compared with the yield stress in an ideal plastic model. The same simulation conditions as for the Armstrong-Frederick model are now possible, see above.

5.6.1. Determination of constants in material models

Determination of constants in the different constitutive models used for simulation of the two-rod tests is discussed in this section. Additional information about how these constants were determined is given in [17] and [18].

Bi-linear kinematic hardening models

Constants in the bi-linear kinematic hardening models are given for P265 and 316L in Table 5-9. Figure 5-25 and 5-26 show a comparison between the simulated response and test results from tensile and fully-reversed strain controlled cycling tests. As expected, the yield interval cannot be captured for the P265 material in the simulation of the tensile test. Furthermore, the bi-linear models have problems to capture the cyclic test response. For the 316L material, which shows a pronounced cyclic hardening, this problem is obvious.

Table 5-9 Constants in bi-linear models.

	Young's modulus E	Yield stress S_y	Plastic modulus H_p
P265	213 GPa	298 MPa	1938 MPa
316L	197 GPa	315 MPa	2000 MPa

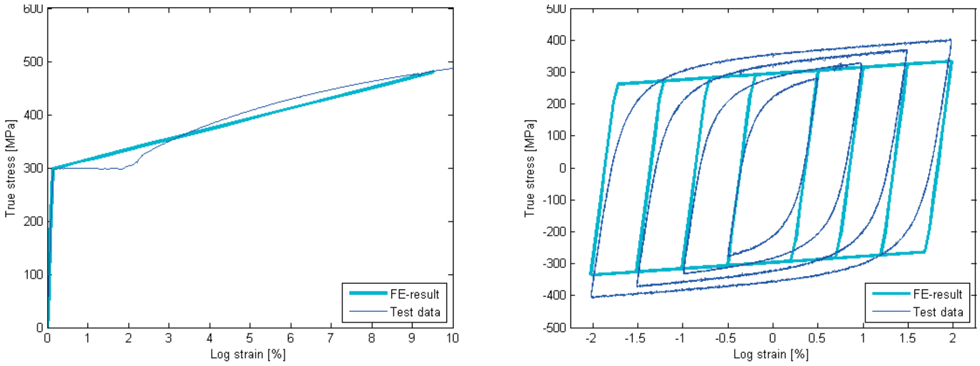

Figure 5-25 **Simulated response with the bi-linear model compared to test results from tensile and fully-reversed strain cycling tests for P265. Only saturated stress-strain loops are shown.**

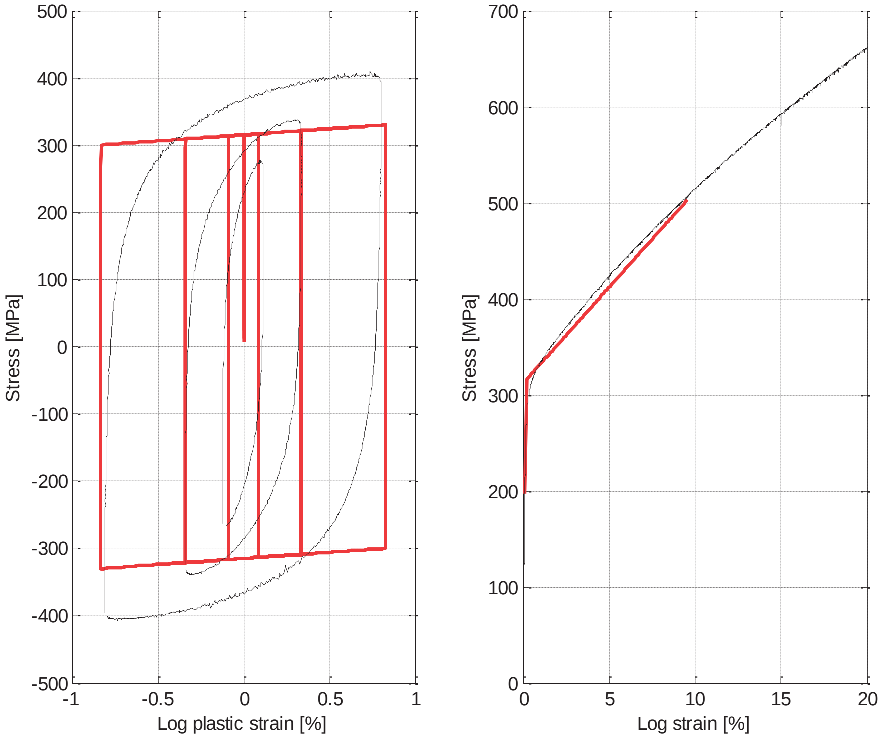

Figure 5-26 **Simulated response with the bi-linear model compared to test results from tensile and fully-reversed strain cycling tests for 316L. Only saturated stress-plastic strain loops are shown. Red colour corresponds to model results and black colour corresponds to test results.**

Ideal plastic model

The ideal plastic model is a special case of the bi-linear model where the plastic modulus is reduced to a very low value, see Table 5-10. The possibility to predict the response of the tensile and the fully-reversed strain cycling tests is very limited with this model as seen in Figure 5-27. Only P265 has been investigated with an ideal plastic model.

Table 5-10 **Constants in ideal plastic models.**

	Young's modulus E	Yield stress $\boldsymbol{S_y}$	Plastic modulus $\boldsymbol{H_p}$
P265	213 GPa	298 MPa	11 MPa

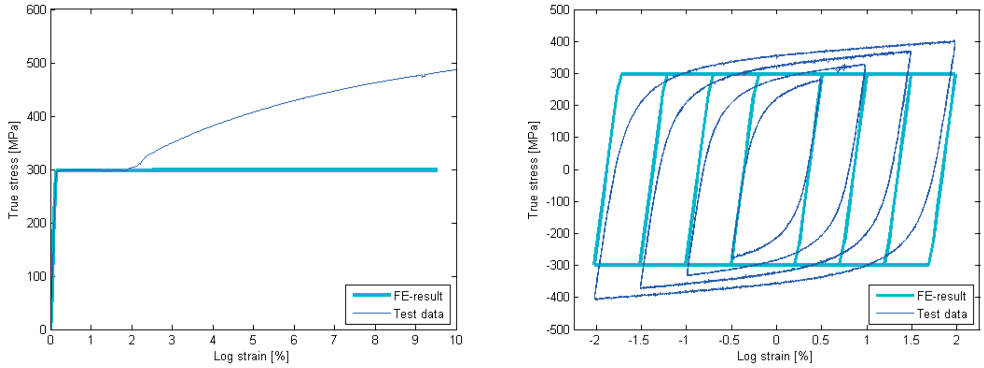

Figure 5-27 **Simulated response with the ideal plastic model compared to test results from tensile and fully-reversed strain cycling tests for P265. Only saturated stress-strain loops are shown.**

Multi-linear kinematic hardening models

Points at the stress-strain curve defining the multi-linear kinematic hardening models are given for P265 and 316L in Table 5-11 and 5-12, respectively. As expected and shown in Figure 5-28 and 5-29, the tensile tests are perfectly simulated. The yield interval is here considered for P265 which results in an almost ideal plastic response in the simulation of the fully-reversed strain cycling test (max strain amplitude of 2%). Cycling tests of the 316L material reveal a pronounced cyclic hardening. It is obvious that this phenomenon cannot be captured with the multi-linear model, see Figure 5-29.

Table 5-11 **P265 - Points on stress-strain curve defining the multi-linear model.**

Point	1	2	3	4	5	6	7	8	9	10
Stress [MPa]	295	298	330	367	407	448	476	523	558	600
Strain [%]	0.14	2.0	2.5	3.5	5.0	7.0	9.0	14	20	30

Table 5-12 316L - Points on stress-strain curve defining the multi-linear model.

Point	1	2	3	4	5	6	7	8	9	10
Stress [MPa]	50	101	151	200	251	275	300	325	350	375
Strain [%]	0.023	0.052	0.083	0.12	0.17	0.21	0.33	0.76	1.6	2.7

Point	11	12	13	14	15	16	17
Stress [MPa]	400	500	600	700	800	900	980
Strain [%]	3.9	9.2	15.7	23.0	31.1	39.9	48.0

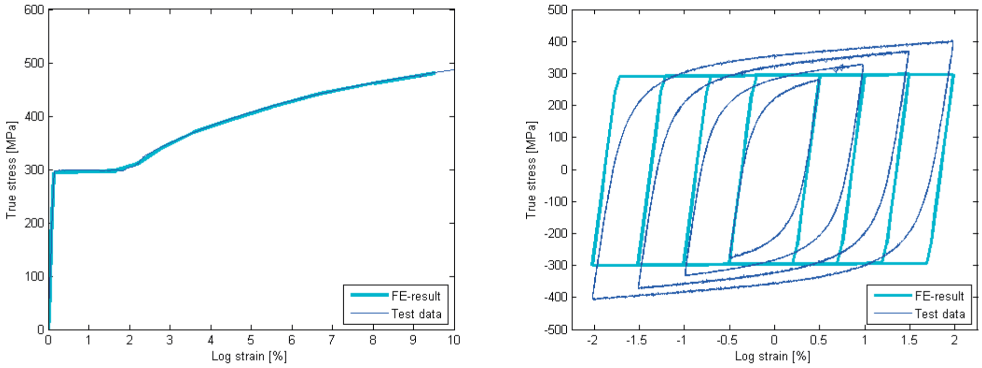

Figure 5-28 Simulated response with the multi-linear model compared to test results from tensile and fully-reversed strain cycling tests for P265. Only saturated stress-strain loops are shown.

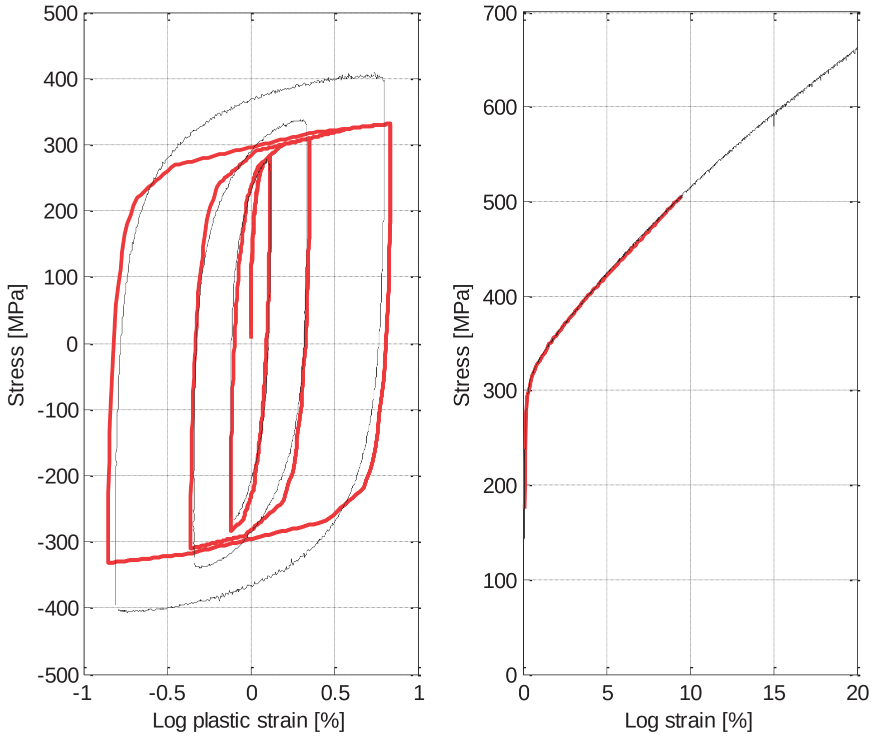

Figure 5-29 **Simulated response with the multi-linear model compared to test results from tensile and fully-reversed strain cycling tests for 316L. Only saturated stress-plastic strain loops are shown. Red colour corresponds to model results and black colour corresponds to test results.**

Armstrong-Frederick nonlinear kinematic hardening models

Constants in the Armstrong-Frederick nonlinear kinematic hardening models are given for P265 and 316L in Table 5-13. The saturated stress-plastic strain loops from the fully-reversed strain cycling tests are used for determination of the constants. As seen from tensile test simulation results in Figure 5-30 and 5-31, the stress has an upper bound of about 400 MPa for both P265 and 316L. This is a consequence of the description of the back-stress evolution and the plastic hardening in the Armstrong-Frederick constitutive model. The 316L model is better than the P265 model to capture the fully-reversed strain cycling tests.

Table 5-13 **Constants in Armstrong-Frederick models.**

	E_{sat}	S_y	c_{AF}	γ_{AF}
P265	192 GPa	224 MPa	1.81e10	100
316L	197 GPa	240 MPa	4.5e10	280

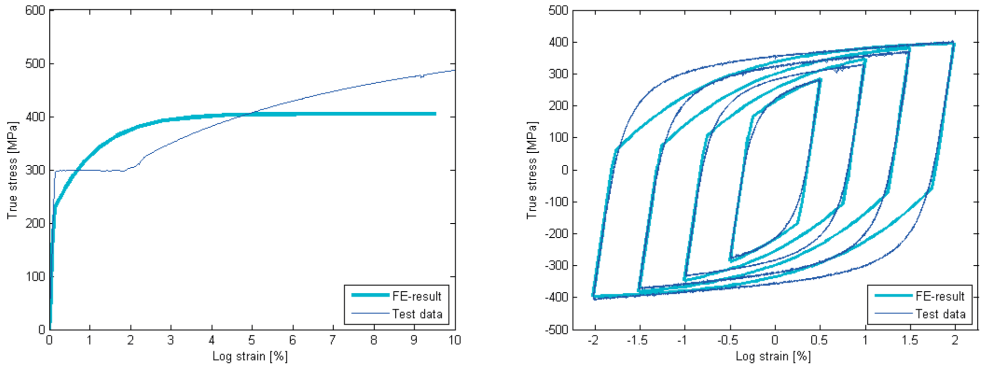

Figure 5-30 **Simulated response with the Armstrong-Frederick model compared to test results from tensile and fully-reversed strain cycling tests for P265. Only saturated stress-strain loops are shown.**

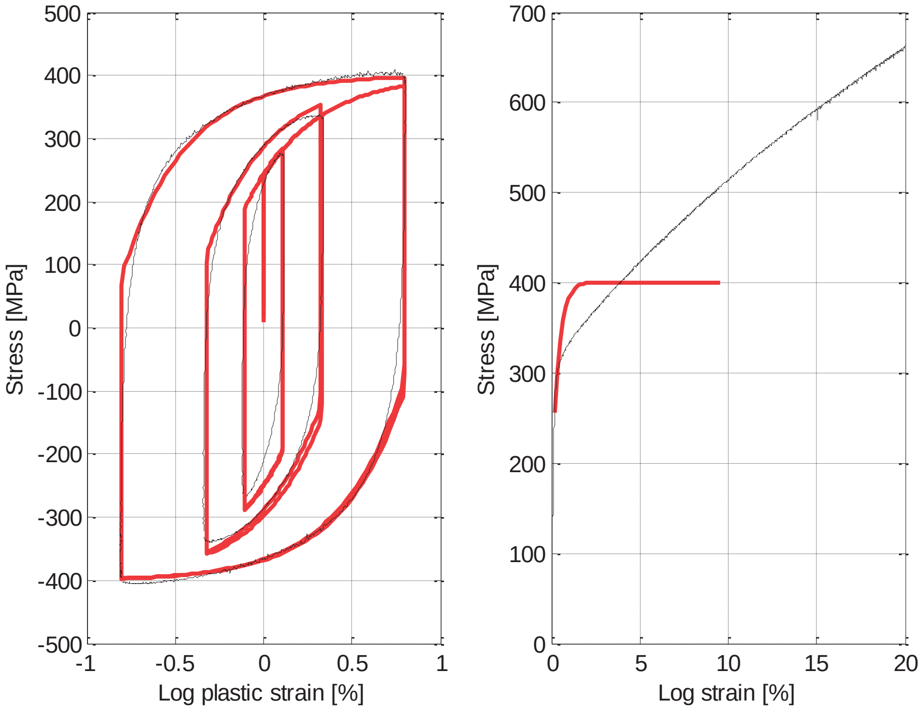

Figure 5-31 **Simulated response with the Armstrong-Frederick model compared to test results from tensile and fully-reversed strain cycling tests for 316L. Only saturated stress-plastic strain loops are shown. Red colour corresponds to model results and black colour corresponds to test results.**

Chaboche nonlinear kinematic hardening models

Constants in the Chaboche nonlinear kinematic hardening models are given for P265 in Table 5-14 to 5-16 and for 316L in Table 5-17. The saturated stress-plastic strain loops from the fully-reversed strain cycling tests are used for determination of the constants. Three back-stress tensors are used for all Chaboche models. In the first P265 model designated C3, constants are determined based on all four saturated stress-plastic strain loops in Figure 5-14. In the second P265 model designated C3V, in addition isotropic hardening is considered why two more constants are added. The constants in the third P265 model designated C3:2 are determined based only on the saturated stress-plastic strain loop from fully-reversed strain cycling test with amplitude 2%. Figure 5-32 to 5-35 show that the possibility to predict the experimental results, particularly the cyclic tests, increases with the Chaboche model. Introducing isotropic hardening (model C3V) even further improves the model if the material shows cyclic hardening characteristics, see Figure 5-33.

Table 5-14 P265 - Constants in Chaboche model C3.

E_{sat}	$\sigma_{y,C3}$	c_1	γ_1	c_2	γ_2	c_3	γ_3
192 GPa	100 MPa	2.49e9	13.2	2.85e10	352	2.24e11	1537

Table 5-15 P265 - Constants in Chaboche model C3V.

E_{sat}	$\sigma_{y,V}$	c_1	γ_1	c_2	γ_2	c_3	γ_3
192 GPa	6.17 MPa	2.79e9	13.2	3.79e10	368	5.99e11	3751

R_0	R_∞	b
0	80 MPa	20

Table 5-16 P265 - Constants in Chaboche model C3:2.

E_{sat}	$\sigma_{y,C3}$	c_1	γ_1	c_2	γ_2	c_3	γ_3
192 GPa	86 MPa	2.79e9	13.2	3.79e10	368	5.99e11	3751

Table 5-17 316L - Constants in Chaboche model.

E_{sat}	$\sigma_{y,C3}$	c_1	γ_1	c_2	γ_2	c_3	γ_3
197 GPa	145 MPa	1.85e10	160	8.0e10	800	1.85e11	3500

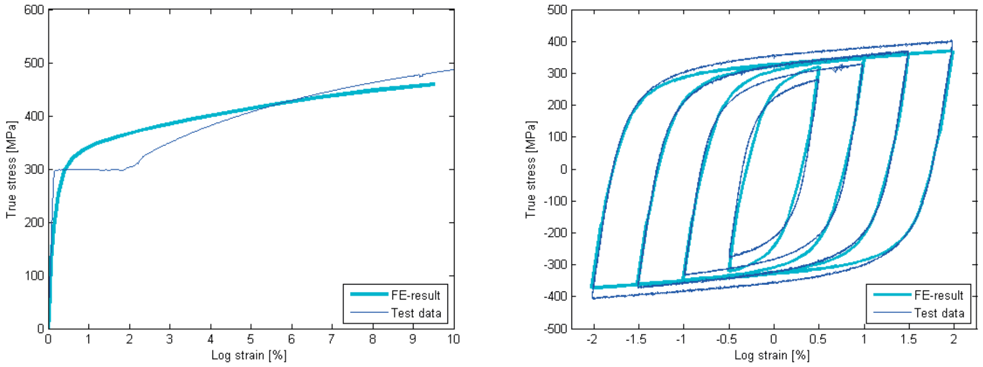

Figure 5-32 Simulated response with the Chaboche model (C3) compared to test results from tensile and fully-reversed strain cycling tests for P265. Only saturated stress-strain loops are shown.

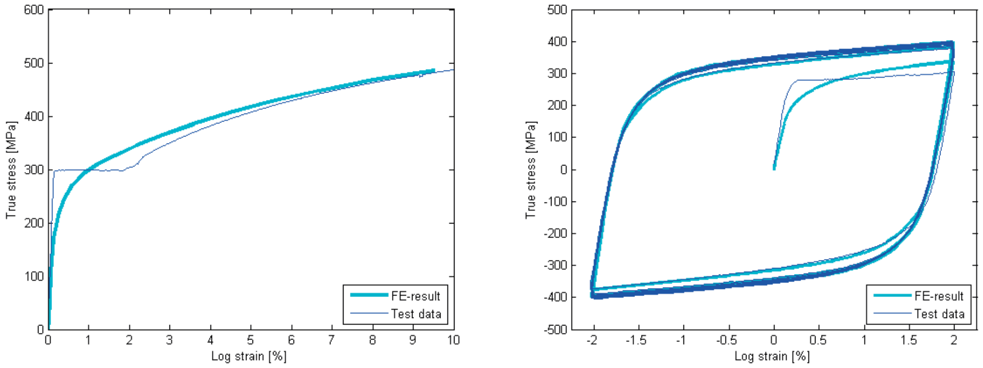

Figure 5-33 Simulated response with the Chaboche model C3V compared to test results from tensile and fully-reversed strain cycling tests for P265. Only the fully-reversed strain cycling test with 2% strain amplitude is shown.

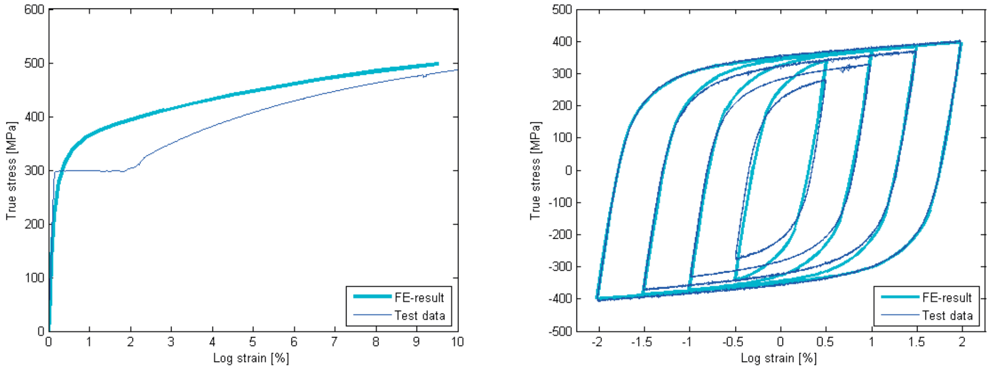

Figure 5-34 Simulated response with the Chaboche model C3:2 compared to test results from tensile and fully-reversed strain cycling tests for P265. Only saturated stress-strain loops are shown.

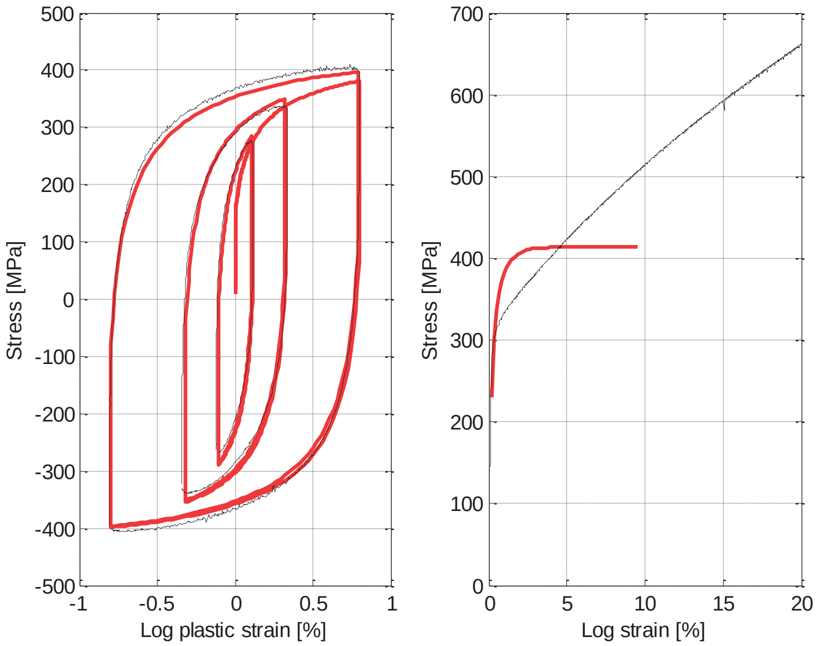

Figure 5-35 **Simulated response with the Chaboche model compared to test results from tensile and fully-reversed strain cycling tests for 316L. Only saturated stress-plastic strain loops are shown. Red colour corresponds to model results and black colour corresponds to test results.**

5.6.2. Results from numerical simulation of two-rod tests

This section shows results from numerical simulation of the two-rod tests with the different constitutive models. Results are given for each model with all load combinations presented in the same figure. Mean strain of the two specimens as a function of cycles is shown for both experiments and simulations. Load combination is given above each sub-figure. The 5% strain criterion in ASME NB-3228.4 is included in the figures for comparison. Additional results can be found in [17] and [18].

P265 - Bi-linear kinematic hardening model

Figure 5-39 shows results from simulation of the two-rod tests with the bi-linear kinematic hardening model. For a secondary stress range $\Delta\sigma_{sec} \leq 2\,S_y = 3\,S_m$, the bi-linear model is expected to eventually predict elastic shakedown. Numerical results indicate that this is the case. For $\Delta\sigma_{sec} > 2\,S_y = 3\,S_m$, the bi-linear model is expected to predict plastic shakedown. In the sub-figures with a secondary stress range of $6\,S_m$ and $9\,S_m$, it is seen that simulated mean strain suddenly stops to increase. At this point, plastic deformation starts in the most compressed rod and the most pulled rod cannot use the most compressed one as a dolly anymore. Plastic shakedown has occurred. Up to a strain level of 5%, the bi-linear model predicts the mean strain in the two-rod tests very well.

P265 - Ideal plastic model

Figure 5-40 shows results from simulation of the two-rod tests with the ideal plastic model. As expected and as seen in the sub-figures, ratcheting occurs for all cases with a constant ratchet strain. The initial strain development in the simulations corresponds rather well with test results during the first ten cycles. Up to a strain level of 5%, the ideal plastic model predicts the mean strain in the two-rod tests rather well. The model predicts equal or more strain than the experiments show.

P265 - Multi-linear kinematic hardening model

Figure 5-41 shows results from simulation of the two-rod tests with the multi-linear model. As for the bi-linear model, it is expected to eventually predict elastic shakedown for a secondary stress range $\Delta\sigma_{sec} \leq 2\ S_y = 3\ S_m$. Numerical results indicate that this is the case. For $\Delta\sigma_{sec} > 2\ S_y = 3\ S_m$, simulation results show a saw-tooth shape. The explanation for this artefact is related to the yield interval that is considered for P265 when describing the stress-strain curve. The way the multi-linear model works, the yield interval considered here is present both in tension and compression. After simulation of a certain number of cycles, plastic deformation starts in the most compressed rod. At this point the numerical model becomes instable as the modulus in the yield interval is very low, now influencing both the pulled and the compressed rod. During experimental cycling of P265, however, the yield interval vanishes. Figure 5-36 shows a modified stress-strain curve after a few numbers of cycles. Numerical simulation of one of the P265 two-rod tests with the modified stress-strain curve is shown in Figure 5-37. Now, the numerical response is as expected. A comparison with corresponding sub-figure in Figure 5-41 ($\sigma_{prim} = S_m$, $\Delta\sigma_{sec} = 6\ S_m$) shows that the two simulations agree very well up to plastic shakedown takes place. The effect of cyclic loading on the yield interval part of the stress-strain curve is further discussed in section 6.5.1. Up to a strain level of 5%, the multi-linear model predicts the mean strain in the two-rod tests very well as seen in Figure 5-41.

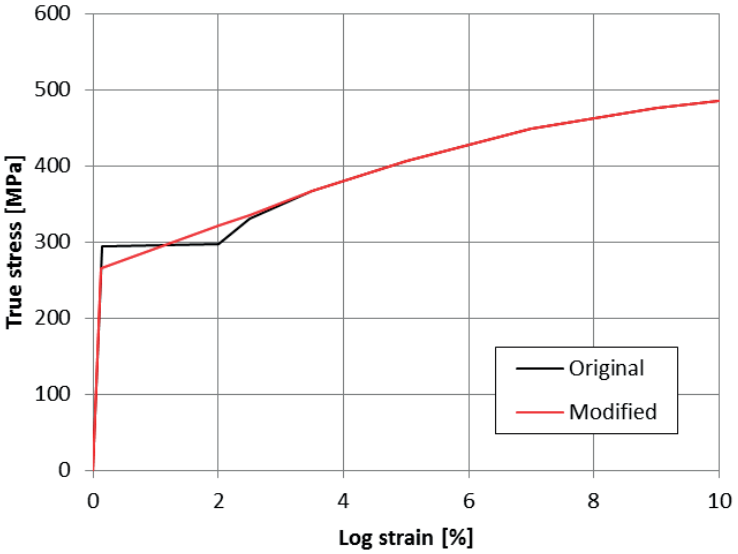

Figure 5-36 **Modified description of multi-linear model for P265. Original description is given in Table 5-11.**

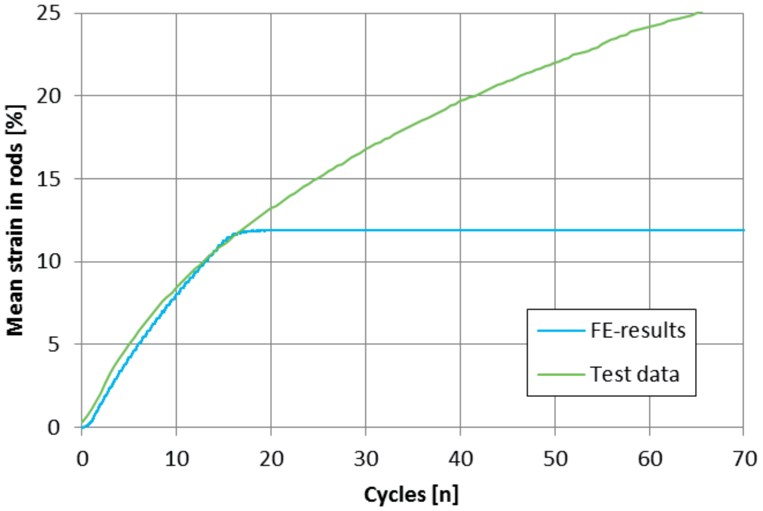

Figure 5-37 **Numerical simulation of P265 two-rod test with modified description of multi-linear model according to Figure 5-36. Load combination: $\sigma_{prim} = S_m$ and $\Delta\sigma_{sec} = 6\ S_m$.**

P265 - Armstrong-Frederick model

Figure 5-42 shows results from simulation of the two-rod tests with the Armstrong-Frederick model. Simulated elastic shakedown is expected to eventually occur if the following two conditions are fulfilled: $\sigma_{prim} + 0.5\ \Delta\sigma_{sec} < \sigma_{bound} = S_y + c_{AF}/\gamma_{AF} = 405$ MPa and $\Delta\sigma_{sec} \leq 2\ S_y = 448$ MPa. None of the load combinations fulfils these conditions. A combination of simulated material and structural ratcheting is expected to eventually occur if the following conditions are fulfilled: $\sigma_{prim} + 0.5\ \Delta\sigma_{sec} <$

$\sigma_{bound} = 405$ MPa and $\Delta\sigma_{sec} > 2\ S_y = 448$ MPa. These conditions are fulfilled for the load combination $\sigma_{prim} = 0.5\ S_m$ / $\Delta\sigma_{sec} = 3\ S_m$. A stress-plastic strain graph from simulation indicates that a combination of material and structural ratcheting occurs, see Figure 5-38. For the remaining load combinations in Figure 5-42, structural ratcheting is expected to eventually occur. The sub-figures indicate that this is the case. Up to a strain level of 5%, the Armstrong-Frederick model predicts less mean strain compared to that of the two-rod tests.

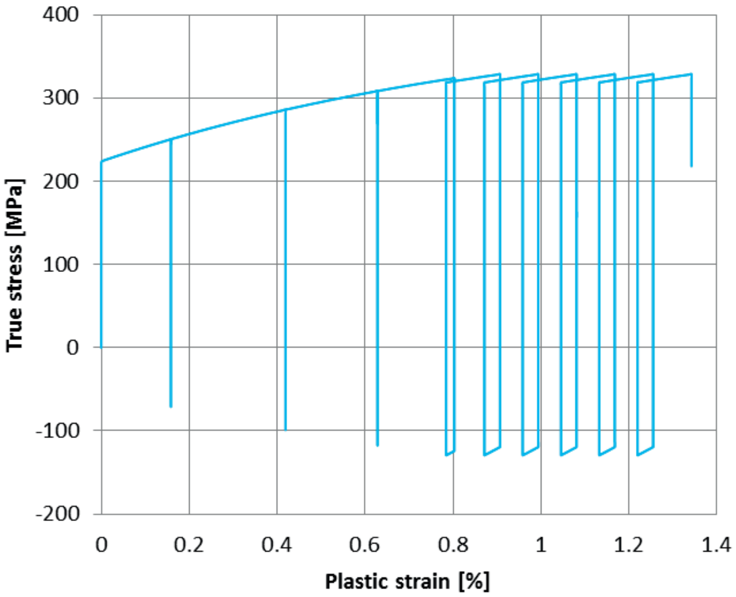

Figure 5-38 **Stress versus plastic strain for one of the two-rod specimens. The Armstrong-Frederick model is used in the simulation with $\sigma_{prim} = 0.5\ S_m$ and $\Delta\sigma_{sec} = 3\ S_m$.**

P265 - Chaboche model C3

Figure 5-43 shows results from simulation of the two-rod tests with the Chaboche model designated C3. Simulated elastic shakedown is expected to eventually occur if the following two conditions are fulfilled: $\sigma_{prim} + 0.5\ \Delta\sigma_{sec} < \sigma_{bound} = S_y + c_1/\gamma_1 + c_2/\gamma_2 + c_3/\gamma_3 = 515$ MPa and $\Delta\sigma_{sec} \leq 2\ S_y = 200$ MPa. None of the load combinations fulfils these conditions. A combination of simulated material and structural ratcheting is expected to eventually occur if the following conditions are fulfilled: $\sigma_{prim} + 0.5\ \Delta\sigma_{sec} < \sigma_{bound} = 515$ MPa and $\Delta\sigma_{sec} > 2\ S_y = 200$ MPa. These both conditions are fulfilled for the three load combinations $\sigma_{prim} = 1.25\ S_m$ / $\Delta\sigma_{sec} = 2\ S_m$, $\sigma_{prim} = 0.5\ S_m$ / $\Delta\sigma_{sec} = 3\ S_m$ and $\sigma_{prim} = S_m$ / $\Delta\sigma_{sec} = 3\ S_m$. A stress-plastic strain graph from simulation would show that a combination of material and structural ratcheting occurs. For the remaining load combinations in Figure 5-43, structural ratcheting is expected to eventually occur. The sub-figures indicate that this is the case. Up to a strain level of 5%, the Chaboche model C3 predicts less mean strain compared to that of the two-rod tests.

P265 - Chaboche model C3V

Figure 5-44 shows results from simulation of the two-rod tests with the Chaboche model designated C3V. Simulated elastic shakedown is expected to eventually occur if the following two conditions are fulfilled: $\sigma_{prim} + 0.5\ \Delta\sigma_{sec} < \sigma_{bound} = S_y + c_1/\gamma_1 + c_2/\gamma_2 + c_3/\gamma_3 = 560$ MPa and $\Delta\sigma_{sec} \leq 2\ S_y = 2 \cdot (6.17 + 80) = 172$ MPa. None of the load combinations fulfils these conditions. A combination of simulated material and structural ratcheting is expected to eventually occur if the following conditions are fulfilled: $\sigma_{prim} + 0.5\ \Delta\sigma_{sec} < \sigma_{bound} = 560$ MPa and $\Delta\sigma_{sec} > 2\ S_y = 172$ MPa. These both conditions are fulfilled for the four load combinations $\sigma_{prim} = 1.25\ S_m$ / $\Delta\sigma_{sec} = 2\ S_m$, $\sigma_{prim} = 0.5\ S_m$ / $\Delta\sigma_{sec} = 3\ S_m$, $\sigma_{prim} = S_m$ / $\Delta\sigma_{sec} = 3\ S_m$ and $\sigma_{prim} = 1.25\ S_m$ / $\Delta\sigma_{sec} = 3\ S_m$. A stress-plastic strain graph from simulation would show that a combination of material and structural ratcheting occurs. For the remaining load combinations in Figure 5-44, structural ratcheting is expected to eventually occur. The sub-figures indicate that this is the case. Up to a strain level of 5%, the Chaboche model C3V predicts less mean strain compared to that of the two-rod tests. The Chaboche model C3V is slightly better than the Chaboche model C3 to predict the mean strain developed.

P265 - Chaboche model C3:2

Figure 5-45 shows results from simulation of the two-rod tests with the Chaboche model designated C3:2. As the material constants for the Chaboche model C3:2 are the same as for the Chaboche model C3V (after the isotropic hardening has taken place) these two models show the same phenomenological response.

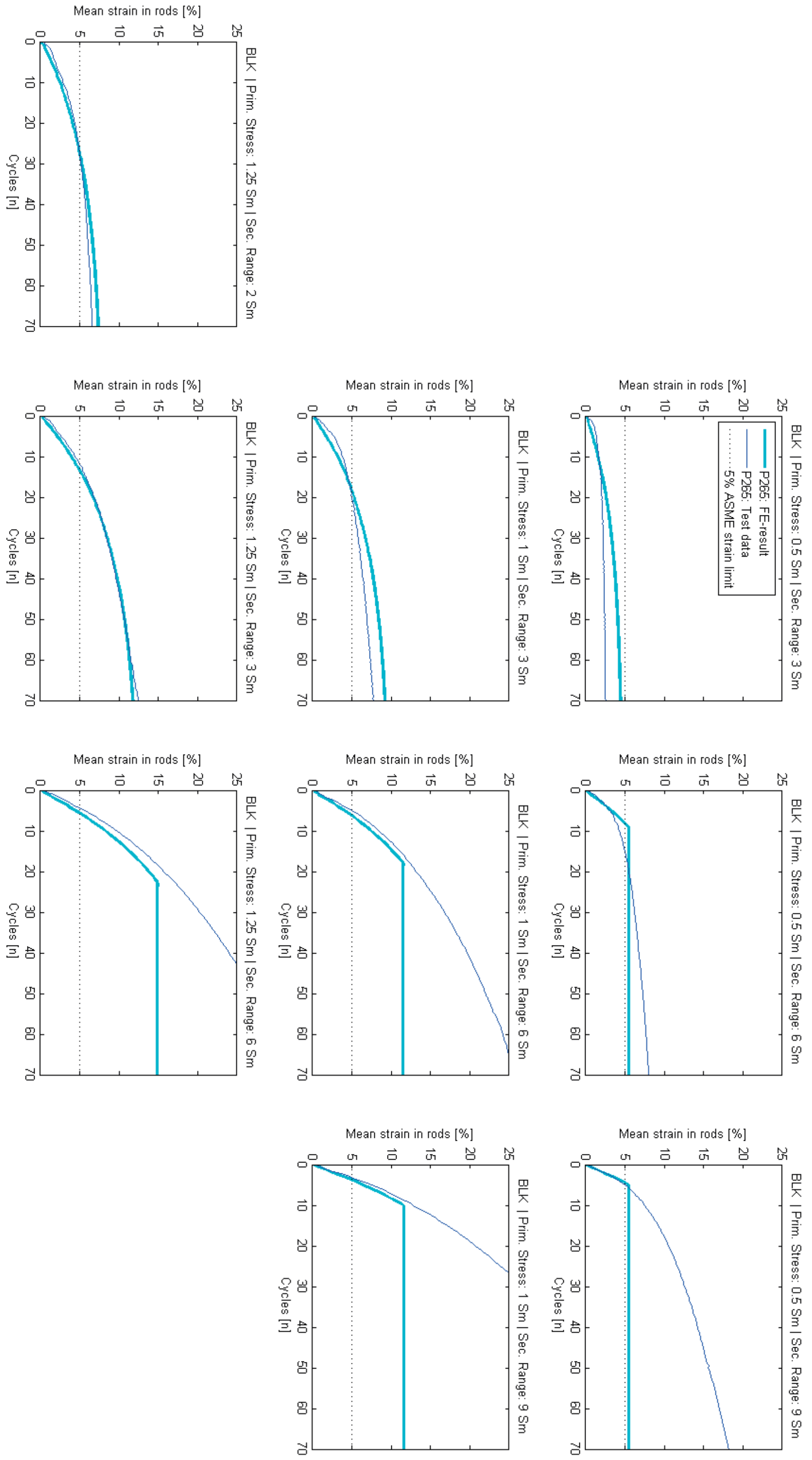

Figure 5-39 **Numerical simulation of P265 two-rod tests with the bi-linear kinematic hardening model.**

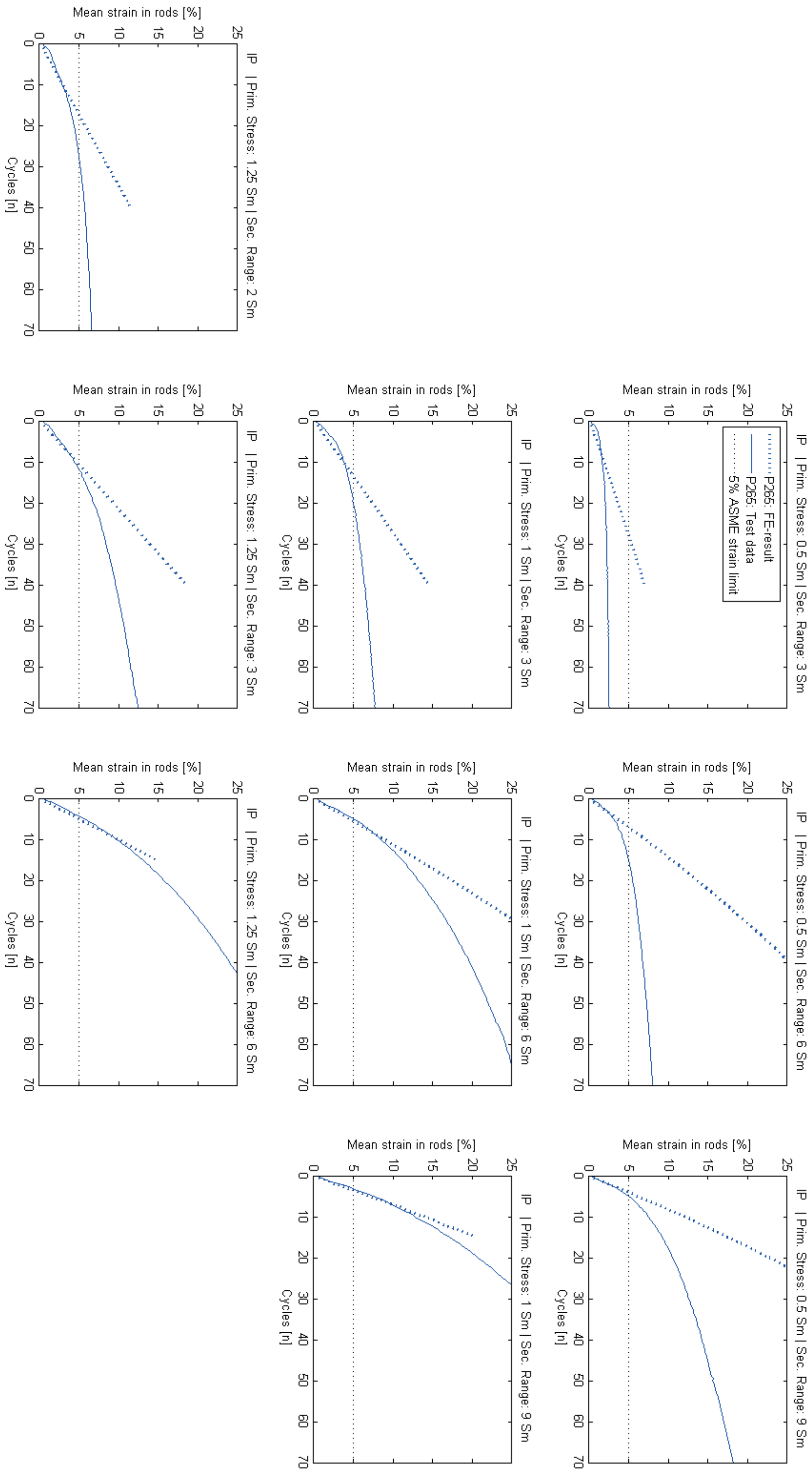

Figure 5-40 Numerical simulation of P265 two-rod tests with the ideal plastic model.

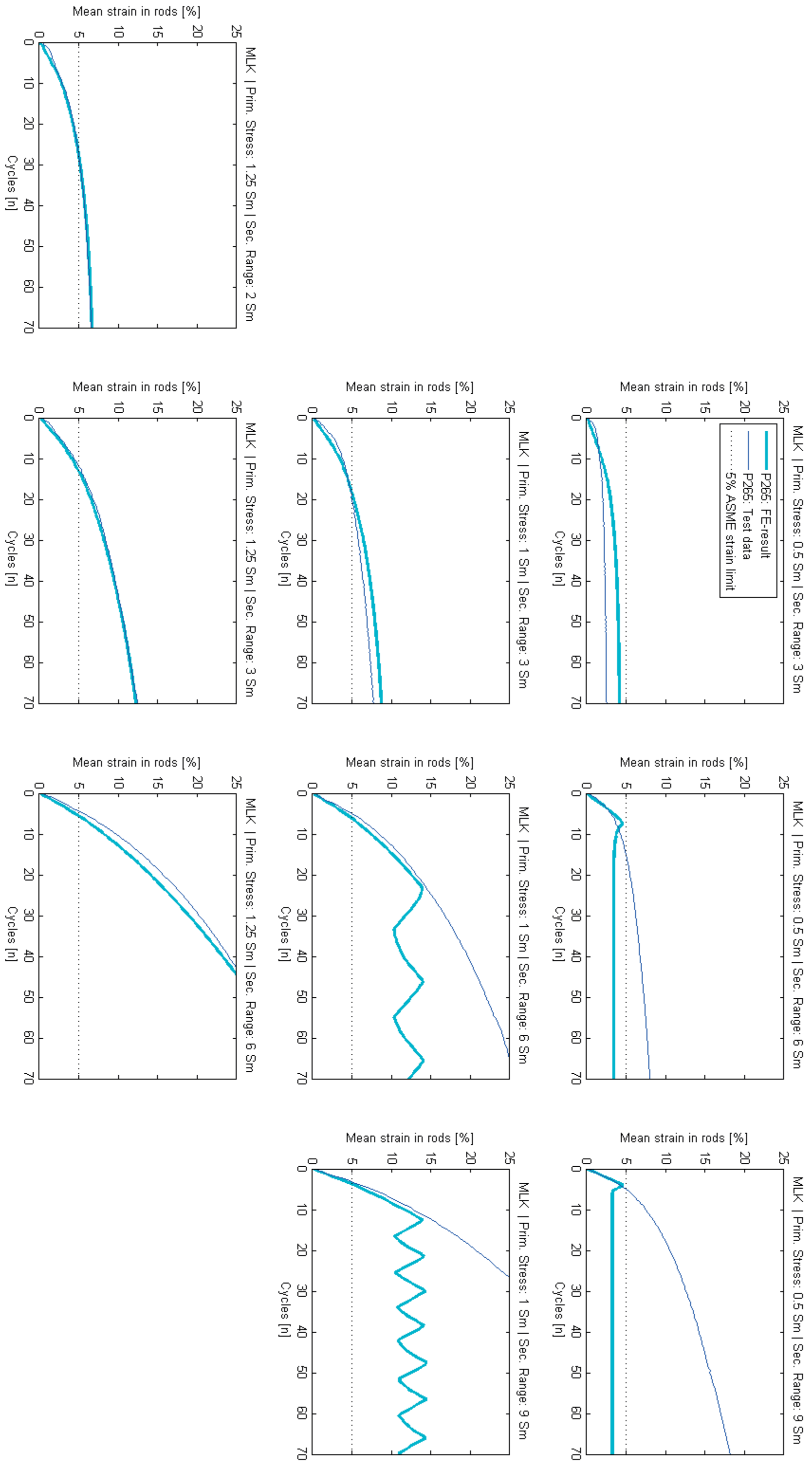

Figure 5-41 Numerical simulation of P265 two-rod tests with the multi-linear kinematic hardening model.

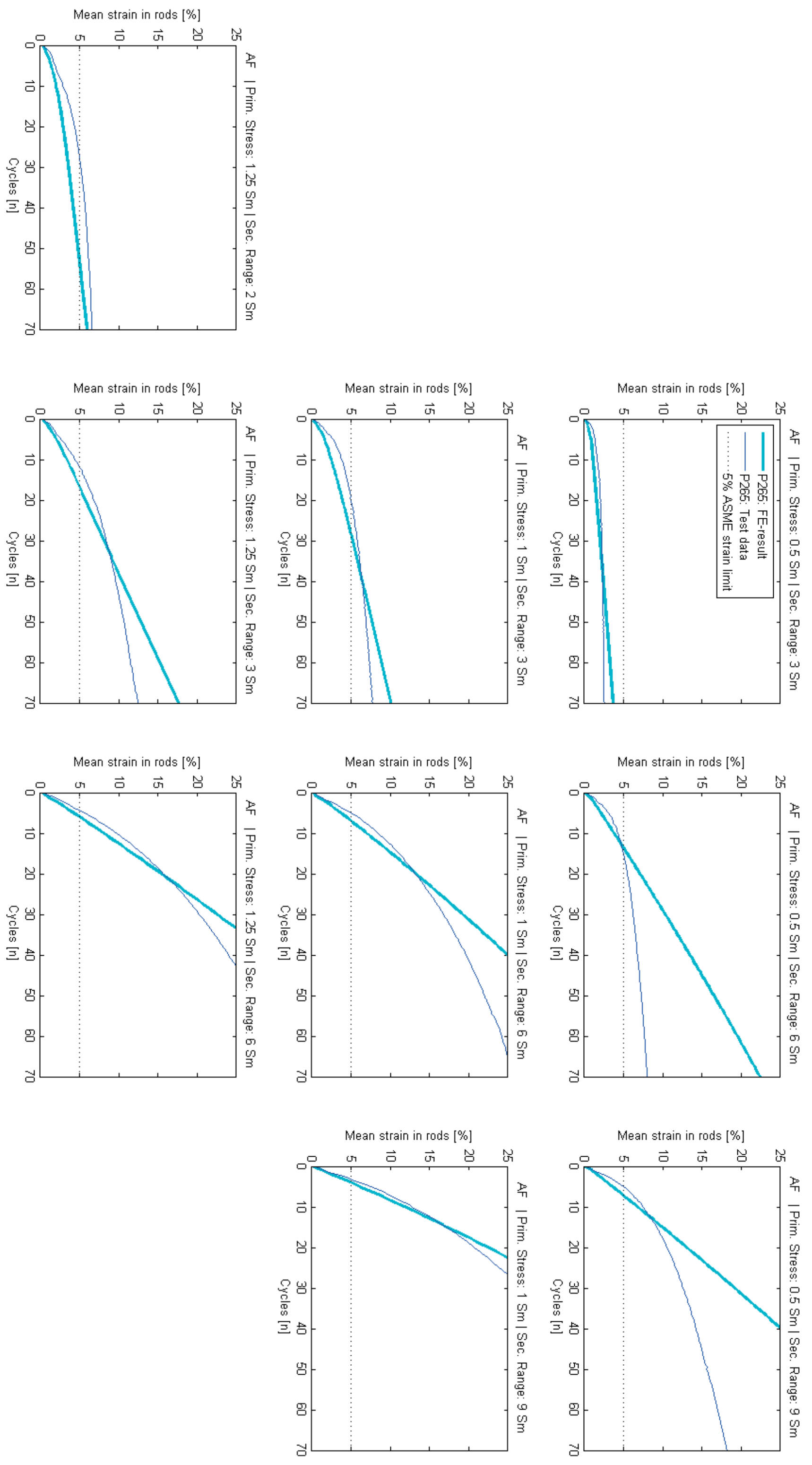

Figure 5-42 Numerical simulation of P265 two-rod tests with the Armstrong-Frederick model.

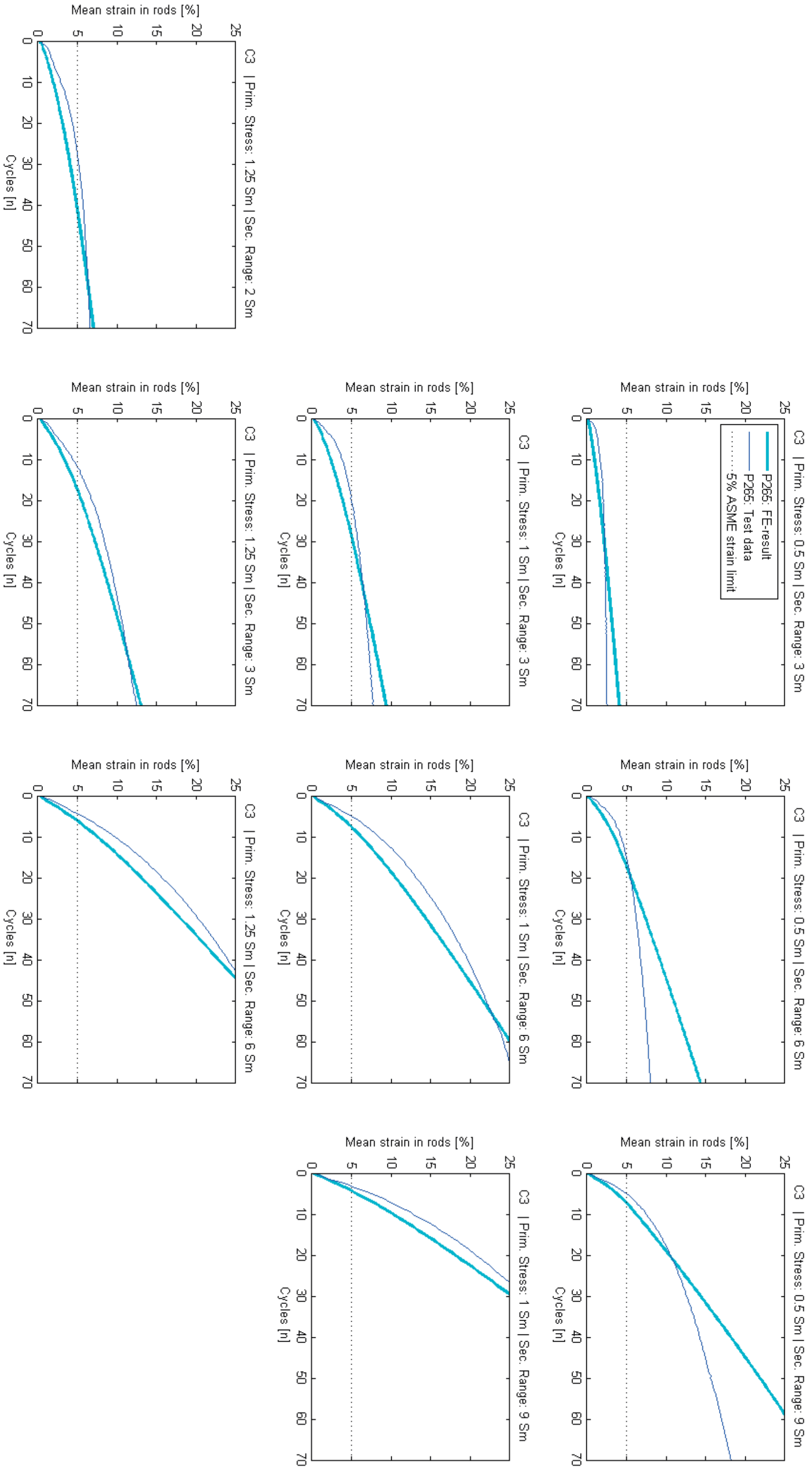

Figure 5-43 Numerical simulation of P265 two-rod tests with the Chaboche model C3.

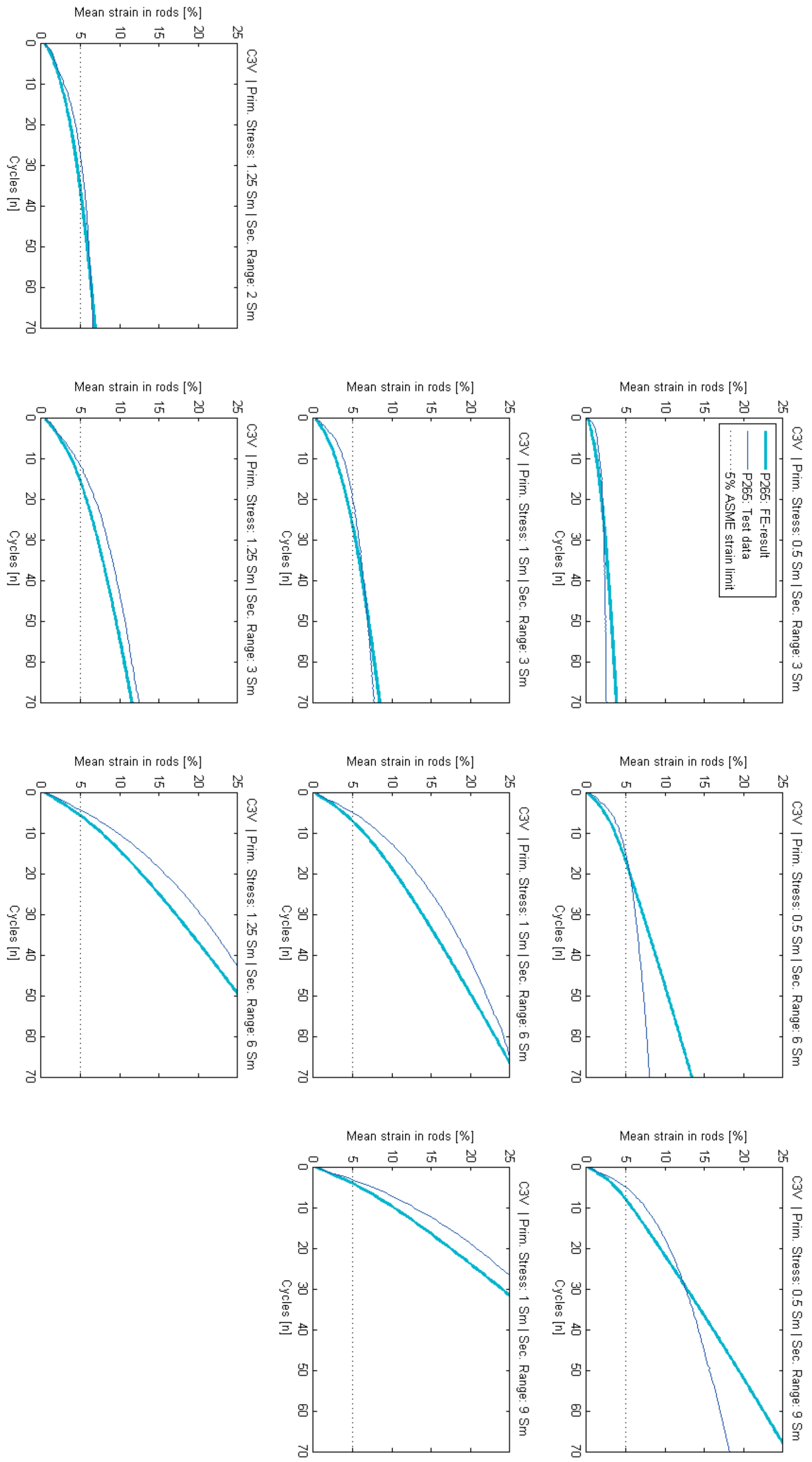

Figure 5-44 **Numerical simulation of P265 two-rod tests with the Chaboche model C3V which includes isotropic hardening.**

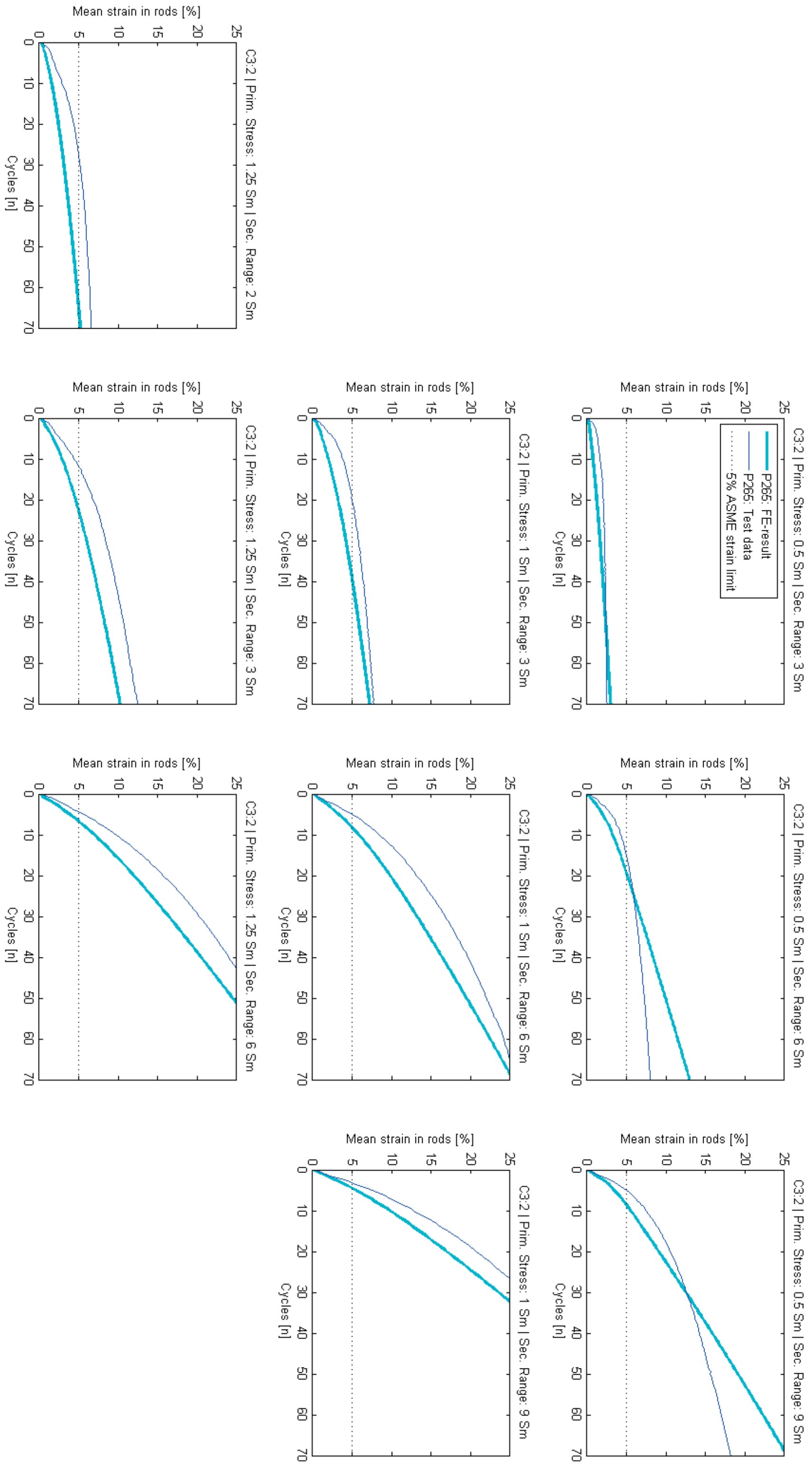

Figure 5-45 **Numerical simulation of P265 two-rod tests with the Chaboche model C3:2.**

316L - Bi-linear kinematic hardening model

Figure 5-46 shows results from simulation of the two-rod tests with the bi-linear kinematic hardening model. For a secondary stress range $\Delta\sigma_{sec} \leq 2\ S_y = 3\ S_m$, the bi-linear model is expected to eventually predict elastic shakedown. Numerical results indicate that this is the case. For $\Delta\sigma_{sec} > 2\ S_y = 3\ S_m$, the bi-linear model is expected to predict plastic shakedown. In the sub-figures with a secondary stress range of 6 S_m and 9 S_m, it is seen that simulated mean strain suddenly stops to increase. At this point, plastic deformation starts in the most compressed rod and the most pulled rod cannot use the most compressed rod as a dolly anymore. Plastic shakedown has occurred. Up to a strain level of 5%, the bi-linear model predicts the mean strain in the two-rod tests rather well.

316L - Multi-linear kinematic hardening model

Figure 5-47 shows results from simulation of the two-rod tests with the multi-linear model. This model has no distinct yield stress. Similarities with the bi-linear model can be seen with elastic shakedown indicated for load combinations with $\Delta\sigma_{sec} \leq 3\ S_m$ and plastic shakedown indicated for $\Delta\sigma_{sec} \geq 4.5\ S_m$. The transition from structural ratcheting to plastic shakedown is however not as distinct as for the bi-linear model, compare Figure 5-46 and 5-47. Up to a strain level of 5%, the multi-linear model predicts less or equal amount of mean strain compared to that of the two-rod tests.

316L - Armstrong-Frederick model

Figure 5-48 shows results from simulation of the two-rod tests with the Armstrong-Frederick model. Simulated elastic shakedown is expected to eventually occur if the following two conditions are fulfilled: $\sigma_{prim} + 0.5\ \Delta\sigma_{sec} < \sigma_{bound} = S_y + c_{AF}/\gamma_{AF} = 401$ MPa and $\Delta\sigma_{sec} \leq 2\ S_y = 480$ MPa. These conditions are fulfilled for the two load combinations $\sigma_{prim} = 1.25\ S_m$ / $\Delta\sigma_{sec} = S_m$ and $\sigma_{prim} = S_m$ / $\Delta\sigma_{sec} = 2\ S_m$. This response is shown in corresponding sub-figures in Figure 5-48. A combination of simulated material and structural ratcheting is expected to eventually occur if the following conditions are fulfilled: $\sigma_{prim} + 0.5\ \Delta\sigma_{sec} < \sigma_{bound} = 401$ MPa and $\Delta\sigma_{sec} > 2\ S_y = 480$ MPa. These conditions are fulfilled for the load combination $\sigma_{prim} = 0.5\ S_m$ / $\Delta\sigma_{sec} = 3\ S_m$. A stress-plastic strain graph from simulation would show that a combination of material and structural ratcheting occurs. For the remaining load combinations in Figure 5-48, structural ratcheting is expected to eventually occur. This response is indicated in the sub-figures. Up to a strain level of 5%, the Armstrong-Frederick model predicts less mean strain compared to that of the two-rod tests when $\sigma_{prim} \geq S_m$ and $\Delta\sigma_{sec} \leq 3\ S_m$. For load combinations with $\sigma_{prim} = 0.5\ S_m$ and $\Delta\sigma_{sec} \leq 6\ S_m$ the opposite prevails.

316L - Chaboche model

Figure 5-49 shows results from simulation of the two-rod tests with the Chaboche model. Simulated elastic shakedown is expected to eventually occur if the following two conditions are fulfilled: $\sigma_{prim} + 0.5\ \Delta\sigma_{sec} < \sigma_{bound} = S_y + c_1/\gamma_1 + c_2/\gamma_2 + c_3/\gamma_3 = 413$ MPa and $\Delta\sigma_{sec} \leq 2\ S_y = 290$ MPa. These conditions are fulfilled for the load combination $\sigma_{prim} = 1.25\ S_m$ / $\Delta\sigma_{sec} = S_m$. The sub-figure shows expected response. A combination of simulated material and structural ratcheting is expected to eventually occur if the following conditions are fulfilled: $\sigma_{prim} + 0.5\ \Delta\sigma_{sec} < \sigma_{bound} = 413$ MPa and $\Delta\sigma_{sec} > 2\ S_y = 290$ MPa. These both conditions are fulfilled for the two load combinations $\sigma_{prim} = S_m$ / $\Delta\sigma_{sec} = 2\ S_m$ and $\sigma_{prim} = 0.5\ S_m$ / $\Delta\sigma_{sec} = 3\ S_m$. A stress-plastic strain graph from simulation would show that a combination of material and structural ratcheting occurs. For the remaining load combinations in Figure 5-49, structural ratcheting is expected to eventually occur. This response is indicated in corresponding sub-figures. Up to a strain level of 5%, the response of the Chaboche model is similar to that of the Armstrong-Frederick model except for the load combination $\sigma_{prim} = S_m$ / $\Delta\sigma_{sec} = 2\ S_m$.

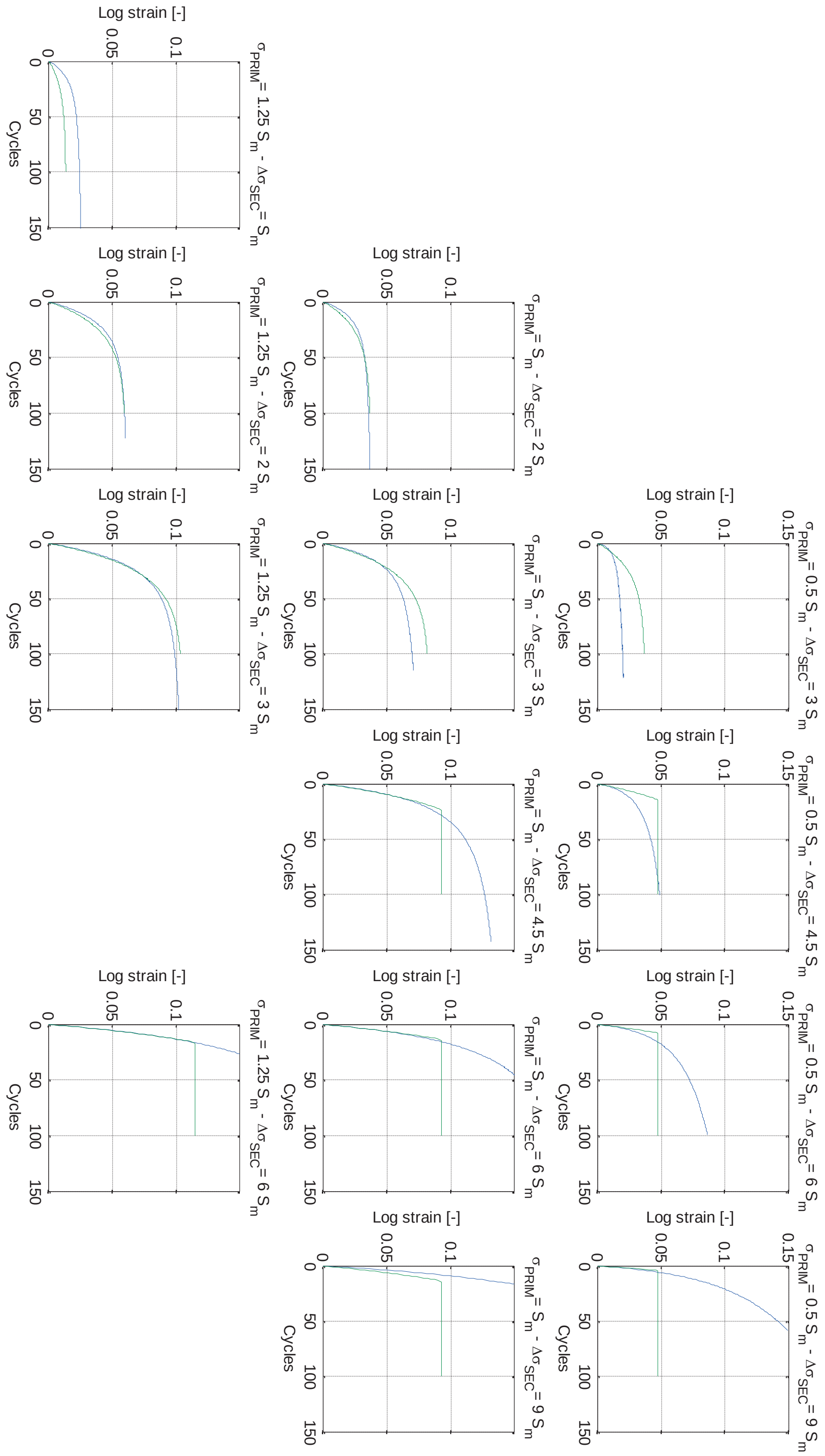

Figure 5-46 Numerical simulation of 316L two-rod tests with the bi-linear kinematic hardening model. Blue curves represent experiments and green curves represent simulations.

]

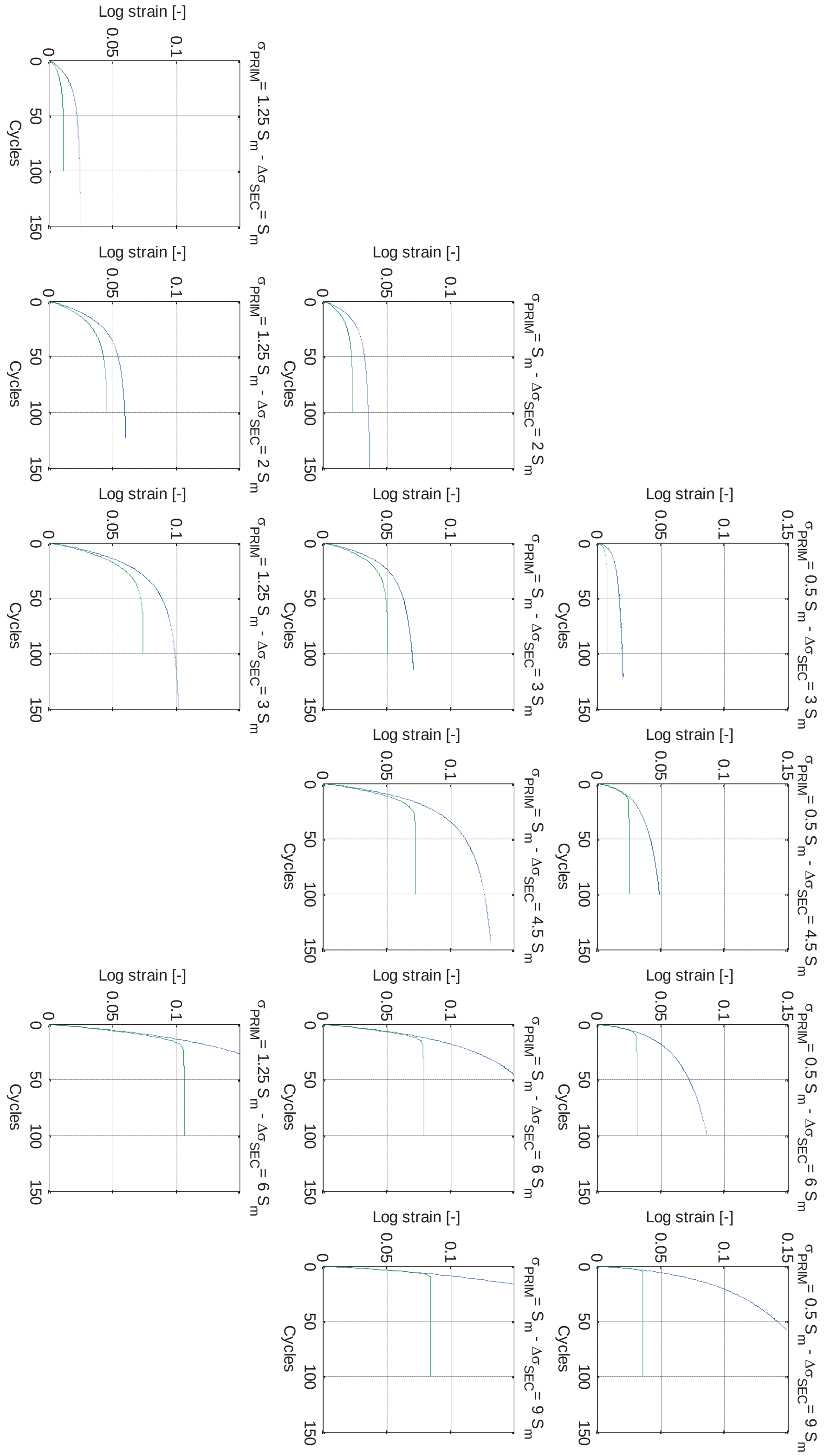

Figure 5-47 **Numerical simulation of 316L two-rod tests with the multi-linear kinematic hardening model. Blue curves represent experiments and green curves represent simulations.**

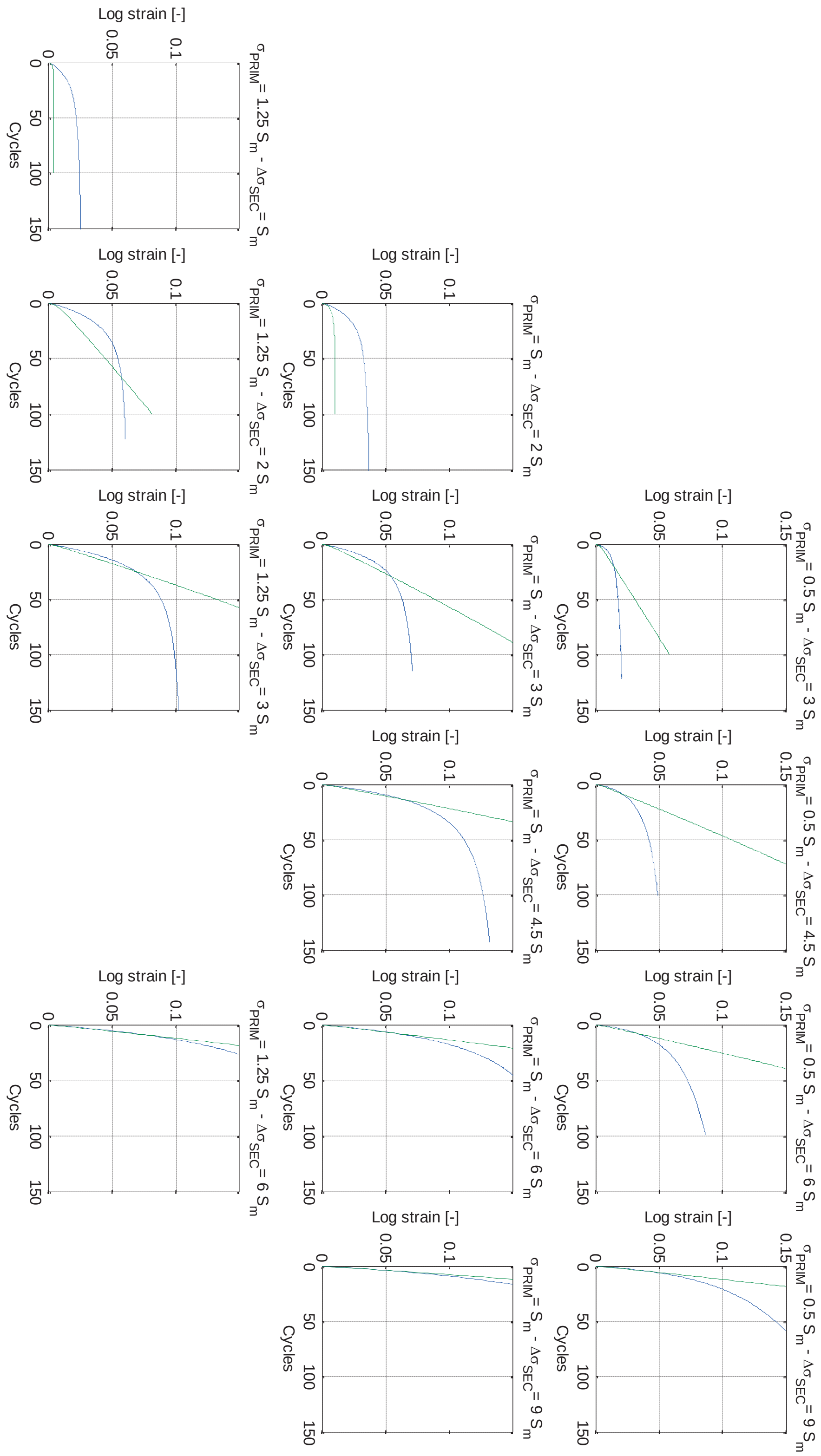

Figure 5-48 **Numerical simulation of 316L two-rod tests with the Armstrong-Frederick model. Blue curves represent experiments and green curves represent simulations.**

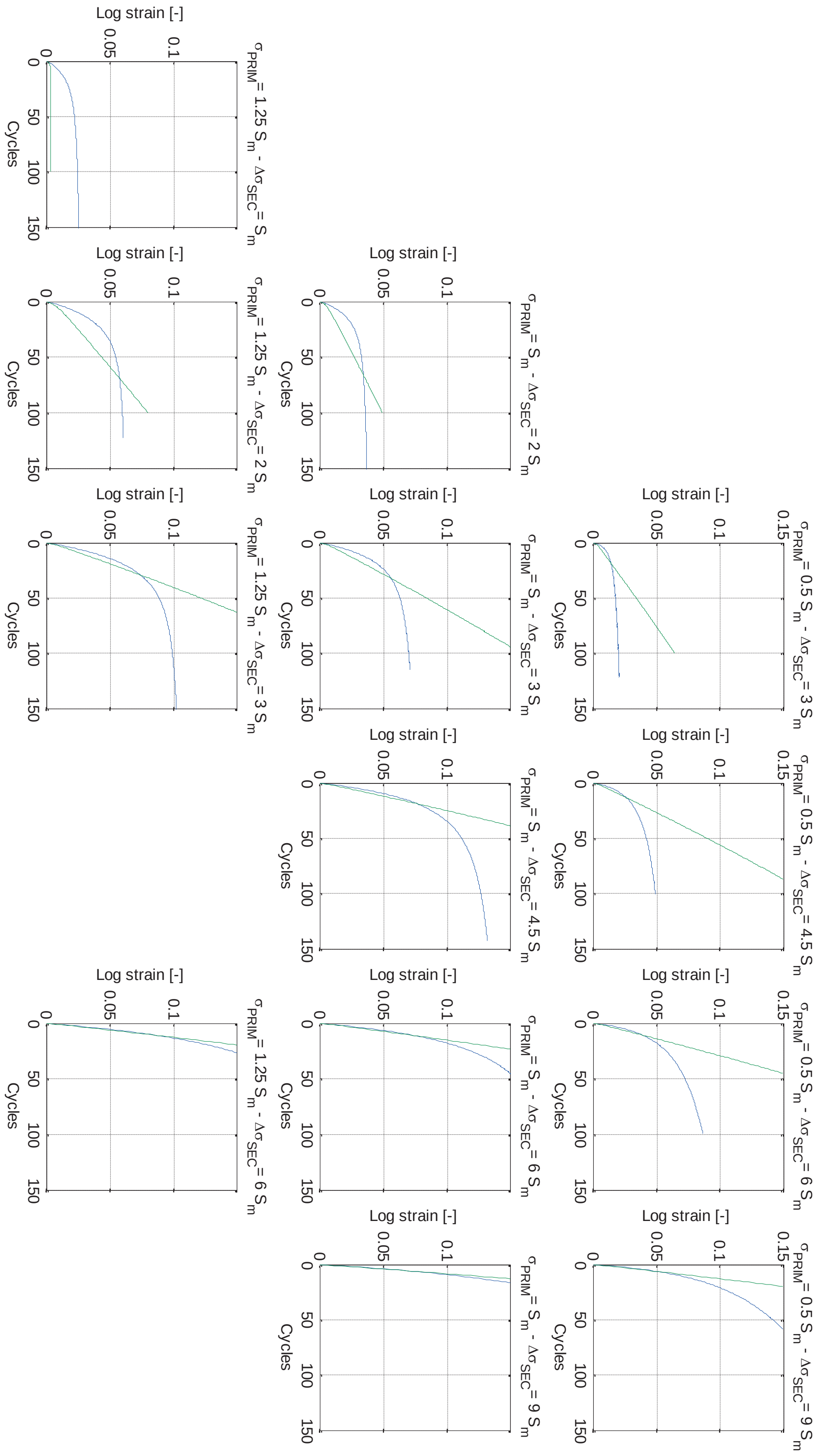

Figure 5-49 **Numerical simulation of 316L two-rod tests with the Chaboche model. Blue curves represent experiments and green curves represent simulations.**

5.6.3. Evaluation of numerical simulation of two-rod tests

Two-rod tests of the two materials P265 and 316L are simulated with four different constitutive models. The models investigated can be divided in two main groups; linear and nonlinear kinematic hardening models. The linear models are characterised by their simplicity in the sense that only results from a tensile test is needed to determine the constants in the models. However, these models cannot capture material ratcheting. In contrary to the linear models, the nonlinear models can capture material ratcheting. In general, nonlinear models are better in simulating cyclic response. Determination of the constants in these models is however not as easy as for the linear models and furthermore is additional cyclic test data needed.

Generally, the results from the bi-linear model and the multi-linear model look similar for the respective material. This is also the case for the two nonlinear models, i.e. the Armstrong-Frederick (one back-stress tensor) and Chaboche (three back-stress tensors).

The linear models show initial structural ratcheting followed by shakedown after a sufficient number of cycles. Type of shakedown is dependent on the relation between the secondary stress range $\Delta\sigma_{sec}$ and the yield stress S_y of the model. Elastic shakedown occurs if $\Delta\sigma_{sec} \leq 2\ S_y$ while plastic shakedown occurs if $\Delta\sigma_{sec} > 2\ S_y$.

The nonlinear models show initial structural ratcheting followed by either elastic shakedown, continued structural ratcheting or a combination of structural and material ratcheting. The load combination, the yield stress S_y of the model and the bounding stress $\sigma_{bound} = S_y + \sum c_i/\gamma_i$ of the model determine the eventual response. Elastic shakedown occurs if $\sigma_{prim} + 0.5\ \Delta\sigma_{sec} < \sigma_{bound}$ and $\Delta\sigma_{sec} \leq 2\ S_y$, structural ratcheting occurs if $\sigma_{prim} + 0.5\ \Delta\sigma_{sec} > \sigma_{bound}$, and a combination of structural and material ratcheting occurs if $\sigma_{prim} + 0.5\ \Delta\sigma_{sec} < \sigma_{bound}$ and $\Delta\sigma_{sec} > 2\ S_y$.

The strain level 5% is of special interest as this is the limit for how much accumulated strain caused by ratcheting that can be accepted in a structure according to the ASME NB-3228.4 [6].

Up to a strain level of 5%, simulations of the P265 two-rod tests show that the linear models predict the response better than the nonlinear models do. Simulation result for the linear models is very good while the nonlinear models underestimate the strain development. One explanation for this deviation might be that the constants in the nonlinear models are determined based on cyclic test data for which cyclic hardening is taken into account. The specimens in a two-rod test are however primarily subjected to plastic deformation in one direction (tension) why less cyclic hardening takes place during the tests than during a fully-reversed strain cycling test. Determining the constants in the nonlinear models based on the tensile curve, instead of the cyclic test data, would increase simulated strain. However, then the idea of using a more advanced model must be questioned.

Regarding simulation of the 316L two-rod tests, the linear models are not superior compared to the nonlinear models. Up to a strain level of 5%, the multi-linear model underestimates the strain development in almost all two-rod tests. Strain predictions with the bi-linear model are better than that with the multi-linear model. The non-linear models both over- and underestimate the strain development. For load combinations with a primary stress $\sigma_{prim} \geq S_m$, strain is underestimated. As for the P265, constants in the nonlinear models could be determined based on the tensile curve instead of cyclic data. Cyclic hardening is then not considered and simulated strain development would increase. For load combinations with a primary stress of $\sigma_{prim} = 0.5\ S_m$, simulated strain is overestimated.

The characteristics of the ferritic steel P265 and the austenitic steel 316L differ. P265 shows a distinct yield interval which is absent for 316L. Cyclic hardening is somewhat more pronounced for 316L than for P265 and 316L shows a higher ductility than P265 does. The way the constants in the respective model are determined influences the constants and thereby also the two-rod test simulation results. The possibility to adjust these constants without violating the overall material characteristics of interest differs between the two materials. Using the tensile curve as input when determining the constants in the nonlinear models could be one remedy for underestimated amount of strain for load combinations with $\sigma_{prim} \geq s_m$. With such nonlinear models, however, it will is not possible to predict the response of the fully-reversed strain cycling tests very accurately.

The two-rod tests of P265 have also been simulated with an ideal plastic model, see Figure 5-40. With this model the simulated strain development is overestimated for all two-rod tests.

In summary, the best model to use for simulation of two-rod tests depends on the characteristics of the material and the loading conditions. In this investigation of the two materials P265 and 316L, the bi-linear model seems to best predict the strain development up to a strain level of 5%. The multi-linear model works well for P265 but underestimates the strain for 316L. The nonlinear models for both P265 and 316L underestimate the strain for load combinations with $\sigma_{prim} \geq s_m$. Using the tensile curve for determination of the constants in the nonlinear models, instead of the cyclic test data, would increase simulated strain for these load combinations. However, then the idea of using a more advanced model must be questioned.

5.7. Material ratcheting tests

5.7.1. P265

A material ratcheting test is performed with a mean stress of 50 MPa and a stress amplitude of 325 MPa. Specimen geometry is given in Table 5-1. Stress-strain curve from the test is given in Figure 5-50. The increasing stress amplitude reflects the decreasing cross section area with the number of cycles.

Linear models cannot capture material ratcheting per definition. Generally, nonlinear models can capture material ratcheting. The constants determined for the present nonlinear models result in a bounding stress $\sigma_{bound} = 405$, 515, 560 and 560 MPa for the Armstrong-Frederick and the Chaboche models C3, C3V and C3:2, respectively. As maximal stress in the material ratcheting test is lower than the bounding stress, all models can be used for simulation.

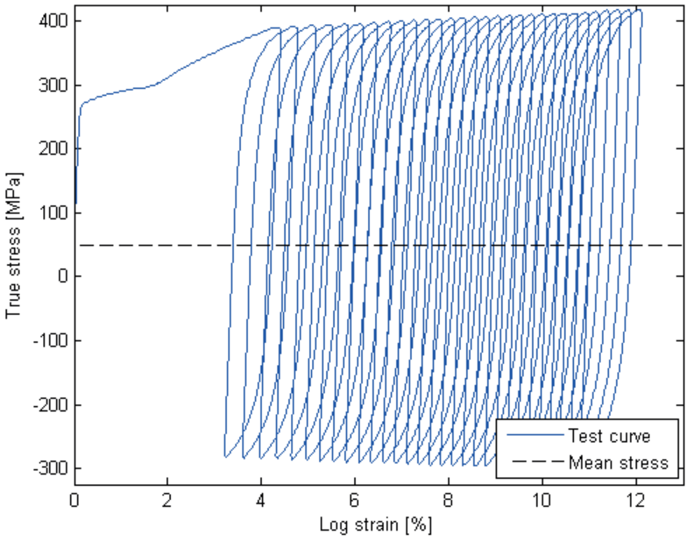

Figure 5-50 Stress-strain response from P265 material ratcheting test.

The Chaboche models C3V and C3:2 best predict test results. The explanation is that these models material constants are determined based on the fully-reversed strain cycling test with a strain amplitude of 2%. Maximal stress in this test is close to maximal stress in the material ratcheting test. Figure 5-51 shows simulation results with the Chaboche model C3:2 where maximal strain during the cycle is shown as function of number of cycles. As the C3:2 model cannot capture the strain development during the initial on-loading of the specimen, the red curve is corrected with respect to strain for an easier comparison with the experiment. As seen in Figure 5-51, the ratchet strain per cycle is very well predicted for the first 15 cycles. Further results from simulation of this ratcheting test are given in [17].

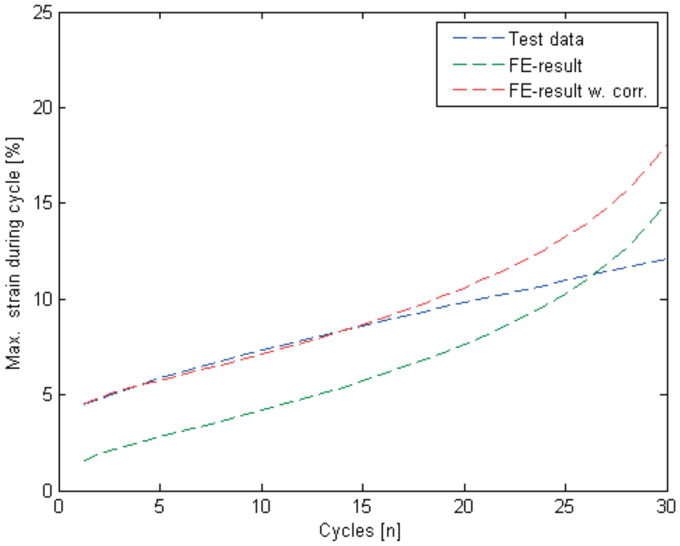

Figure 5-51 Simulation of P265 material ratcheting test with the Chaboche model C3:2.

5.7.2. 316L

A material ratcheting test is performed with a mean stress of $0.5\ S_m = 97.7$ MPa and a stress amplitude of $2\ S_m = 390.6$ MPa. Specimen geometry is given in Table 5-1. Stress-strain curve and strain development as a function of number of cycles are presented in Figure 5-52.

The constants determined for the present nonlinear models result in a bounding stress $\sigma_{bound} = 401$ and 413 MPa for the Armstrong-Frederick and the Chaboche model, respectively. As maximal stress in the ratcheting test is 488 MPa, i.e. $> \sigma_{bound}$, both nonlinear models will respond with an infinite strain when simulating the test. A remedy for this shortcoming would be to determine the constants in the nonlinear models based on a fully-reversed strain cycling test where the resulting maximal stress is larger than 488 MPa.

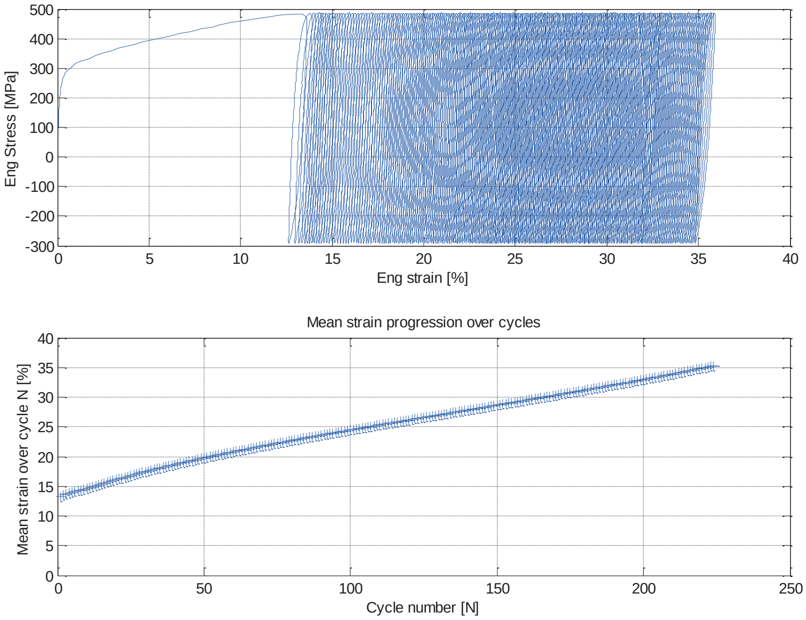

Figure 5-52 316L material ratcheting test results. Upper: Stress versus strain plot. Lower: Strain progression with increasing cycles.

6. Tube testing

6.1. Introduction

During a master thesis work, performed at AREVA NP Uddcomb spring 2013, see [19], the final design of a tube test specimen was developed. The specimen was designed to give a ratcheting response in the multiaxial stress state which may occur in a pressurized pipe which is exposed by cyclic axial deformation controlled loads. This load situation is schematically illustrated in the biaxial stress state in Figure 6-1 whereas Figure 6-2 presents the followed theoretically ratcheting response in the pipe hoop direction and the plastic shake-down response in the pipe axial direction.

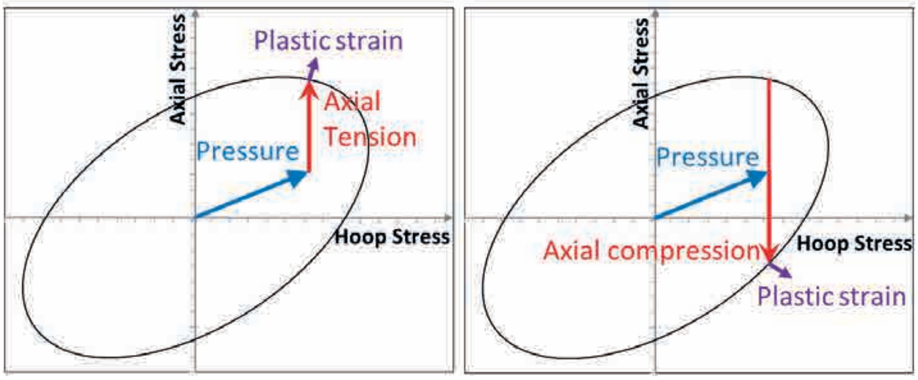

Figure 6-1 **Schematically illustration of the tube stress state in the biaxial stress of state when exposed by internal pressure, axial tension and axial compression.**

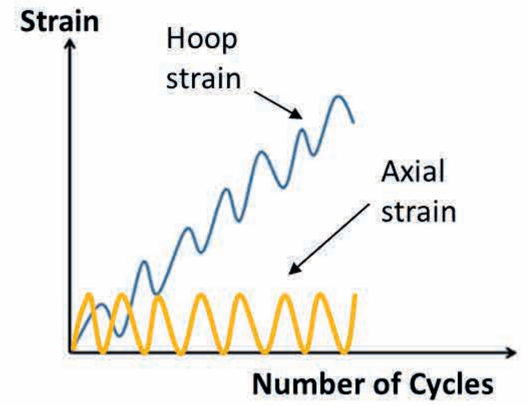

Figure 6-2 **The followed theoretically ratcheting response in the pipe hoop direction and shake-down response in the pipe axial direction.**

During the master thesis work it was successfully verified that a ratcheting response followed when the specimen was subjected by combinations of primary and secondary loads which theoretically would give a ratcheting response. Based on this, in total 30 new test specimens made by two different materials were manufactured, see Figure 6-3.

In March 2014 experiments were conducted on all new specimens at the Complab laboratory at Luleå Technical University. First, in order to determine material properties, monotonic load controlled experiments were performed on several test specimens. Based on the measured material properties, the pressure and axial displacement loads for each of the ratcheting experiments were determined and summarized in a testing scheme. Thereafter, the remaining test specimens were used for ratcheting experiments according to the testing scheme.

It should be noted that the original design concept of the tube specimen in this project was composed by a pressurized pipe which instead of cyclic axial deformation loads would be exposed by cyclic end rotations. However, in the early process of this project, it was obvious that an axial loaded specimen would give a greater number of succeeded experiments since it is, from a practical point of view, much easier to perform that type experiment.

Figure 6-3 Combined photos of the 30 test specimens.

6.2. Experimental specimens

The experimental test specimen consisted of a pipe section and two parts denoted attachments, see illustration in Figure 6-4.

The attachments are made of steel S355 and designed to fit into the tensile test machine. They are much stiffer than the pipe sections and allow connection of hydraulic equipment for introducing pressure into the test specimen. Two types of pipe sections of austenitic steel, 316L, and ferritic steel, P235, with dimensions according to Table 6-1 are investigated. The pipe sections are welded together with the attachments with full penetration butt welds.

In order to easier visualize the size of the specimen a photo of the specimen together with a marker pen is shown in Figure 6-5. Finally, detailed manufactory drawings of the specimens are attached in Appendix 1.

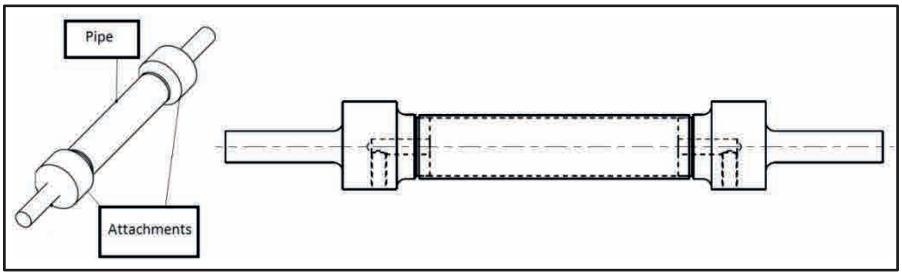

Figure 6-4 Illustration of test specimen.

Table 6-1 Material and dimension for the two pipe sections of investigation.

	D_o	t	L
P235	70.00 mm	2.90 mm	300 mm
316L	73.03 mm	3.05 mm	300 mm

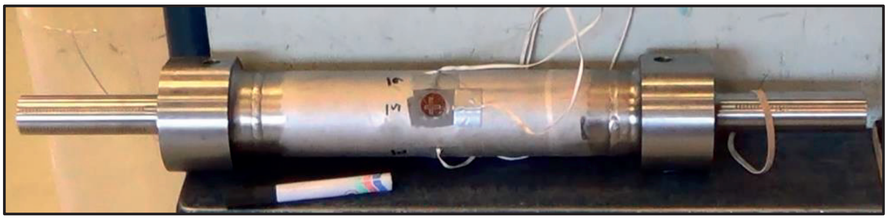

Figure 6-5 Photo of a 316L test specimen and a marker pen.

6.3. Tube test setup

Three types of experimental tests are performed. These are a) monotonic load controlled tensile tests, b) monotonic load controlled internal pressure tests and c) ratcheting tests. During all three types of test the tube specimen is mounted into a tensile test machine. Further, during test type a) and c) the specimen is axially loaded by the tensile test machine and for test type b) and c) the specimen is loaded by internal pressure introduced via an external pressure system.

The monotonic tests are further described in section 6.5 and the ratcheting tests are further described in section 6.6. Below the used pressure regulation system and measurement of strains are described.

6.3.1. Pressure regulation

A constant pressure level is achieved by connecting hydraulic hoses to the threaded holes in both the attachments. One hose is connected to an open valve and the other to a hose coupling. Thereafter, the specimen is placed in a nearly vertical position and drained from air by pressing hydraulic oil through the bottom hose until the whole system is filled with oil. Finally, the valve is closed, the specimen is mounted into a tensile test machine and an external pressurized system is connected to the hose coupling. The external system controls the internal pressure in the specimen.

In order to compensate for pressure fluctuation due to internal volumetric variation of the specimen, the pressure in the external system is regulated based on the pressure data from a pressure sensor located close to the specimen. A schematic illustration and an overview photo of the system used for controlling the pressure in the specimen is illustrated in Figure 6-6 and Figure 6-7. The pressure sensor is also used for recording pressure data during the experiments.

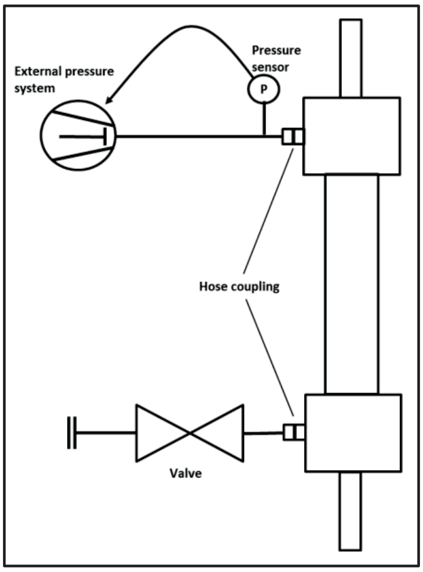

Figure 6-6 Schematic illustration of the pressure regulation system.

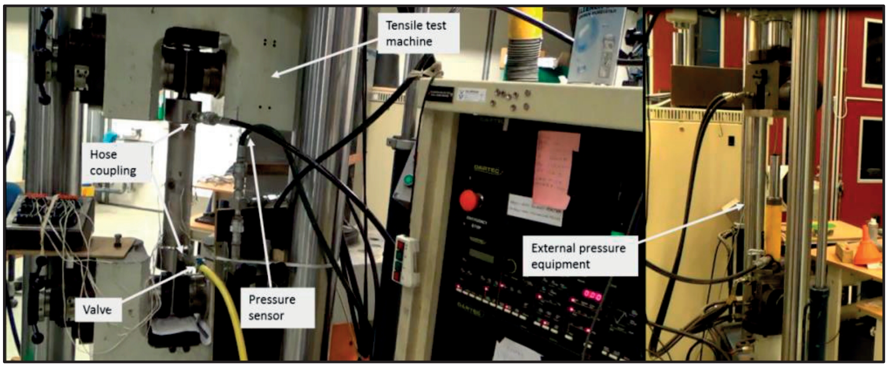

Figure 6-7 Overview photo of the pressure regulation system.

6.3.2. Measurement of strains

Three biaxial strain gages are attached at the center outer wall of the specimen with a distance of 120° between each gage. Each biaxial strain gage is connected to a computer which recorded the axial and circumferential strains.

In order to ensure experimental continuation in case of a single strain measure failure, two extensometers of MTS fabricate which measure the axial strains, are attached close to the center of the outer wall of the specimen and connected to the computer. Extensometers normally allow larger strains before failure in comparison to a strain gage. Hence, the displacement of the tensile test machine is controlled by the average strain of the two extensometers.

A close-up photo of a strain gage and the two extensometers is presented in Figure 6-8.

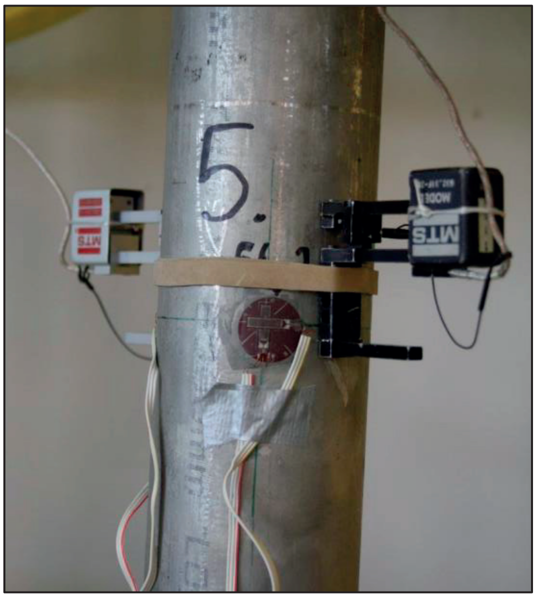

Figure 6-8 Close-up on a strain gage and the two extensometers.

6.4. Internal pressure and axial deformation ranges

In order to facilitate the comparison between the loads acting on the pipe and the allowable loads in the AMSE III code for class 1 piping, the internal pressure and axial deformation range applied in the experiments are chosen in units of S_m. The allowable stress intensity, S_m, is determined in AMSE II Part D. The relation between internal pressure, axial deformation and S_m are derived as well as the chosen load levels for the ratcheting experiments are motivated below.

If the rule of ultimate strength is ignored when determining S_m it holds that:

$$S_m = \frac{2}{3} S_y \tag{Eq. 6-1}$$

Further, according to ASME III NB-3641.1 equation (3) the allowable stresses based on the design pressure is determined as follows:

$$S_m = \frac{P_a\left(D_o - 2 \cdot 0.4 \cdot t\right)}{2t} = \frac{P_a D_o}{2t} - 0.4 P_a \qquad \text{(Eq. 6-2)}$$

In the experiments, the applied pressure is the only primary load and in order to express the primary load in units of S_m, the pressure, P, is derived through (Eq. 6-2) according to:

$$P = \frac{2t}{\left(D_o - 2 \cdot 0.4 \cdot t\right)} \underbrace{F_{prim} S_m}_{= \sigma_{prim}} \qquad \text{(Eq. 6-3)}$$

where F_{prim} corresponds to the primary stress factor.

As the hoop stresses in a thin walled pressure pipe is determined according to:

$$\sigma_{Hoop} = \frac{P D_m}{2t} \qquad \text{(Eq. 6-4)}$$

where D_m corresponds to the mean diameter. It can be observed that (Eq. 6-2) more or less corresponds to (Eq. 6-4). Hence, the allowable hoop stress for a pressurized pipe is roughly $1 \cdot S_m$.

The allowable secondary stress range for class 1 piping is given in ASME NB-3653 equation 12 and equal $3S_m$. In the experiments, the secondary loads are applied as deformation controlled axial displacements. The secondary axial strain ranges are determined through Hooks law as follows:

$$\Delta\varepsilon_{axial} = \frac{E}{L} \underbrace{F_{\sec} \cdot S_m}_{= \Delta\sigma_{\sec}} \qquad \text{(Eq. 6-5)}$$

where F_{sec} corresponds to the secondary stress factor and the modulus of elasticity, E, for each of the materials is chosen according to ASME II part D. Hence, for the 316L specimen E=195 GPa and for the P235 specimen E=205 GPa.

For the ratcheting experiments primary stress levels of $0.5 \cdot S_m$, $1 \cdot S_m$ and $1.25 \cdot S_m$ are chosen. By visualizing each corresponding pressure level in a biaxial stress state together with the von Mises yield surface it is easier to realize the reason for the chosen primary stress levels. This is performed in Figure 6-9 and it shows that for stress level $0.5 \cdot S_m$, the direction of the theoretically initial plastic strain vectors, ε_p(a) and ε_p(b), appears to cancel each other in the axial direction. However, in the hoop direction it is a small advantage of strain in the hoop positive direction which may lead to ratcheting.

Further, a primary stress level $1\cdot S_m$ is of interest only since it correspond to the AMSE maximum allowed pressure. However, it is also interesting from the point of view that both the theoretical initial plastic strain vectors, ε_p(c) and ε_p(d), are pointing in the positive hoop direction. Figure 6-9 shows that in theory, a ratcheting response in the hoop direction is expected for load combinations which are allowed according to ASME.

Finally, a primary stress level of $1.25\cdot S_m$ is of interest since the theoretically initial plastic strain vectors, ε_p(e) and ε_p(f), are strongly pointing in the positive hoop direction. Hence, in theory a ratcheting response is expected for a secondary stress ranges lower than $3\cdot S_m$.

Secondary stress range levels of $2\cdot S_m$, $3\cdot S_m$, $4.5\cdot S_m$, and $6\cdot S_m$ are investigated. However, not all ranges for each pressure level. A summary of the used primary and secondary stress level for each test specimen are presented in Table 6-2.

The only input needed for determining the primary and secondary load is yield strength of each material. As described earlier these values are established during the monatomic experiments which are described in the next section.

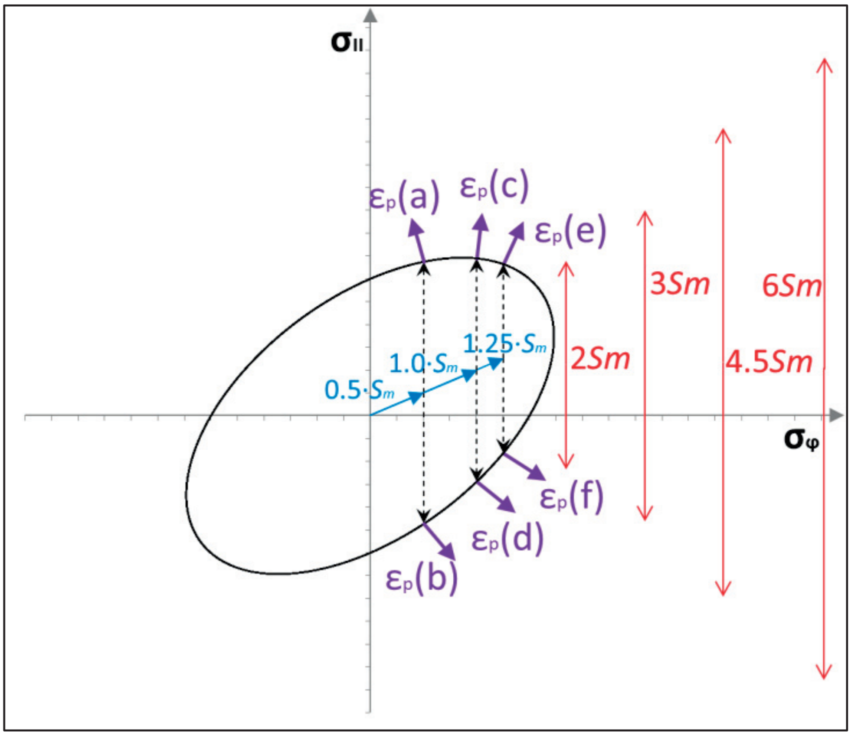

Figure 6-9 **Visualization of applied primary stresses, secondary stress ranges and plastic strain vectors in von Mises initial yield surface.**

Table 6-2 **Hoop stress and axial stress ranges used in the ratcheting experiments.**

Test specimen	Material	Hoop Stress	Axial Stress range
1	316L	$0.5 \cdot S_m$	$3 \cdot S_m$
2	316L	$0.5 \cdot S_m$	$4.5 \cdot S_m$
3	316L	$0.5 \cdot S_m$	$6 \cdot S_m$
4	316L	$1.0 \cdot S_m$	$2 \cdot S_m$
5	316L	$1.0 \cdot S_m$	$3 \cdot S_m$
6	316L	$1.0 \cdot S_m$	$4.5 \cdot S_m$
7	316L	$1.0 \cdot S_m$	$6 \cdot S_m$
8	316L	$1.25 \cdot S_m$	$2 \cdot S_m$
9	316L	$1.25 \cdot S_m$	$3 \cdot S_m$
10	P235	$0.5 \cdot S_m$	$3 \cdot S_m$
11	P235	$0.5 \cdot S_m$	$4.5 \cdot S_m$
12	P235	$0.5 \cdot S_m$	$6 \cdot S_m$
13	P235	$1.0 \cdot S_m$	$2 \cdot S_m$
14	P235	$1.0 \cdot S_m$	$3 \cdot S_m$
15	P235	$1.0 \cdot S_m$	$4.5 \cdot S_m$
16	P235	$1.0 \cdot S_m$	$6 \cdot S_m$
17	P235	$1.25 \cdot S_m$	$2 \cdot S_m$
18	P235	$1.25 \cdot S_m$	$3 \cdot S_m$

6.5. Monotonic experiments

Initially, both uniaxial and multiaxial experiments under load control for determination of the pipe section material properties are conducted. For the uniaxial experiments the test specimen, with no internal pressure, are mounted into a tensile test machine and monotonically loaded in the axial direction until rupture occurred. For the 316L specimen one uniaxial test and for the P235 two uniaxial tests are performed. The reason for the deviation is due to the fact that the material supplier delivered the 316L pipe sections as one 6 meter pipe section but the P235 was delivered in two 3 meter sections. Both the delivered P235 sections were made from the same batch. However, in order to exclude variation of material properties between the two sections a complemented uniaxial test is performed. The test result is more or less identical to the response of the first test. Hence, the material properties for both of the P235 sections are considered equal.

In order to examine the influence of anisotropic material behavior, an additional multiaxial experiment for each of the two specimen types is performed. For this test the specimen is first mounted into the tensile test machine. Thereafter, the test machine is set to load control mode and an internal pressure is introduced into the specimen. The pressure is slowly increased until the measured strains show that the load is approaching the ultimate load.

6.5.1. Stress-strain curves

Stress-strain curves are determined on the basis of the tensile tests and the internal pressure tests. For the latter, the stress-strain curve is derived on the basis of effective stress and effective strain. The results are presented in Figure 6-10 and Figure 6-11 and show that both materials exhibit a difference in stress-strain curve from tension and from pressure to some extent which is expected. The difference is larger for P235 than for 316L which is probably due to the fact that the discontinuous state of plateau strain (Lüders strain) that occurs in tensile tests of ferritic steels is less pronounced in bi-axial stress states, [20].

For cyclic loading of ferritic steels with yield plateau, it is important to recognize that kinematic hardening applied to the uni-axial tension stress-strain curve greatly over-estimates the elastic range. The yield plateau is due to the pinning of dislocations by interstitial atoms such as carbon and nitrogen and really represents an un-natural raise of yield strength. Once the plateau is extinguished it is gone forever and the material behaves as any other strain-hardening material and the elastic range is considerably lower than $2S_y$.

In fact, a back extrapolation of the strain hardening following the plateau would result in a stress-strain curve applicable for cyclic loading. Such a back extrapolation is obviously to some extent arbitrary by nature. For the P235 material therefore, the stress-strain curve is taken half the first unloading curve in the cyclic test for the establishment of the stabilized stress-strain curve[1]. Taking the first unloading cycle ensures no impact of cyclic hardening.

---

[1] In fact no cyclic tests were conducted on P235 tubes. However, cyclic tests were conducted on P265 bars. The stress-strain curve is taken from the latter and scaled for the (minor) difference in yield strength.

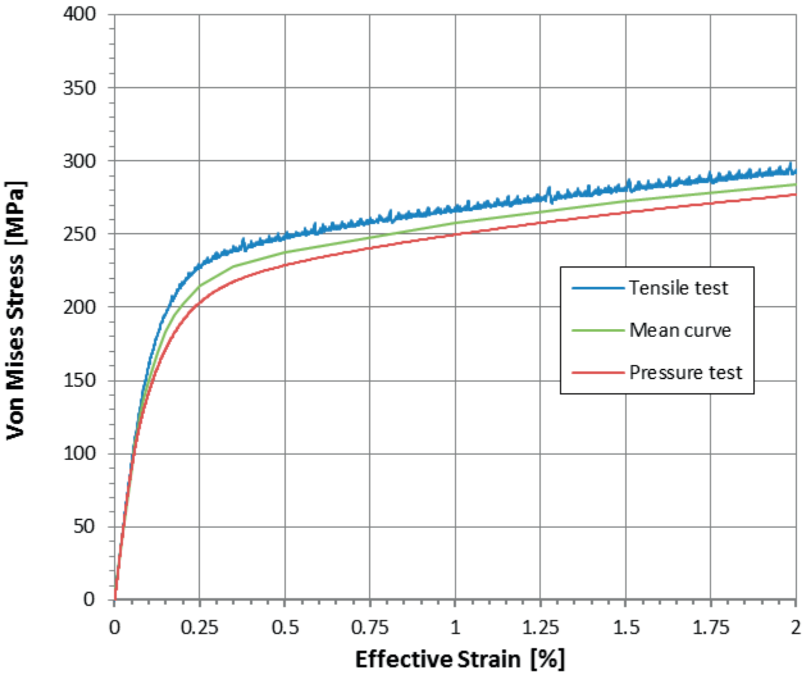

Figure 6-10 Experimental stress-strain curves 316L.

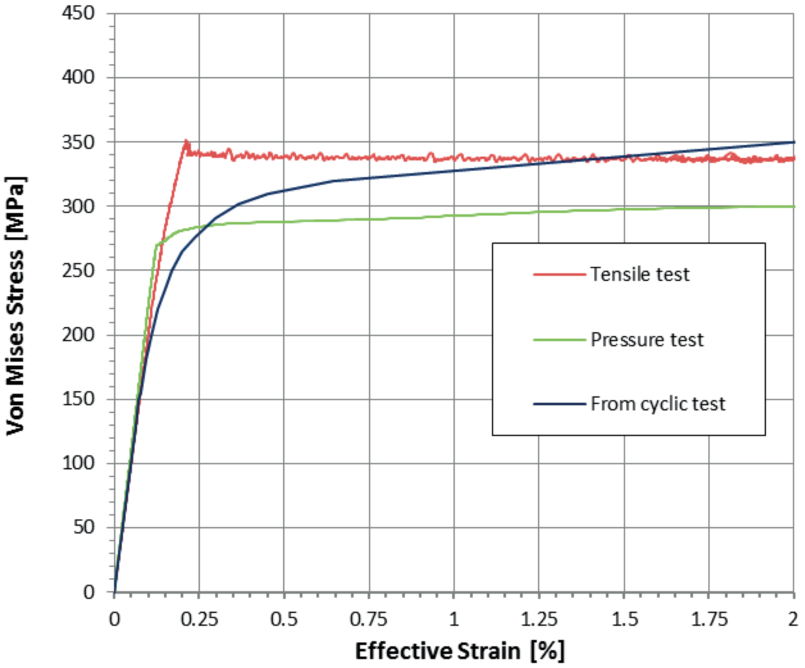

Figure 6-11 Experimental stress-strain curves P235.

6.5.2. Yield strength

For determination of the yield strength the $R_{p0.2}$ method is used. It should be noted that the back-stress interpolation method in these cases give more or less the same yield strength. The yield strength for the uni-axial tests, the internal pressure tests and the mean value of these tests are presented in Table 6-3.

Table 6-3 Yield strengths based on the monotonic experiments.

	S_y^{axial}	$S_y^{pressure}$	S_y^{mean}
P235	340 MPa	285 MPa	312.5 MPa
316L	240 MPa	215 MPa	227.5 MPa

6.6. Ratcheting experiments

After mounting the test specimen into the tensile test machine the pressure is increased and kept constant at the desired level. Thereafter, the tensile machine is switched from load control with zero loads to a displacement control mode. The specimen is then loaded based on the predefined axial displacement range. The displacement is ramped at a constant motion of 10 seconds and when reaching the chosen value the motion is kept constant for 10 seconds. Finally, the specimen is loaded to the originally position. This procedure is repeated for approximately 200 cycles based on the response for each test specimen. During the experiments the following data is measured and saved to a digital file:

- Time [s]
- Pressure [bar]
- Stroke position [mm]
- Tensile test machine load [kN]
- Hoop strain of the three strain gages [mm/mm]
- Axial strain of the three strain gages [mm/mm]
- Axial strain of the two extensometers [mm/mm]

Initially, the data is saved at a rate of 5 Hz. However, after evaluating the results this rate is reduced to 2 Hz.

During the testing of the initial specimens a temperature sensor is attached close to the center of the test specimen. When concluding that the temperature is kept constant during the whole experiment the sensor is removed.

6.6.1. Experimental loading scheme

The yield strength value used when determining the experimental pressure level and cyclic deformation range is chosen to be based on the average of the yield strength from the uniaxial and multiaxial experiments. Hence, the final yield strength values, S_y^{mean} , became 227.5 MPa for the 316L specimen and 312.5 for the P235 specimen. Based on these results the pressure and axial deformation ranges are determined as described in section 6.4. Below in Table 6-4 the loading scheme used for the ratcheting experimental is presented.

Table 6-4 Summary of the ratcheting experimental loading scheme.

Test specimen	Material	Hoop Stress	Pressure	Axial stress range	Axial strain range
1	316L	0.50 S_m	66 bar	3 S_m	0.233 %
2	316L	0.50 S_m	66 bar	4.5 S_m	0.350 %
3	316L	0.50 S_m	66 bar	6 S_m	0.467 %
4	316L	1.00 S_m	131 bar	2 S_m	0.156 %
5	316L	1.00 S_m	131 bar	3 S_m	0.233 %
6	316L	1.00 S_m	131 bar	4.5 S_m	0.350 %
7	316L	1.00 S_m	131 bar	6 S_m	0.467 %
8	316L	1.25 S_m	164 bar	2 S_m	0.156 %
9	316L	1.25 S_m	164 bar	3 S_m	0.233 %
10	P235GH	0.50 S_m	89 bar	3 S_m	0.305 %
11	P235GH	0.50 S_m	89 bar	4.5 S_m	0.457 %
12	P235GH	0.50 S_m	89 bar	6 S_m	0.610 %
13	P235GH	1.00 S_m	179 bar	2 S_m	0.203 %
14	P235GH	1.00 S_m	179 bar	3 S_m	0.305 %
15	P235GH	1.00 S_m	179 bar	4.5 S_m	0.457 %
16	P235GH	1.00 S_m	179 bar	6 S_m	0.610 %
17	P235GH	1.25 S_m	223 bar	2 S_m	0.203 %
18	P235GH	1.25 S_m	223 bar	3 S_m	0.305 %

6.7. Numerical simulations

In order to evaluate the behaviour of different constitutive material models in comparison to the experiments, an extensive amount of numerical analyses are performed. The Prager, Armstrong-Fredrick, Chaboche and Besseling constitutive models are calibrated against the stress-strain curves presented in section 6.5.1. Since the method for calibrating the Armstrong-Fredrick and Chaboche model is ambiguous, detailed studies for different configuration of the material parameters are investigated. In the analyses the test specimens are modelled as axisymmetric and the same primary and secondary loads as used in each experiment are applied.

In the following subsections further details of the numerical simulations are described.

6.7.1. Analysis model

The numerical simulations were performed using the FE software ANSYS [14]. As evaluation of the constitutive models behaviour required an extensive number of analysis runs it is of great importance to reduce the analysis execution time. Further, the considered geometry and load components contribute to a circumferential homogeneous stress field which is suitable for axisymmetric elements. Based on these facts the tube specimens are modelled using axisymmetric elements.

It should be noted that the numerical results also is benchmarked by performing the same analysis using the old but well documented ANSYS PLANE42 element. The results indicate similar responses as with the SOLID272.

According to the ANSYS user manual, see [14] the recommended elements when modelling axisymmetric structural solids is SOLID272. Hence, for simulation of the experimental specimens this element is used.

For modelling the pipes, 20 elements along the pipe thickness and two elements in the pipe axial direction are used, see Figure 6-12. The primary load is applied at the inner surface, line 4 in Figure 6-13, as pressure loads and the bottom surface, line 3 in Figure 6-13, is locked in the pipe axial direction. Further, the secondary loads are applied as boundary condition displacements at the upper surface, line 1 in Figure 6-13, in the pipe axial direction. Finally, large deformation theory is considered in the analyses.

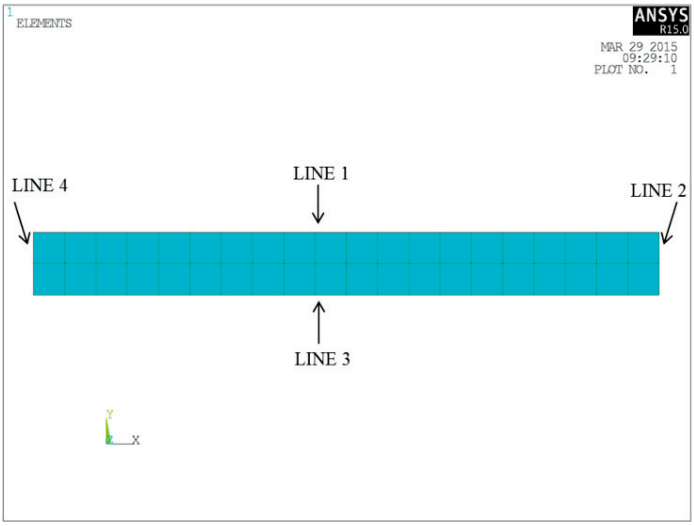

Figure 6-12 **ANSYS axisymmetric model of the pipe wall with the axial center line located one radius to the left.**

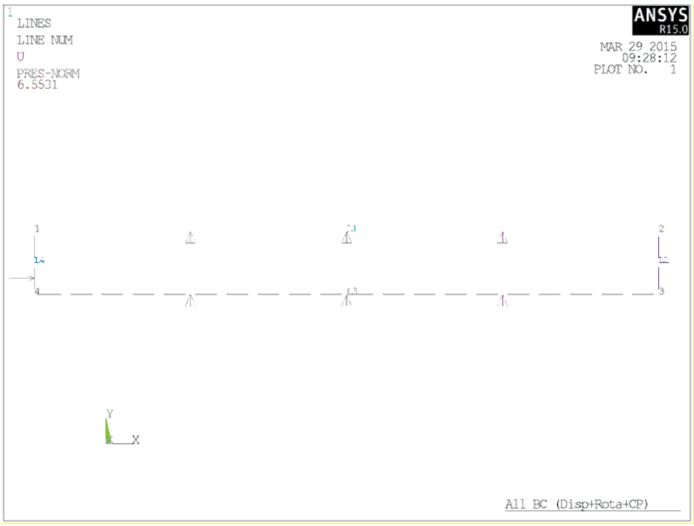

Figure 6-13 Illustration of applied loads and boundary conditions.

6.7.2. Constitutive model parameters

As described earlier, the investigated constitutive material model parameters are calibrated so the material uniaxial response becomes as close as possible to the stress-strain curves presented in section 6.5.1. To be specific, the 316L material models are calibrated against the mean curve presented in Figure 6-10 and the P235 material models are calibrated against the cyclic curve presented in Figure 6-11.

BKIN and EPP

Prager linear kinematic hardening material behavior is activated through the ANSYS BKIN command. The only input for this model is the material yield strength and modulus of plasticity. For the BKIN model the yield strength used in the simulations corresponds to the mean value presented in Table 6-3 and the plastic modulus for both materials is chosen to fit the slope of the curve between the intervals 1-5% of strains. For the EPP (elastic-perfect-plastic) model the same yield strength is used. However, the plastic modulus is very low and equal 10 MPa. In Table 6-5 the parameters used in the presented numerical simulation are presented and in Figure 6-18 and Figure 6-19 the uniaxial response using these parameter configurations are illustrated.

Table 6-5 BKIN material parameters.

	S_y	Modulus of plasticity
P235	312.5 MPa	2.1 GPa
316L	227.5 MPa	2.3 GPa

AF

A material behavior according to the Armstrong-Fredrick kinematic hardening rule is achieved by the use of the ANSYS CHAB command with three material constants. For the Armstrong Fredrick material model it is possible to calibrate the model parameters to either fit the initial, final or something in between the slope of the stress and strain curve. In order to evaluate which calibration method that best simulate the experiment, a sensitivity study using different configuration of material parameters is performed. The result of this study shows that the best results is achieve when the curve is calibrating against the slope of the curve between 1-5% strains together with using a yield strength which is larger than the mean value presented in Table 6-3. In Table 6-6 the final chosen parameters are presented and in Figure 6-18 and Figure 6-19 the uniaxial response using these parameter configurations are illustrated.

Table 6-6 AF material parameters.

	S_y	C_1	γ_1
P235	305 MPa	2250	0.001
316L	245 MPa	2000	0.001

CHAB

A material behavior according to Chaboche kinematic hardening rule is activated through the ANSYS CHAB command and by using seven material parameters. The Chaboche material model may be calibrated to closely fit a stress and strain curve in the span of 0-5% strains. However, different configurations of material parameters may give similar uniaxial responses but the ratcheting response may differ a lot. In order to demonstrate this effect one of the performed sensitivity studies is presented. In this study three different sets of material parameter configurations, according to Table 6-7, are compared. The uniaxial response when using these material configurations are presented in Figure 6-14 to Figure 6-16 and show similar behaviors. However, when performing numerically ratcheting analyses the response variation is significant. This is well illustrated in Figure 6-17 which both shows the experimental response and numerical response using the studied material configurations for ratcheting test 6.

The material configuration used when comparing the numerical simulations with the experiments in section 6.8 is summarized in

Table 6-8 and illustrated for 316L in Figure 6-18 and for P235 in Figure 6-19.

Table 6-7 CHAB material parameters used in the presented sensitivity study.

	S_y	C_1	γ_1	C_2	γ_2	C_3	γ_3
Test0	125 MPa	150000	1666.7	6000	240	2300	2.3
Test1	102.9 MPa	150000	1666.7	6000	240	2300	2.3
Test2	125 MPa	150000	1666.7	5000	150	2000	0.001

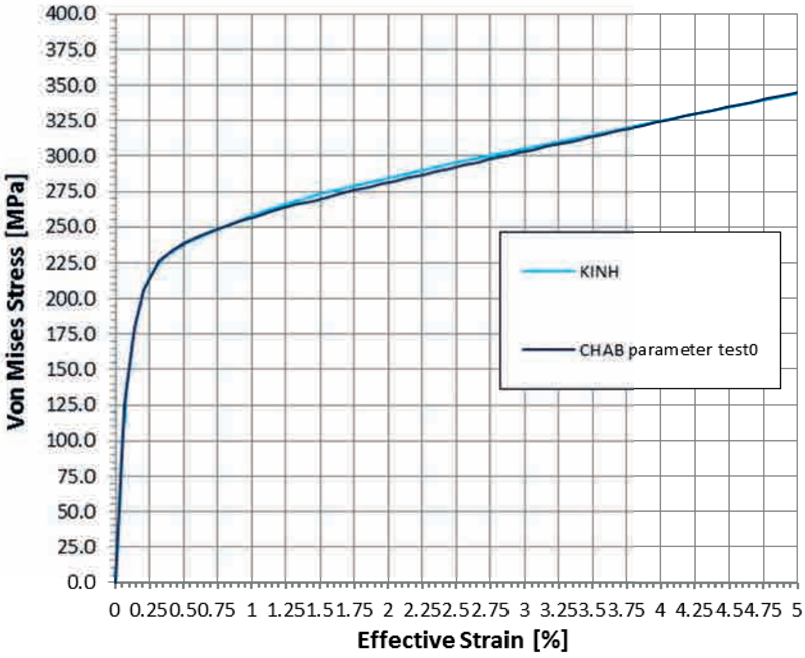

Figure 6-14 ANSYS axisymmetric model of one of the tube specimen.

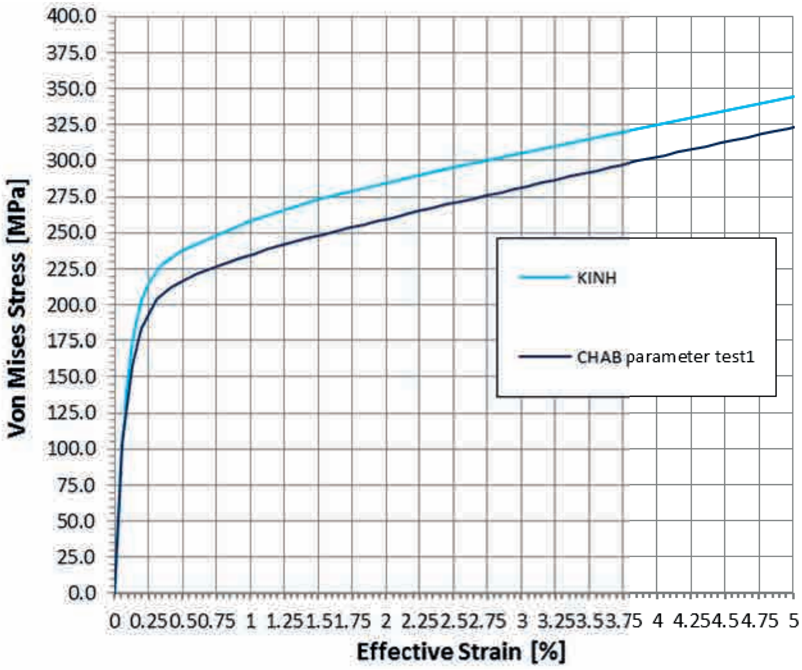

Figure 6-15 ANSYS axisymmetric model of one of the tube specimen.

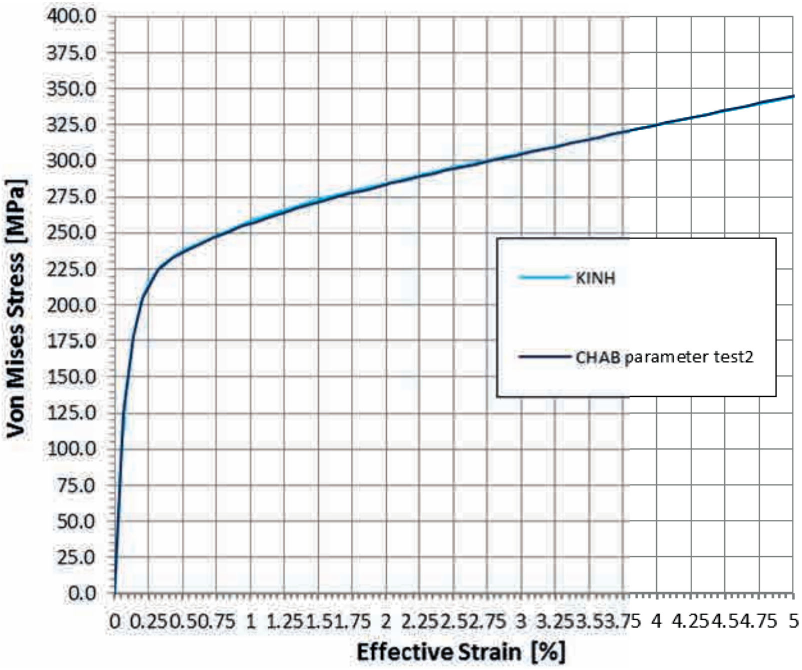

Figure 6-16 ANSYS axisymmetric model of one of the tube specimen.

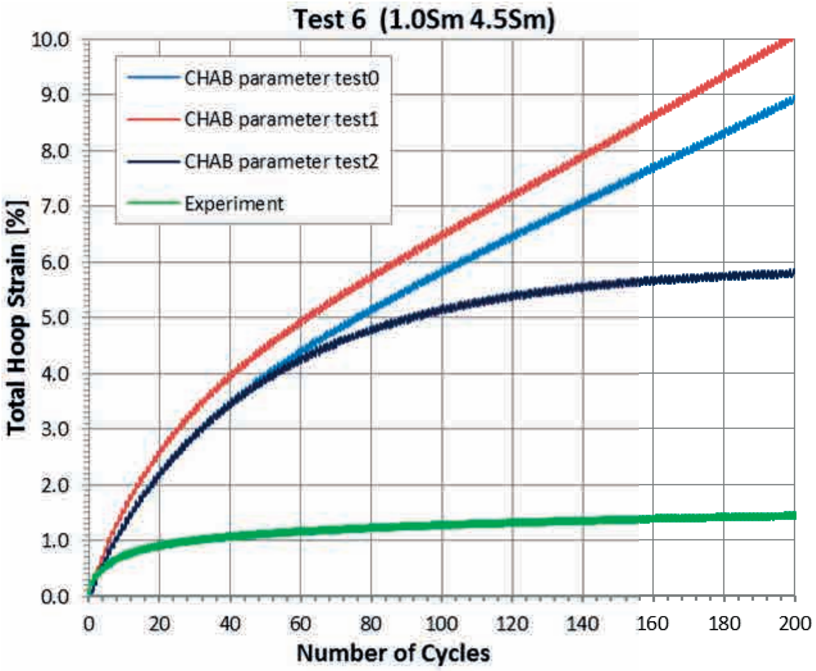

Figure 6-17 ANSYS axisymmetric model of one of the tube specimen.

Table 6-8 CHAB material parameters.

	S_y	C_1	γ_1	C_2	γ_2	C_3	γ_3
P235	145 MPa	700000	9500	85000	950	2300	0.0001
316L	125 MPa	150000	1666.7	5000	150	2000	0.001

KINH

The material behavior of a Besseling multi- linear kinematic hardening model is achieved through the ANSYS KINH command. The only input is stress and strain data points of a stress-strain curve. In ANSYS up to 20 stress and strain data points can be used to build the uniaxial response curve. Hence, a uniaxial response curve very accurately calibrated against a stress-strain curve is quickly achieved.

The data points used when comparing experimental and numerical results are presented in

Table 6-9 and illustrated for 316L in Figure 6-18 and for P235 in Figure 6-19.

Table 6-9 KINH material parameters.

P235		316L	
ε^{tot}	σ	ε^{tot}	σ
0.00026	55 MPa	0.00025	48 MPa
0.00062	129.1 MPa	0.00050	91.5 MPa
0.00073	148.8 MPa	0.00060	106.95 MPa
0.00077	156.5 MPa	0.00065	113.95 MPa
0.00093	181.2 MPa	0.00070	119.9 MPa
0.00107	199.3 MPa	0.00075	125.85 MPa
0.00127	219.6 MPa	0.00085	137.5 MPa
0.00149	236.0 MPa	0.00100	150.5 MPa
0.00171	249.7 MPa	0.00125	169 MPa
0.00201	264.5 MPa	0.00150	183.5 MPa
0.00239	276.0 MPa	0.00175	195 MPa
0.00296	290.3 MPa	0.00200	203 MPa
0.00364	301.3 MPa	0.00250	215.25 MPa
0.00454	310.0 MPa	0.00350	228 MPa
0.00646	319.4 MPa	0.00500	238 MPa
0.03500	383.8 MPa	0.01000	258 MPa
0.06000	438.6 MPa	0.01500	273 MPa
		0.02500	295.5 MPa
		0.05000	344.5 MPa

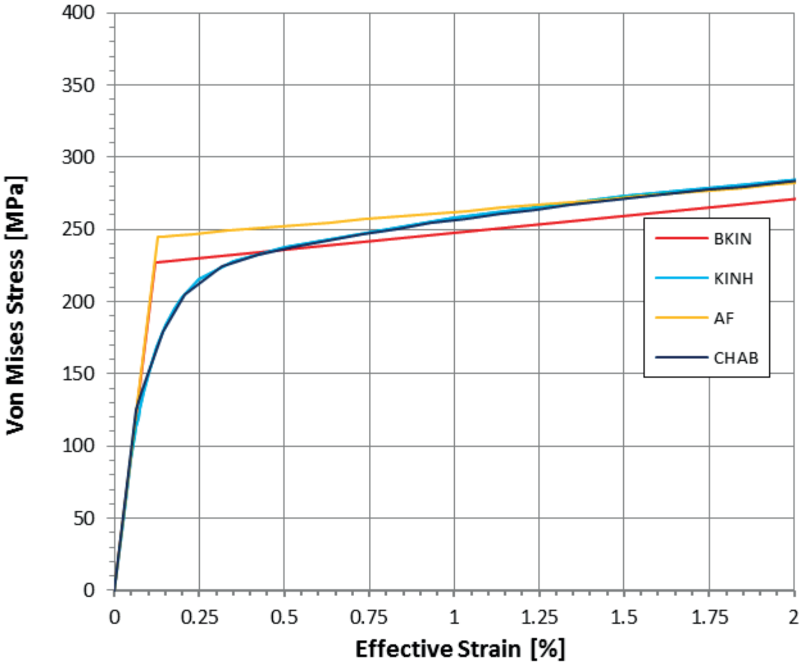

Figure 6-18 Final constitutive model parameters presented in a uni-axial stress-strain curves for 316L.

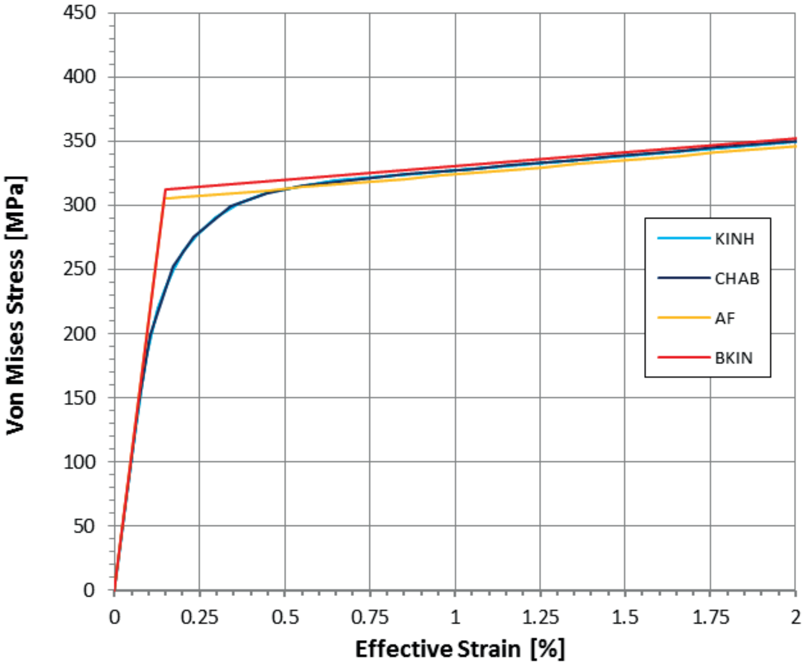

Figure 6-19 Final constitutive model parameters presented in a uni-axial stress-strain curves for P235.

6.8. Experimental & Numerical Simulation Comparisons

In the following section the ratcheting experimental results and numerical results are presented and compared. The results are presented in figures where the total hoop strain is plotted as a function of number of secondary load cycles. The figures also show which stress levels of primary and secondary loads that are used for the considered experiment. Further, the experimental results and each material model are plotted with a unique colour where EPP corresponds to an elastic-perfect-plastic model, BKIN to Prager, AF to Armstrong-Fredericks, CHAB to Chaboche and KINH to Besselings material model.

In total 18 ratcheting experiments are presented. The first nine experiments are performed for the 316L specimens and the remaining tests on the P235 specimens.

The reason for some of the figures not showing results for all the 200 cycles is that one or more strain gages failed during the experiment at the last presented data point. Strain gages failing during experiments at this level of high strains are normal.

In the following subsections the results and comparisons are presented in details.

6.8.1. 316L tubes

The experimental and numerical results for test 1 to 9 are presented in Figure 6-20 to Figure 6-28. From the results a clear response pattern in three steps is distinguished as follows: 1) a relative larger ratcheting response for the first cycles, 2) thereafter the ratcheting response is descending until 3) a final constant slope of the response curve is obtained. For some experiments the final slope is zero or very close to zero and for the remaining it is positive. The magnitude of the ratcheting response, the number of cycles to reach a constant response rate and the slope of the constant response curve follows the proportion of the primary and secondary loads. Hence, the more primary and secondary loads the greater initial ratcheting response, the more number of cycles until a constant response slope is obtained and the larger final slope of the response curve.

The comparisons of the experimental and numerically results show that the Prager model and Armstrong-Fredrick either underestimate or strongly overestimate the response in comparison to the experiments. Further, the Chaboche model strongly overestimates the response at all nine experiments. The results also show that an EPP model strongly overestimates the response in most cases except in the cases with $2S_m$ in secondary range (test 4 and 8) in which the EPP response is below the experimental response. Finally, the results show that the KINH curve more or less overlaps the experimental curve at almost every experiment. Only for a few experiments the KINH response is slightly below the experimental response.

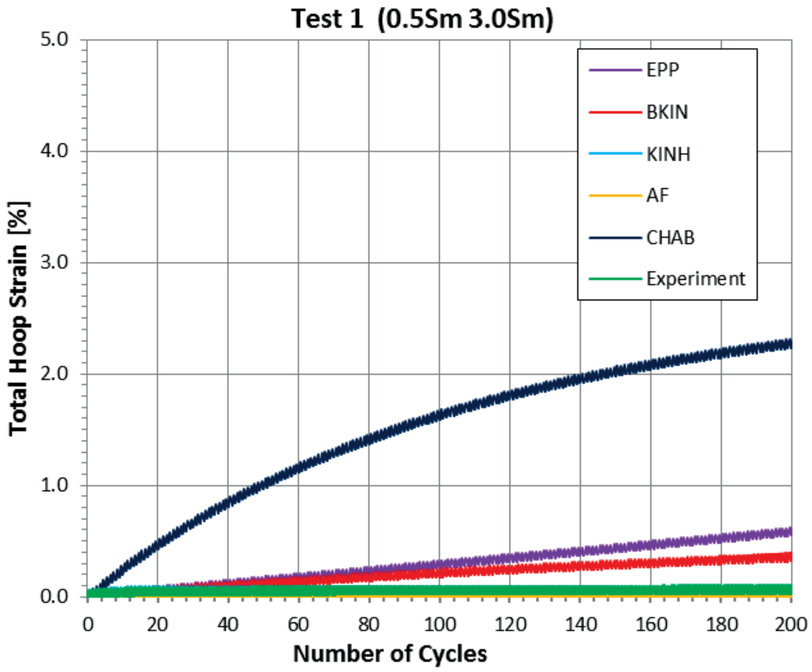

Figure 6-20 **Tubes 316L. Hoop stress *0.5·S*$_m$ and axial strain range corresponding to secondary stress range *3·S*$_m$.**

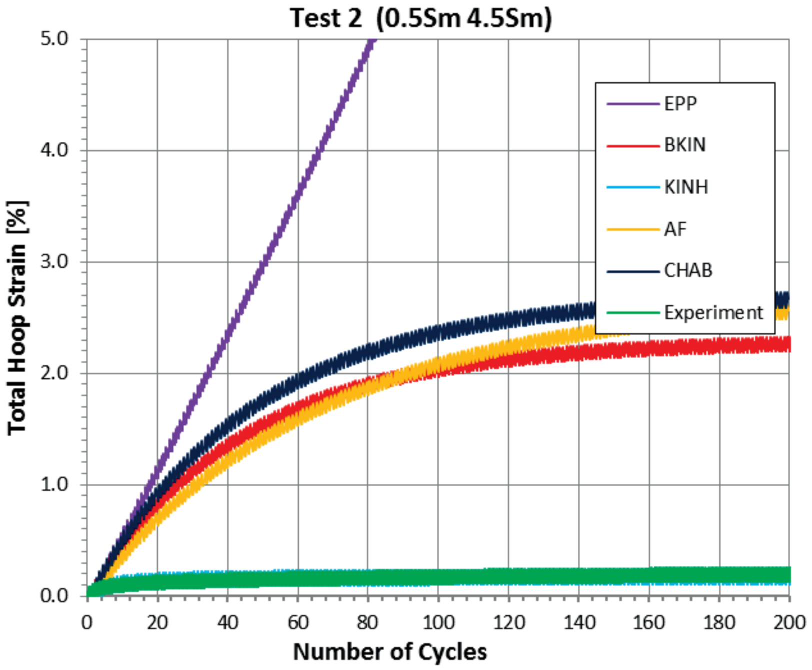

Figure 6-21 **Tubes 316L. Hoop stress *0.5·S*$_m$ and axial strain range corresponding to secondary stress range *4.5·S*$_m$.**

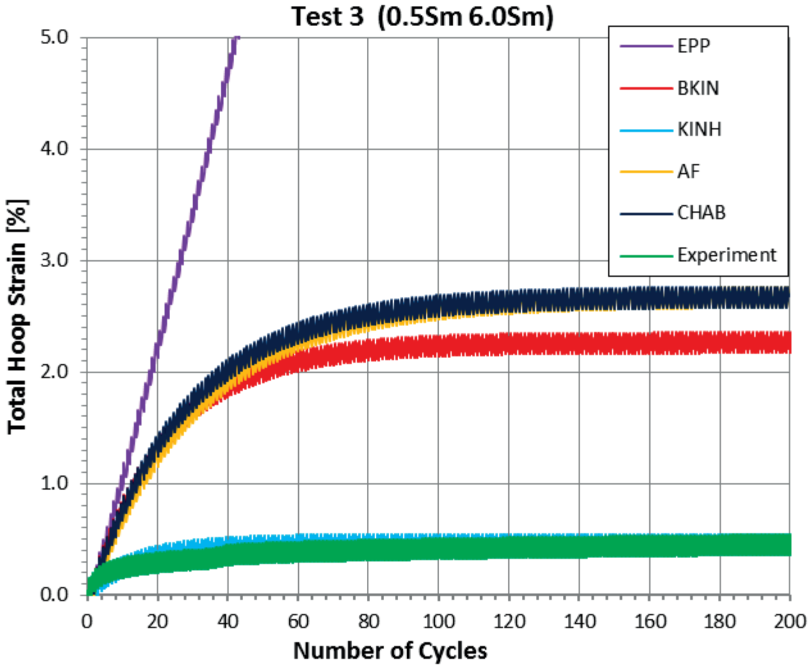

Figure 6-22 Tubes 316L. Hoop stress $0.5 \cdot S_m$ and axial strain range corresponding to secondary stress range $6 \cdot S_m$.

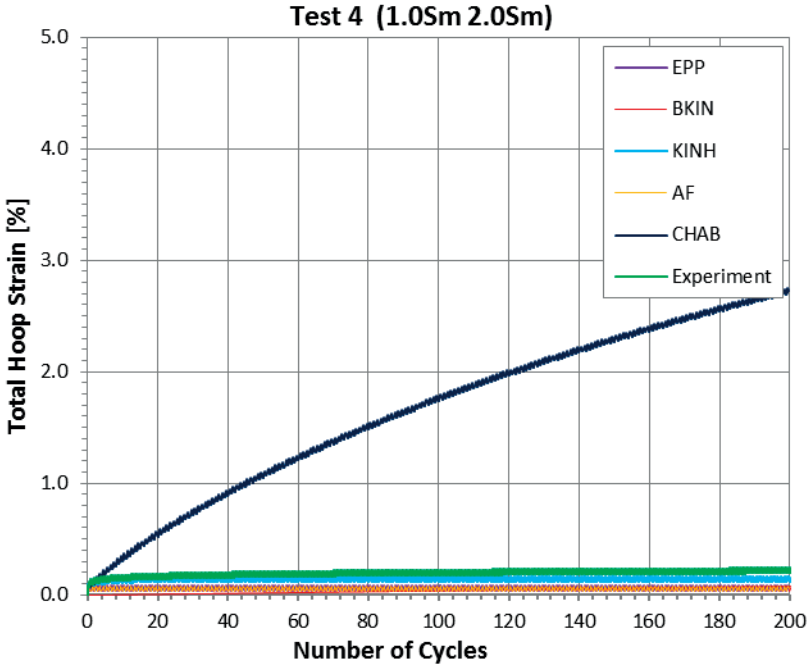

Figure 6-23 Tubes 316L. Hoop stress $1 \cdot S_m$ and axial strain range corresponding to secondary stress range $2 \cdot S_m$.

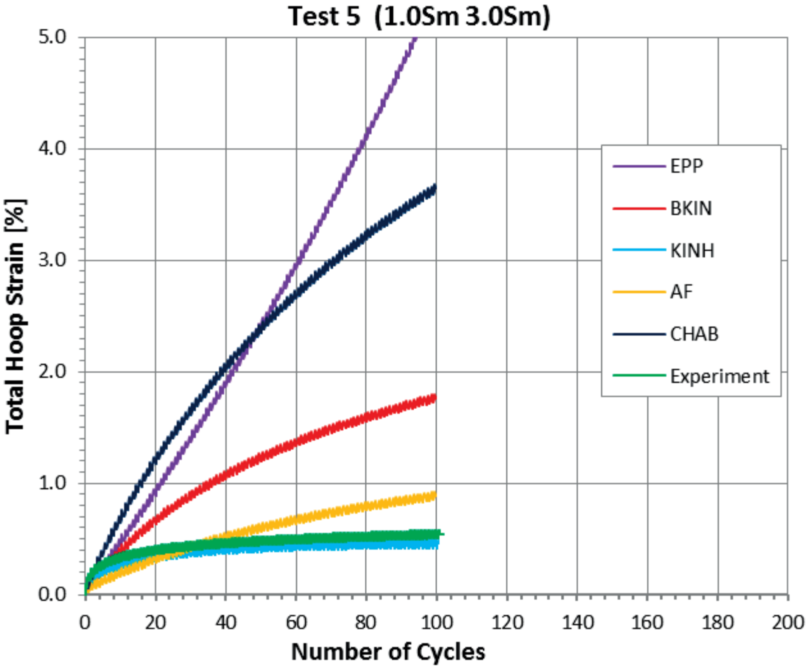

Figure 6-24 Tubes 316L. Hoop stress $1 \cdot S_m$ and axial strain range corresponding to secondary stress range $3 \cdot S_m$.

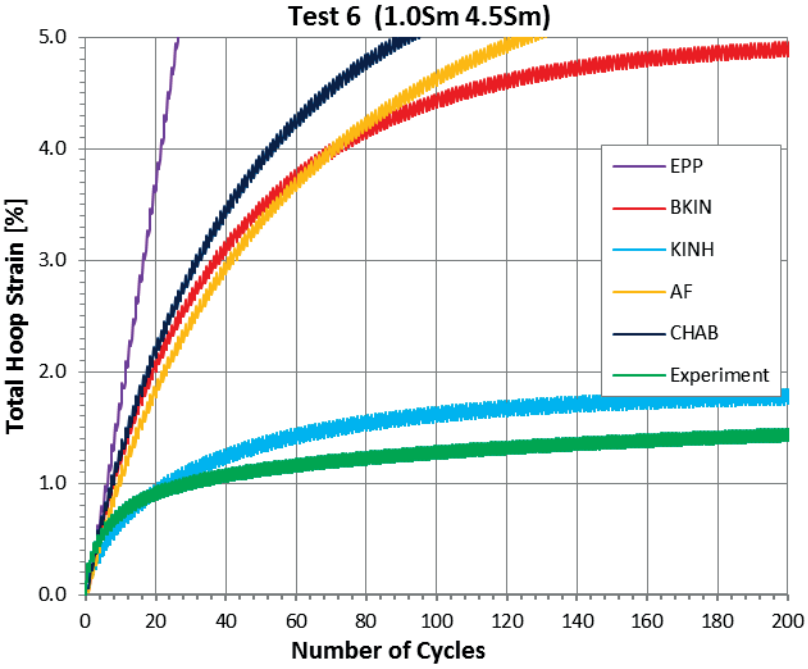

Figure 6-25 Tubes 316L. Hoop stress $1 \cdot S_m$ and axial strain range corresponding to secondary stress range $4.5 \cdot S_m$.

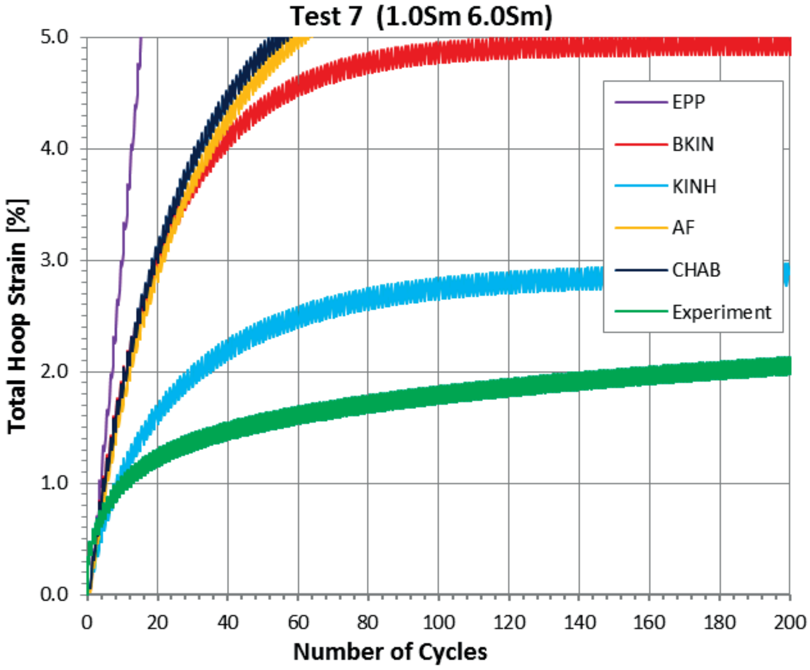

Figure 6-26 Tubes 316L. Hoop stress $1 \cdot S_m$ and axial strain range corresponding to secondary stress range $6 \cdot S_m$.

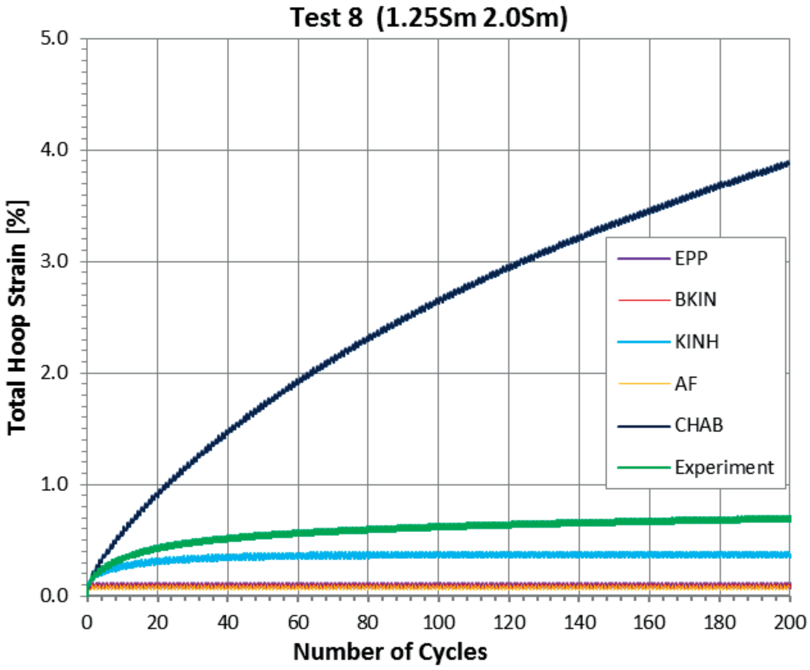

Figure 6-27 Tubes 316L. Hoop stress $1.25 \cdot S_m$ and axial strain range corresponding to secondary stress range $2 \cdot S_m$.

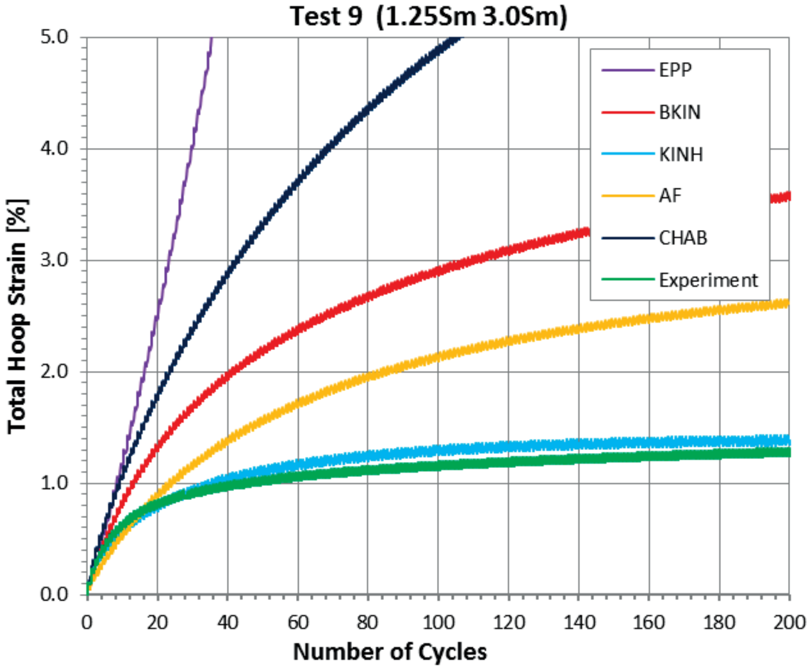

Figure 6-28 **Tubes 316L. Hoop stress $1.25 \cdot S_m$ and axial strain range corresponding to secondary stress range $3 \cdot S_m$.**

6.8.2. Tests on P235 tubes

The experimental and numerical results for test 10 to 18 are presented in Figure 6-29 to Figure 6-37. The experimental results show similar tendency as for the 316L experiments where one can distinguish a response pattern in three steps. However, the response tends to be more extreme for the P235 material in terms of either gives a low response or a very strong response. Further, the number of cycles until a constant slope of the response rate is reached tends to be shorter in comparison to the 316L experiments.

For test 12, presented in Figure 6-31, the secondary range is $7S_m$ instead of 6 S_m. This was due to laboratory related mistakes. However, the numerical simulations are performed using the $7S_m$ secondary stress rate and the results are thereby still of very interests.

The comparisons between experimental and numerical results show the same tendency as for the 316L experiments. Hence, the Prager model and Armstrong-Fredrick either underestimate, overestimate or strongly overestimate the response in comparison to the experiments. Further, the Chaboche model strongly overestimates the response at all nine experiments. The results also show that an EPP model strongly overestimates the response in the most cases except in the cases with $2S_m$ in secondary range (test 13 and 17) in which the EPP response is just below the experimental response. Finally, the results show that also for P235 the KINH curve more or less overlaps the experimental curve at almost every experiment. Only for a few experiments the KINH response reaches a steady state and become below the experimental response.

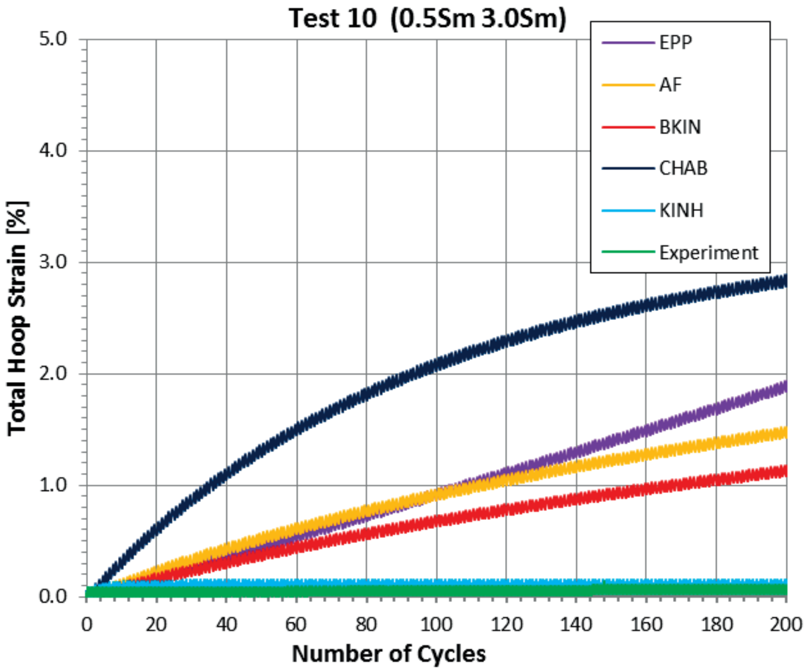

Figure 6-29 Tubes P265. Hoop stress **$0.5 \cdot S_m$** and axial strain range corresponding to secondary stress range **$3 \cdot S_m$**.

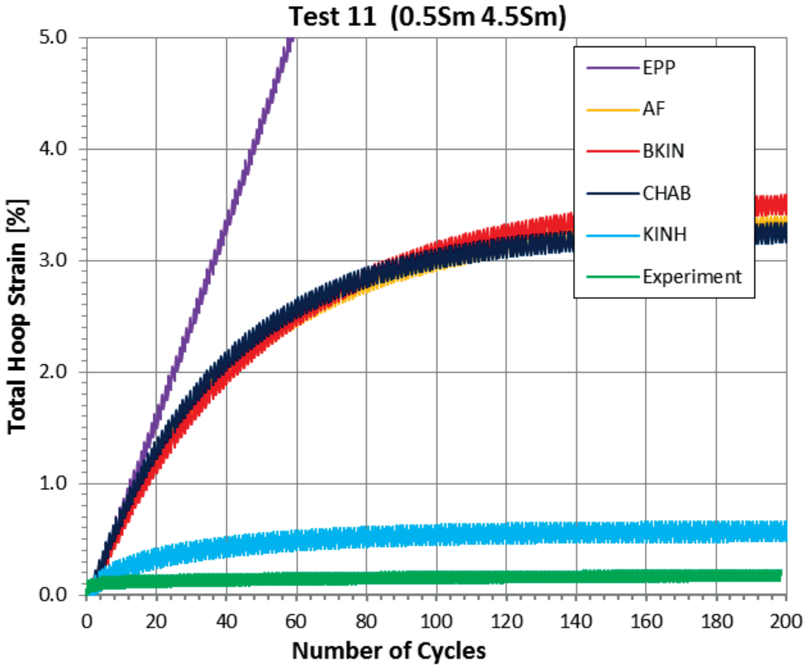

Figure 6-30 Tubes P265. Hoop stress **$0.5 \cdot S_m$** and axial strain range corresponding to secondary stress range **$4.5 \cdot S_m$**.

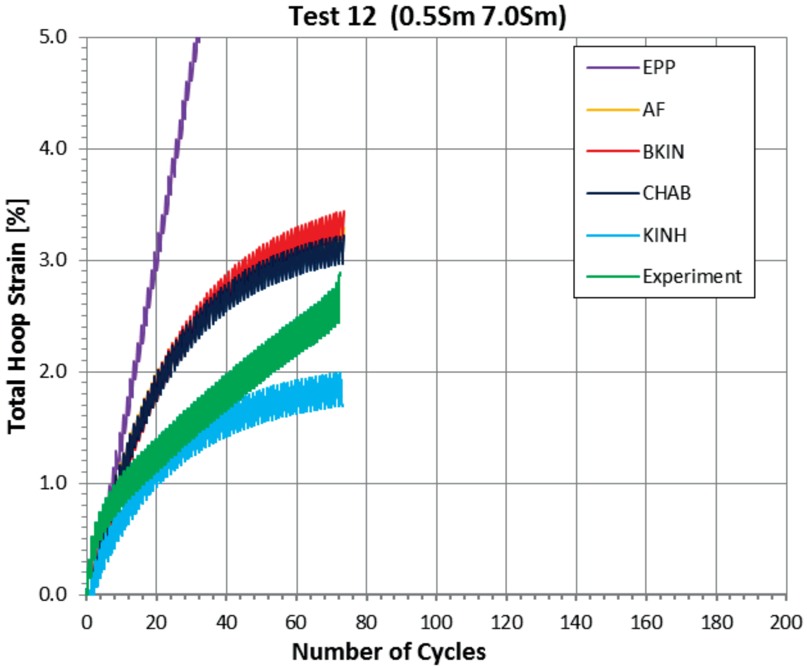

Figure 6-31 **Tubes P265. Hoop stress *0.5·S_m* and axial strain range corresponding to secondary stress range *7.0·S_m*.**

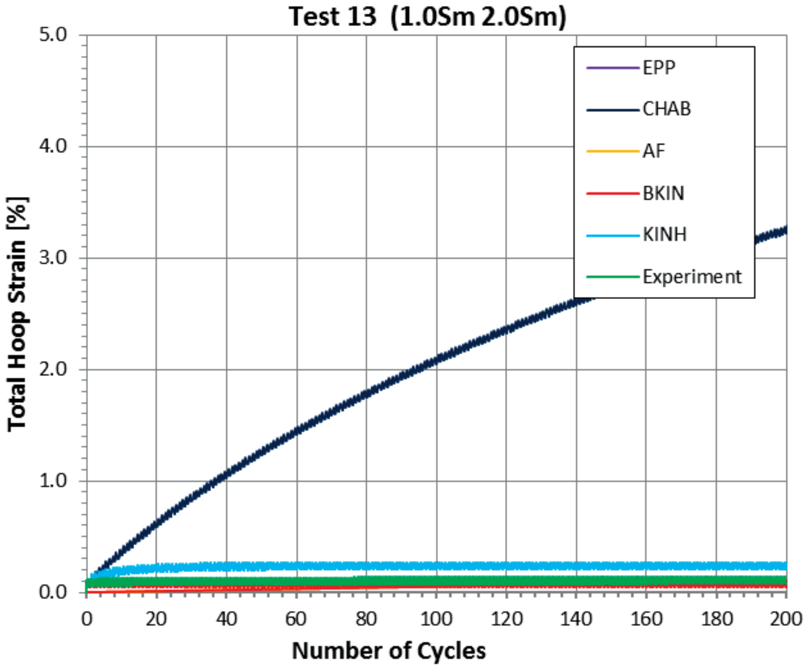

Figure 6-32 **Tubes P265. Hoop stress *1·S_m* and axial strain range corresponding to secondary stress range *2·S_m*.**

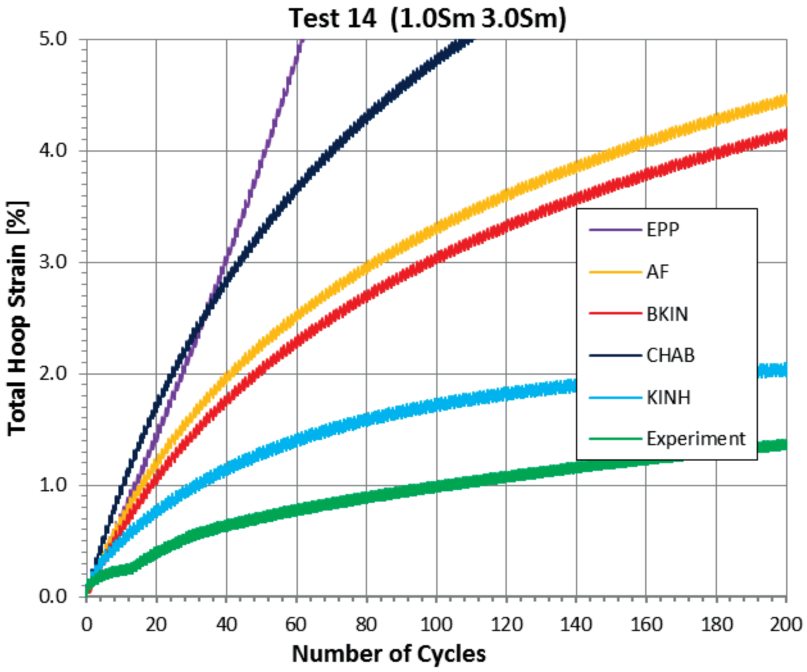

Figure 6-33 Tubes P265. Hoop stress $1 \cdot S_m$ and axial strain range corresponding to secondary stress range $3 \cdot S_m$.

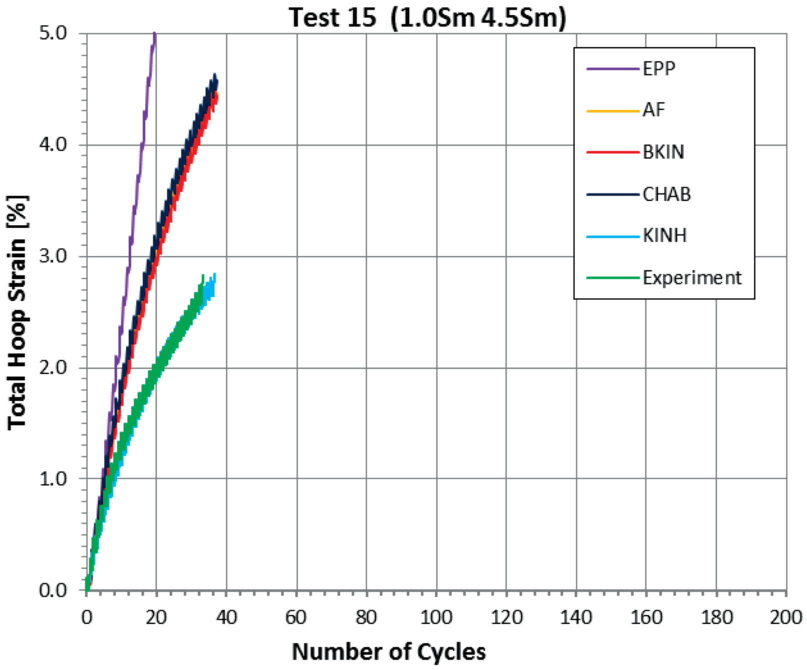

Figure 6-34 Tubes P265. Hoop stress $1 \cdot S_m$ and axial strain range corresponding to secondary stress range $4.5 \cdot S_m$.

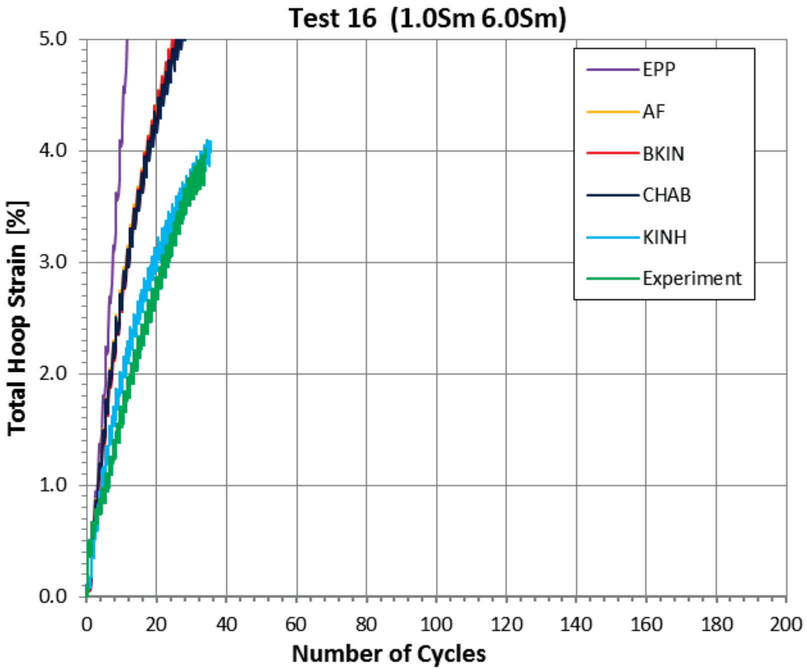

Figure 6-35 Tubes P265. Hoop stress $1 \cdot S_m$ and axial strain range corresponding to secondary stress range $6 \cdot S_m$.

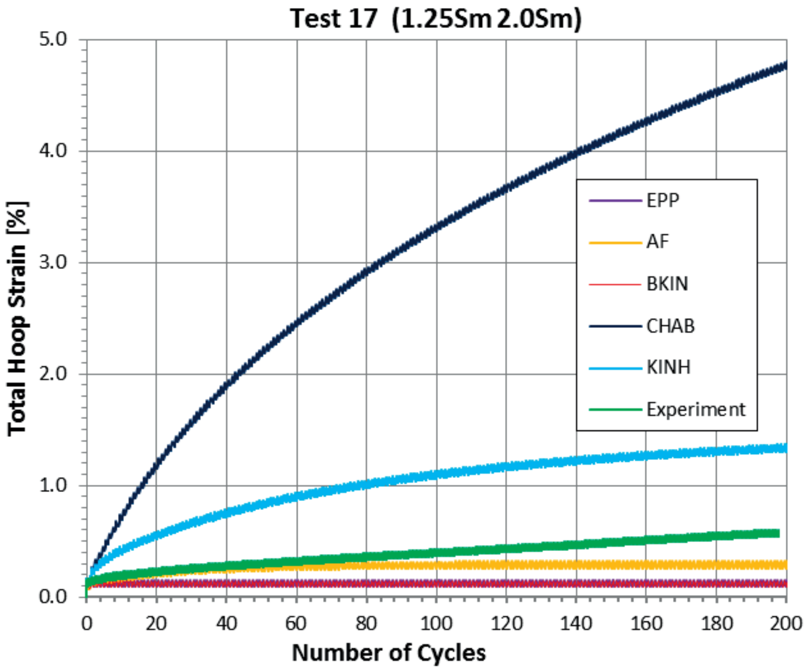

Figure 6-36 Tubes P265. Hoop stress $1.25 \cdot S_m$ and axial strain range corresponding to secondary stress range $2 \cdot S_m$.

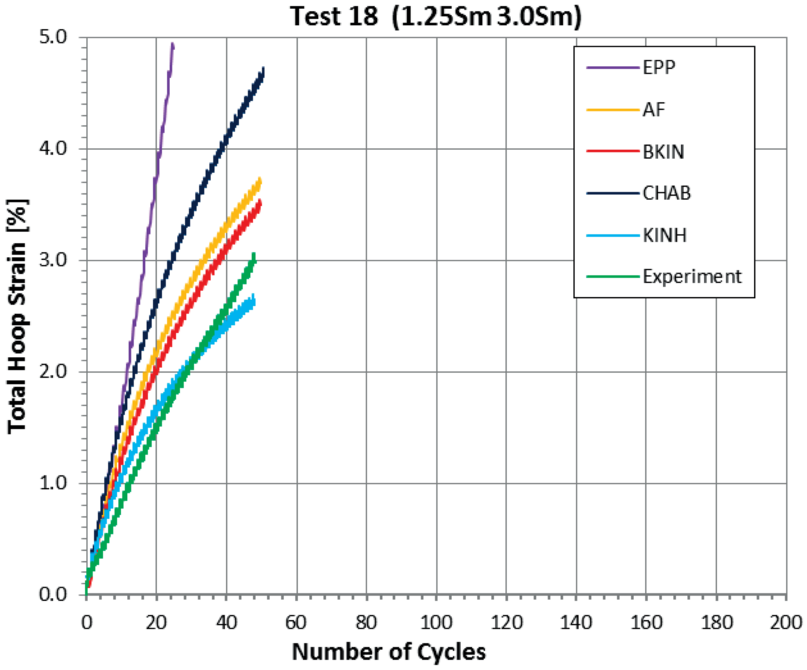

Figure 6-37 Tubes P265. Hoop stress $1.25 \cdot S_m$ and axial strain range corresponding to secondary stress range $3 \cdot S_m$.

6.8.3. Discussion on the descending rate of ratcheting

The anatomy of the Besseling model in ratcheting for cyclic axial strain loading of pressurized tubes is illustrated below. Consider for this purpose two simplified stress-strain curves according to Figure 6-38. Assuming Besseling material, it holds for both materials

$$S_{y1} = 200 \text{ MPa}$$

$$E_{T2} = \frac{300 - 200}{0.005 - 0.001} = 25.000 \text{ MPa}$$

$$\alpha_2 = \frac{25.000}{200.000} = 0.125$$

$$\alpha_1 = 1 - 0.125 = 0.875$$

and

$$S_{y2} = 0.005 \cdot 200.000 = 1.000 \text{ MPa} \qquad \text{red curve}$$

$$S_{y2} = 0.007 \cdot 200.000 = 1.400 \text{ MPa} \qquad \text{black curve}$$

The corresponding yield surfaces are shown in Figure 6-39. Consider a loading constituted by internal pressure such that the hoop stress is kept at a magnitude $\sigma_{\varphi} = S_{y1}/1.5$ while applying cyclic axial strain ranges $\Delta\varepsilon_{\square} = 3\varepsilon_y$.

Denote the application of strain in the positive and negative directions loading and unloading, respectively. Initially, the stress scheme is according to Figure 6-40 and it is realized that plastic hoop strains in sub-volume 1 are produced both at loading and at unloading since both plastic strain increment vectors have a component in the positive hoop direction.

Following a few cycles, consider a removal of all loads. If not connected to each other, sub-volume 1 would, due to the accumulated plastic hoop strains, be permanently elongated in the hoop direction whereas sub-volume 2 would return to its original shape. However, the sub-volumes are subjected to the same total strains at all time and hence compressive residual stresses are introduced in sub-volume1 whereas tensile residual stresses are introduced in sub-volume2.

Effectively, this means in Besseling there are translation of stress states rather than the translation of yield surfaces seen in the conventional kinematic hardening models. This fact is already pointed out for the uni-axial case in section 4 above and the mechanism is hence the same for multi-axial stress states.

The translation of stress state in subvolume 1 is in the compressive hoop direction and red arrow in Figure 6-40 is moving along in the same direction. In this motion, the plastic hoop strain increments at both loading and unloading are decreasing which results in a decending ratcheting rate. The ratchet rate will descend at each cycle since the residual stress in subvolume 1 is progressively more compressive. When the red arrow is aligned with the axial stress axis, shake-down occurs and the residual compressive stress in subvolume 1 is $S_{y1}/1.5$. The condition for this to be possible is that subvolume 2 is able to resist the stresses from internal pressure in addition to balancing the compressive residual stress in subvolume 1. This is true in the considered example for

$$S_{y2} \geq \frac{S_{y1}}{1.5}\left(\frac{\alpha_1}{\alpha_2}+1\right) = \frac{200}{1.5}\left(\frac{0.875}{0.125}+1\right) = 1070\,\mathrm{MPa}$$

in which the first term is tension from balancing compressive residual stress in subvolume 1, and the second term is pressure stress. Obviously this means the material with the black stress-strain curve is able to shake-down, whereas the material with red stress-strain curve is not. This is in fact the outcome of simulation according to Figure 6-41.

Obviously the example is simple but it exhibits the elements of a real problem and it demonstrates elegantly the internal mechanics of the Besseling constitutive model.

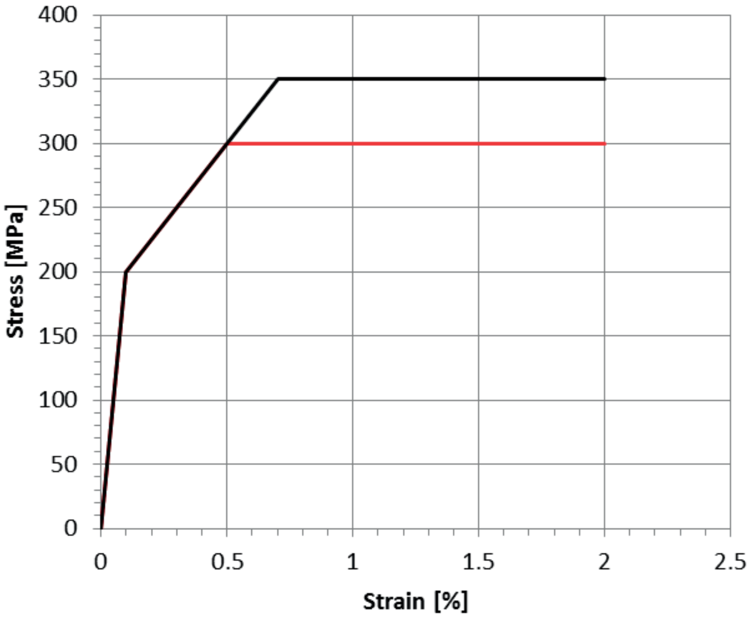

Figure 6-38 Two simplified stress-strain curves.

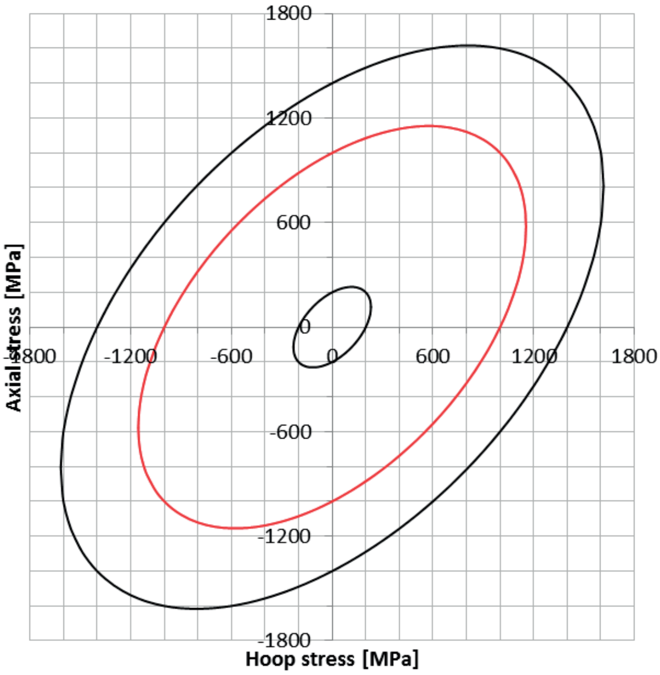

Figure 6-39 Yield surfaces for sub-volume materials in Besseling models corresponding to the stress-strain curves in Figure 6-38 above. The internal yield surface is the same for both models.

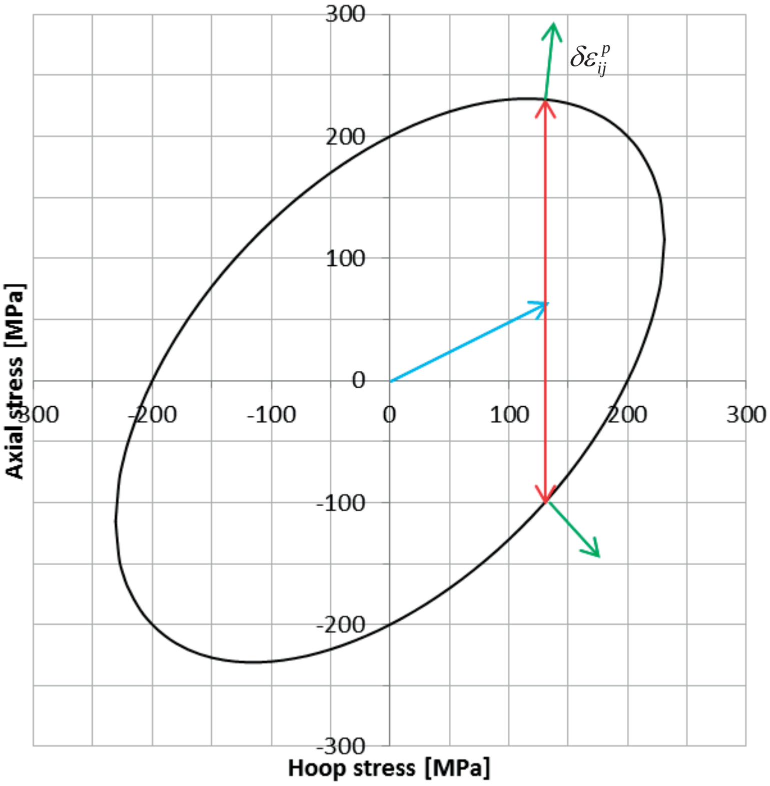

Figure 6-40 Internal yield surface and initial loading. Pressure loading (blue arrow) followed by cyclic axial strain ranges (red arrows) by which plastic strains (green arrows) are produced.

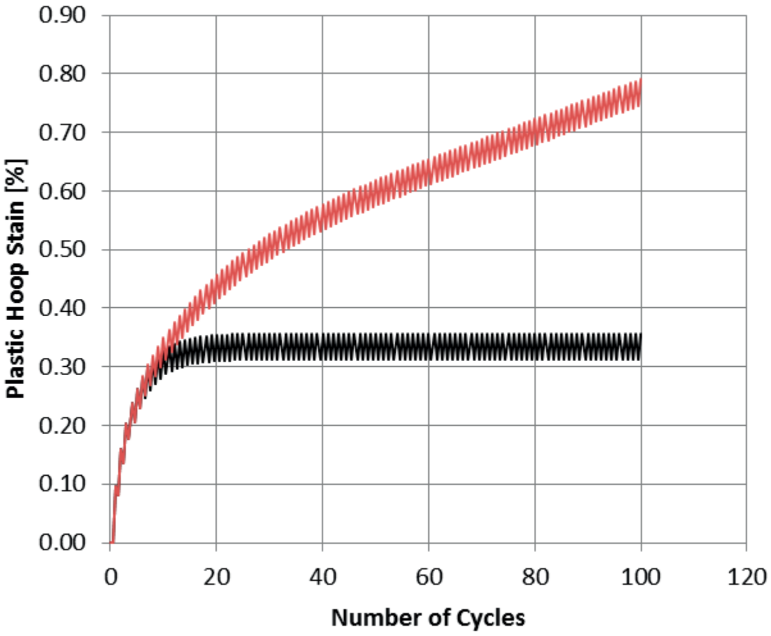

Figure 6-41 Ratcheting response for the two stress-strain curves above to the example imposed pressure and cyclic strain loading.

Discussions

Two-rod tests and tube tests form basis for this investigation. Specimens are made of the ferritic steels P235 and P265 as well as the austenitic steel 316L. Determination of the constants in the five constitutive models used in the project is based on material characterisation of the three materials. This characterisation involves tensile testing, fully-reversed strain controlled cycling and material ratcheting testing. The possibility to simulate the response of conducted experiments with the different material models is of main interest. Development of general recommendations for how ratcheting in structures subjected to cyclic plastic deformation can be predicted by numerical simulation is the goal of the project.

Simulation of cyclic plastic deformation should be done with an as simple constitutive model as possible, still capturing the essential response. Important motivations are that simple models are easier to understand and work with and that fewer tests are needed for characterisation of the material.

The simplest model that can be used in this context is the ideal plastic model. For this model, only Young’s modulus and the yield stress are needed as input to describe the material. If no tensile test results are available, data can be taken from material data sheets where the minimum yield stress can be found. Simulation of cyclic plastic deformation with an ideal plastic model most often overestimates strain development. If the material shows a strong cyclic softening, this might not be the case. Moreover, it may not be the case for small strain ranges, for which it may predict elastic behaviour although ratcheting is experimentally observed. However, for these cases the ratcheting is in general minor and negligible anyway. In most cases the model grossly overestimates ratcheting as it cannot account for decay in ratcheting rate. Thus, the ideal plastic model may be used for establishment of an upper bound. The use of this model may be the first step in an analysis of the plastic response of a structure. Results from such an analysis might be sufficient for structural verification of the component.

If the use of an ideal plastic model results in violated design criteria, a more complex constitutive model can be applied. The linear kinematic hardening models are such models. In this project, a bi-linear and a multi-linear model have been investigated. In addition to the material parameters needed for the ideal plastic model, the plastic hardening needs to be described. For the bi-linear model, the plastic modulus is needed while for the multi-linear model, the shape of the stress-strain curve is required as input. The linear models cannot capture material ratcheting. If this phenomenon dominates the structural response, a more advanced model is needed. However, for pressure equipment subjected to cyclic plastic deformation, structural ratcheting often dominates over material ratcheting. The reason for this might be that the direction for which reversed plastic cycling takes place normally does not coincide with the direction of the incremental plastic deformation (ratcheting). This fact facilitates the use of linear models in the analysis of pressure equipment subjected to cyclic plastic deformation. Investigation of the tube components in this project confirms that the linear models can predict their structural response well. Also the two-rod test responses are often well predicted with the linear models.

The most advanced models investigated in this project are the nonlinear kinematic hardening models, i.e. Armstrong-Frederick and Chaboche. These models can capture both structural and material ratcheting. Regarding pressure equipment and simulation of cyclic plastic deformation, the phenomenon material ratcheting can often be disregarded as discussed above. This means that these more advanced models are not in general needed when simulating pressure equipment responses. One way to determine if this is the case is to investigate how the cyclic plastic deformation evolves during the simulation. The more the direction for which reversed plastic cycling takes place coincides with the direction of incremental plastic deformation (ratcheting), the more important it is to use nonlinear models instead of linear. One disadvantage with nonlinear models is that more tests for characterisation of the material have to be conducted. Fully-reversed strain cycling data is needed in order to determine the material constants and make full use of these more advanced models. Using only the tensile curve for defining the models would result in incorrect cyclic behaviour if material ratcheting is present.

Among the models investigated, cyclic hardening or cyclic softening can be captured only with the nonlinear models. This is done by defining at least two additional material constants. For cases when material ratcheting is present, this possibility can improve the model. Assuming that material ratcheting occurs in a cyclic softening material, simulated strain development would be underestimated if constants in the nonlinear model are determined based only on the tensile curve.

Results from simulation of the two-rod tests with nonlinear models point out the importance of understanding the impact of the bounding stress on the numerical response. Before a nonlinear model is used in a simulation, the bounding stress should be determined for a better understanding of what type of response that can be expected from the numerical results.

For the same load combination of primary stress and secondary stress range, the two-rod test produces more strain than the tube test does. One explanation for this might be that the direction in which incremental plastic deformation takes place and the direction for which potential reversed plastic cycling takes place, coincides for the two-rod test but not for the tube test. This means that material ratcheting should be more pronounced in the two-rod tests than in the tube tests. Overestimation of hoop strain in the tube tests with the Chaboche model indicates the minor impact of material ratcheting. For the two-rod tests, overestimation of strain with the Chaboche model is less pronounced.

7. Conclusions and recommendations

Conclusions and recommendations for numerical simulation of cyclic plastic deformation in structures are given as follows:

1. Simulation of cyclic plastic deformation should be done with an as simple constitutive model as possible, still capturing the essential response. Important reasons are that simple models are easier to understand and work with and that fewer tests are needed for characterisation of the material.

2. The simplest model that can be used for simulation of cyclic plastic deformation is the ideal plastic model. In most cases this model overestimates strain development. If the material shows a strong cyclic softening, this might not be the case. Moreover, it may not be the case for small strain ranges, for which it may predict elastic behaviour although ratcheting is experimentally observed. However, for these cases the ratcheting is in general minor and negligible anyway. In most cases the model grossly overestimates ratcheting as it cannot account for decay in ratcheting rate. Thus, the ideal plastic model may be used for establishment of an upper bound. The use of this model may be the first step in an analysis of the plastic response of a structure. Minimum yield stress according to material data sheets should then be used. Results from such an analysis might be sufficient for structural verification of the component.

3. For pressure equipment subjected to cyclic plastic deformation, structural ratcheting often dominates over material ratcheting. The reason for this is that the direction for which reversed plastic cycling takes place normally does not coincide with the direction of incremental plastic deformation (ratcheting). This fact facilitates the use of linear models in the analysis of pressure equipment subjected to cyclic plastic deformation.

4. Among the constitutive models investigated, the Besseling multi-linear model is recommended for simulation of pressure equipment subjected to cyclic plastic deformation.

5. An important feature for materials exhibiting a yield plateau – which most carbon steels do – is that the applicable stress-strain curve for cyclic analysis with kinematic models is neither the monotonic curve nor the elastic-perfectly plastic idealization. A compressive stress reversal following the yield plateau in tension reveals a considerable smaller elastic range than $2Sy$ and the

material behaves like any other strain hardening material with the characteristic knee at yielding. In fact, the behaviour for cyclic loading is that of a material with a stress-strain curve obtained by back extrapolation of the strain hardening portion of the monotonic curve such that a stress-strain curve similar to austenitic steels is obtained. The stress-strain curve applicable for cyclic loading is half the reversed curve following the yield plateau in tension.

6. Code information on material strength is yield strength and tensile strength. The construction of stress-strain curves from this information is not obvious. The Eurocode 3, [21], and RCC-MRx, [22], give analytical expressions for stress-strain curves as function of yield and tensile strength and this may constitute an applicable procedure for austenitic steels. For carbon steels however, there is no obvious route to determine applicable stress-strain curves for cyclic analysis. The experimental procedure for determining such curves are however simple as outlined above. It is recommended that such curves are derived for common pressure vessel steels as an extension to this project. The extent of such an effort would be considerably smaller than the extent of the project reported herein.

8. Acknowledgements

Forsmarks Kraftgrupp AB, OKG AB, Ringhals AB, Teollisuuden Voima Oij (TVO) and the Swedish Radiation Safety Authority (SSM) are all acknowledged for financing this project.

Mikael Möller and Andreas Gustafsson would like to specially thank AREVA NP Uddcomb for the priority and the allowance to dedicate this project a great amount of time.

Lars Åström and his colleges at Complab at LTU have conducted the tube experiments with honors.

Gustav Eklund and Mattias Skog have both been deeply involved in the investigation of the two materials 316L and P265 by use of the two-rod test procedure. Their respective Master Thesis work covers development of the two-rod test procedure, material characterisation of 316L and P265, two-rod testing of 316L and P265, numerical simulation of all experiments and evaluation of results achieved. Their input to this project is most acknowledged.

All experiments related to the two-rod test approach were conducted at the Department of Solid Mechanics at the Royal Institute of Technology (KTH). Martin Öberg and Hans Öberg are acknowledged for the development of the control system for the two-rod test machines, for their help with the experiments and for valuable technical discussions.

Pär Ljustell at Inspecta Nuclear and Magnus Dahlberg at Inspecta Technology are acknowledged for valuable technical discussions.

9. References

[1] Möller, M., *Progressive deformation – the mechanics and the relation to the 3Sm-criterion*. Presentation Kärnteknikdagarna 2008 (Inspecta), Stockholm.

[2] Besseling, J.F, *A Theory of Elastic, Plastic, and Creep Deformations of an Initially Isotropic Material Showing Anisotropic Strain-Hardening Creep Recovery and Secondary Creep*, Journal of Applied Mechanics. 529-536, 1958.

[3] Mroz, Z., *On the description of anisotropic hardening*, J. Mech. Phys. Solids, Vol 15, pp163-175, 1967.

[4] Chaboche, J.L, *Time independent constitutive theories for cyclic plasticity*, Int. J. Plasticity, vol 2, pp 149-188, 1986.

[5] Armstrong, P.J; Frederick, C.O., *A mathematical representation of the multiaxial Bauschinger effect*, CEGB report RD/B/N 731, Central Electricity Generating Bauart, 1966.

[6] *ASME Boiler & Pressure Vessel Code*, New York: The American Society of Mechanical Engineers, 2007.

[7] Bree, J., *Elastic-plastic behaviour of thin tubes subjected to internal pressure and intermittent high-heat fluxes with application to fast-nuclear-fuel elements*, *J. of Strain Analysis*, Vol. 2, No. 3, 1967.

[8] SSM Research report 2010:45, *Evaluation of models for cyclic plastic deformation – A literature study*, Swedish Radiation Safety Authority, 2010.

[9] Von Mises, R., *Mechanik der Festen Korper im Plastisch Deformablen Zustand*, Nachr. Ges. Wiss. Gottingen, pp. 582., 1913.

[10] Chen, W.F; Han, D.J, *Plasticity for Structural Engineers*, New York: Springer-Verlag, 1988.

[11] Ottosen, N. S.; Ristinmaa, M. *The mechanics of constitutive modelling*, Elsevier, 2005.

[12] Bauschinger, J., *Über die Veränderung det Elastizitätsgrenze und der Festigkeit des Eisens und Stahls durch Strecken und Quetschen, durch Erwärmen und Abkülen und oftmal wiederholte Beanspruchung, Mitteilungen 15 aus dem mechanisch*, Technische Laboratorium der K. poöytechnischen Shule, München, 1886.

[13] Prager, W., *The Theory of Plasticity: A survey of Recent Achievements*, Proceedings of the Institution of Mechanical Engineers. 169.1, pp 41-57, 1955.

[14] ANSYS Inc., ANSYS version 15.0.

[15] ASTM E606, *Standard Test Method for Strain-Controlled Fatigue Testing*, West Conshohocken: ASTM international, 2012.

[16] P. v. Eeten and F. Nilsson, *Constant and variable amplitude cyclic plasticity in 316L*, J. of Testing and Evaluation, Vol. 34, No. 4, 2006.

[17] Mattias Skog*, Uni- and multiaxial ratcheting testing and simulation investigation on the ferritic steel P265*, Master Thesis, KTH/Inspecta Nuclear, 2015.

[18] Gustav Eklund, *Experimental and numerical investigation of ratcheting effects in 316L stainless steel – The two-rod approach*, Master Thesis, KTH/Inspecta Nuclear, 2014.

[19] Jansson, D; Wallin, P, *Progressive Deformation in Nuclear Piping – Experimental Investigation and Theoretical Considerations,* Master Thesis, Division of solid mechanics/AREVA NP Uddcomb, 2013.

[20] Granlund, J., *Structural Steel Plasticity: Experimental Study and Theoretical Modelling*, Tekniska högskolan i Luleå, 1997.

[21] EN-1993-1-4. *Design of steel structures – Part 1-4: Supplementary rules for stainless steel*.

[22] RCC-MRx. *Design and Construction Rules for Mechanical Components of Nuclear Installations.* Afcen, 2012 edition.

APPENDIX 1 - Drawings of tube test specimens

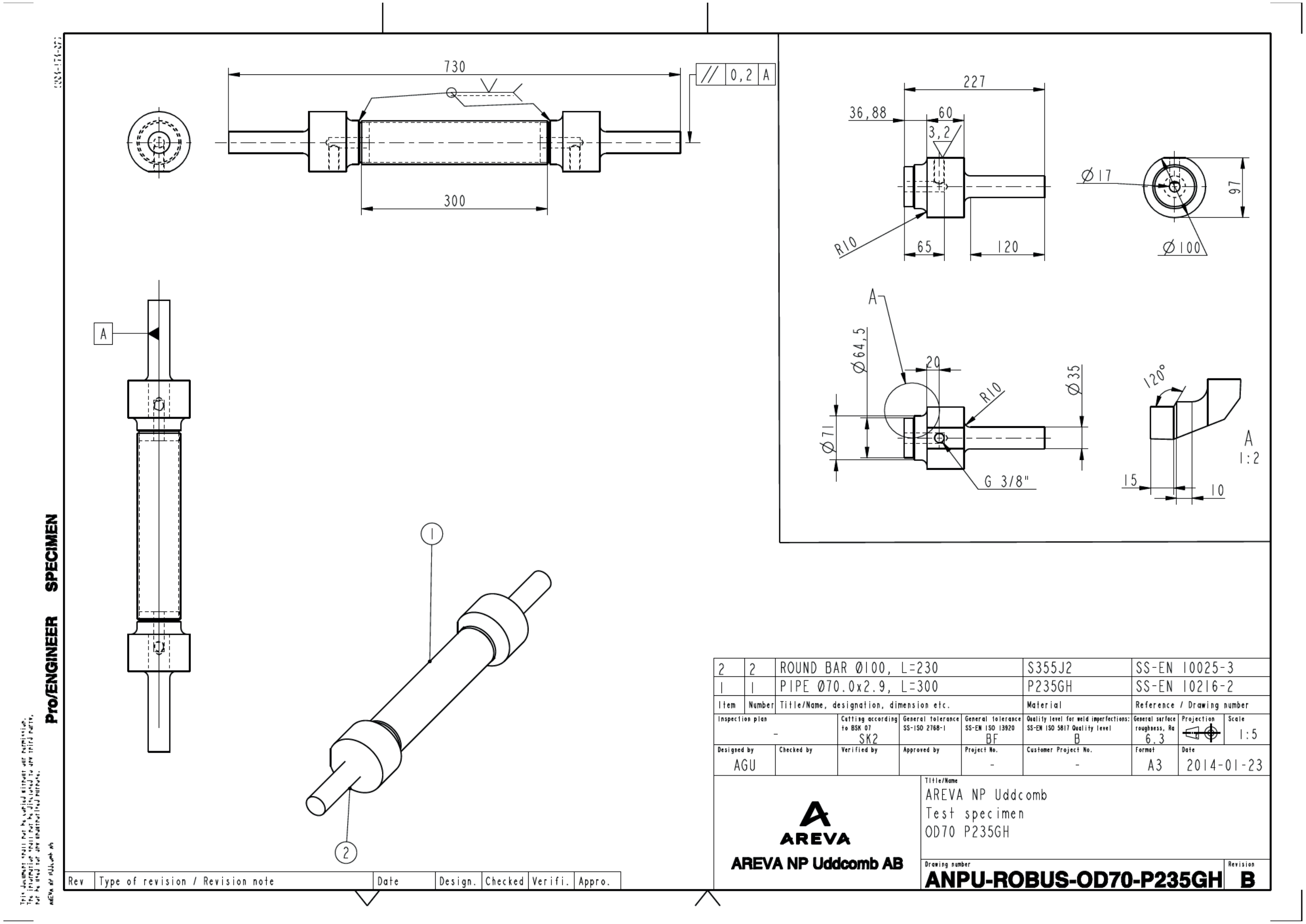

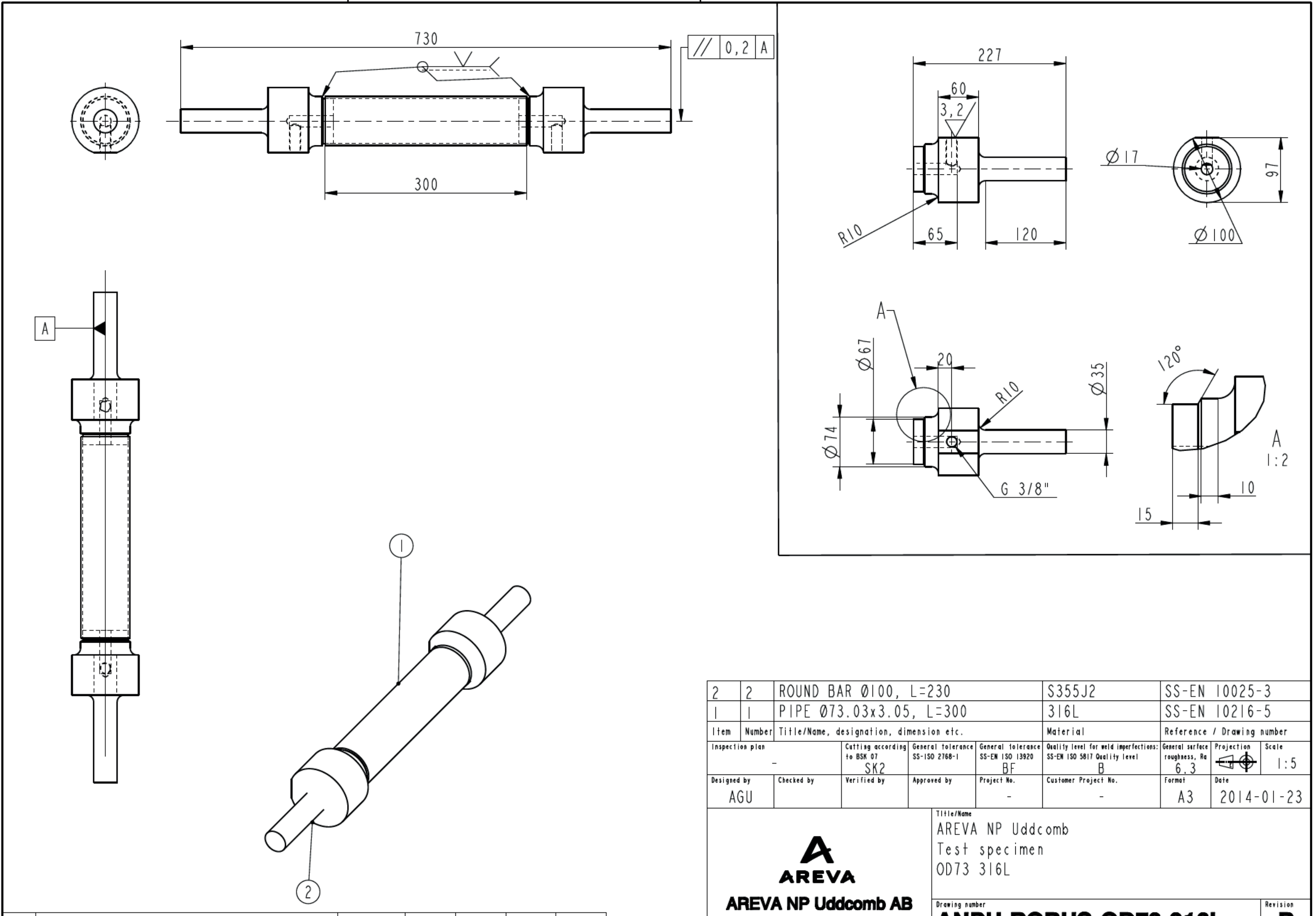

Item	Number	Title/Name, designation, dimension etc.	Material	Reference / Drawing number
2	2	ROUND BAR Ø100, L=230	S355J2	SS-EN 10025-3
1	1	PIPE Ø73.03x3.05, L=300	316L	SS-EN 10216-5

Inspection plan	Cutting according to BSK 07	General tolerance SS-ISO 2768-1	General tolerance SS-EN ISO 13920	Quality level for weld imperfections: SS-EN ISO 5817 Quality level	General surface roughness, Ra	Projection	Scale
-	SK2		BF	B	6.3		1:5

Designed by	Checked by	Verified by	Approved by	Project No.	Customer Project No.	Format	Date
AGU				-	-	A3	2014-01-23

AREVA

AREVA NP Uddcomb AB

Title/Name
AREVA NP Uddcomb
Test specimen
OD73 316L

Drawing number
ANPU-ROBUS-OD73-316L

Revision
B

Rev	Type of revision / Revision note	Date	Design.	Checked	Verifi.	Appro.

Pro/ENGINEER SPECIMEN

This document shall not be copied without our permission.
The information shall not be disclosed to any third party,
nor be used for any unauthorized purposes.
AREVA NP Uddcomb AB

2015:43

The Swedish Radiation Safety Authority has a comprehensive responsibility to ensure that society is safe from the effects of radiation. The Authority works to achieve radiation safety in a number of areas: nuclear power, medical care as well as commercial products and services. The Authority also works to achieve protection from natural radiation and to increase the level of radiation safety internationally.

The Swedish Radiation Safety Authority works proactively and preventively to protect people and the environment from the harmful effects of radiation, now and in the future. The Authority issues regulations and supervises compliance, while also supporting research, providing training and information, and issuing advice. Often, activities involving radiation require licences issued by the Authority. The Swedish Radiation Safety Authority maintains emergency preparedness around the clock with the aim of limiting the aftermath of radiation accidents and the unintentional spreading of radioactive substances. The Authority participates in international co-operation in order to promote radiation safety and finances projects aiming to raise the level of radiation safety in certain Eastern European countries.

The Authority reports to the Ministry of the Environment and has around 300 employees with competencies in the fields of engineering, natural and behavioural sciences, law, economics and communications. We have received quality, environmental and working environment certification.

Strålsäkerhetsmyndigheten
Swedish Radiation Safety Authority

SE-171 16 Stockholm
Solna strandväg 96

Tel: +46 8 799 40 00
Fax: +46 8 799 40 10

E-mail: registrator@ssm.se
Web: stralsakerhetsmyndigheten.se